New Destructive and Non-Destructive Methods to Quantify Fracture Toughness of High-Strength Rail Steels

by

Feng Yu

A thesis submitted in partial fulfillment of the requirements for the degree of

Doctor of Philosophy

Department of Mechanical Engineering

University of Alberta

Abstract

Rail breaks, resulting from increasing heavy axle-load operations and harsh environmental conditions, remain a major cause of catastrophic derailment of vehicles in North America. The objective of this research project is to develop convenient testing methods to identify the optimum high-strength rail steels for Canadian weather, which can contribute to reducing derailment risks for the Canadian railway industry. In this research project, both destructive and non-destructive testing methods are developed to quantify the fracture toughness of high-strength rail steels. The project can be broadly divided into two phases.

Phase I, which is reported in Chapters 2 and 3, involves establishing an extended strain energy density (SED) model for estimating the fracture toughness of high-strength rail steels at 23, -10, and -40^{o}C. First, the mechanical properties, including the mode I critical stress intensity factor (K_{Ic}), constitutive equation, and Vickers hardness, of three types of high-strength rail steels are tested and compared at 23, -10, and -40^{o}C. According to the experimental results, their K_{Ic} values and tensile properties are not correlated with each other. Further study in phase I involves investigating the influence of stress triaxiality (defined as the ratio of hydrostatic stress to von Mises stress) on the plastic deformation and fracture behaviour of rail steels. An extended SED model that considers the effect

of stress triaxiality on both distortional and dilatational SEDs is proposed for assessing the fracture toughness of high-strength rail steels. The critical SED factor, determined by calculating the product of the critical SED and a characteristic distance ahead of the crack tip, is found to well correlate with the K_{Ic} values among the three types of rail steels at 23, -10, and -40^{o}C. The results also confirm that the dilatational energy dissipation (also known as damage energy dissipation) at the crack tip is the primary component to correlate the critical SED factor with the K_{Ic} of rail steels.

In Phase II, which is reported in Chapters 4 and 5, a more convenient non-destructive indentation technique is developed for estimating the fracture toughness of high-strength rail steels. First, a new constitutive model with coupled stress-triaxiality-dependent plasticity and damage is postulated to describe the mechanisms involved in the plastic deformation and ductile damage to rail steels under different levels of stress triaxiality. Based on the new constitutive model, not only is the independence of the constitutive equation from stress triaxiality explained, but a stress-triaxiality-dependent ductile damage model is also developed to estimate the critical damage parameter (D_{cr}) at the crack tip. With this ductile damage model, the indentation fracture toughness (K_{Ind}) of rail steels is estimated based on the D_{cr} at the crack tip. In addition, the study in Phase II uses a parameter κ to accommodate the potential difference of the D_{cr} value in the two loading modes (tensile fracture and indentation compression).

The study shows that D_{cr} is indeed stress-triaxiality dependent and increases with the increase of stress triaxiality. The results also show that the change in K_{Ind} based on D_{cr} either at the crack tip or for the smooth specimen is generally consistent with the difference in the measured fracture toughness (K_{Ic}) among the three rail steels. However, for materials that show small difference in K_{Ic}, i.e., within the scattering of the measured data, K_{Ind} based on the D_{cr} at the crack tip may show a different trend from that based on the D_{cr} for the smooth specimen, which depends on the selected κ values. Such an issue needs further investigation using materials that cover a wide range of fracture toughness.

Compared to the destructive testing method, the non-destructive indentation technique is more convenient, and has the potential to serve as a tool for the in-field health monitoring of rail steels and for the material evaluation, at an early stage, of the new rail steel under development.

Acknowledgement

I would like to express my sincere thanks to my supervisors Drs. P-Y Ben Jar and Michael T. Hendry for their valuable guidance, patience and support throughout the course of my doctoral thesis work. I would like to extend my thanks to Dr. John A. Nychka for his support and advice during my thesis work; to Dr. Zengtao Chen for his support on testing device; to Mr. Faulkner in the Department of Mechanical Engineering at the University of Alberta for the technical assistance during the experimental work, and to Dr. Nigel Peters from CN for his valuable input and support.

I would like to express my appreciation to the Canadian Rail Research Laboratory (CaRRL), the China Scholarship Council (CSC), and the University of Alberta for awarding prestigious scholarships. CaRRL is funded by the Natural Sciences and Engineering Research Council of Canada (NSERC), Canadian Pacific Railway, Canadian National Railway, the Association of American Railways – Transportation Technology Center Inc., Transport Canada and Alberta Innovates – Technology Futures.

I would like to express my deep gratitude to my parents and parents-in-law, Huihua, Anqing, Youzhen and Shijie for their support and encouragement. Finally, I would like to thank my wife Qun and my little daughter Yue for being a source of energy and inspiration.

Table of Contents

Abstract ii
Acknowledgement v
Table of Contents vi
List of Tables ix
List of Figures x
Nomenclature xix
Chapter 1 Introduction 1
1.1 Background and motivation 1
1.2 Transverse rail breaks 4
1.3 Literature review on the characterization of fracture toughness 8
1.3.1 Standard fracture toughness tests 8
1.3.2 Fracture toughness prediction 10
1.3.2.1 Critical fracture stress and fracture strain models 10
1.3.2.2 Notch stress intensity factor (NSIF) model 11
1.3.2.3 Stress energy density (SED) theory 12
1.3.2.4 Indentation technique 14
1.4 Objectives and outline of this study 16
Chapter 2 Effect of temperature on deformation and fracture behaviour of high-strength rail steels 21
2.1 Introduction 21
2.2 Mechanical testing and simulation 22
2.2.1 Mechanical testing 23
2.2.1.1 Uniaxial tensile test 23
2.2.1.2 Three-point bending test 25
2.2.1.3 Vickers hardness test 27
2.2.2 FE modelling 29
2.3 Results 31
2.3.1 True stress-strain relationship in tension 31
2.3.1.1 Mechanical testing results 31
2.3.1.2 Simulation results 34
2.3.2 Mode I critical stress intensity factor (K_{Ic}) 39

2.3.3 Vickers hardness 41
2.3.3.1 Test results 41
2.3.3.2 FE simulation of Vickers indentation 44
2.4 Discussion 46
2.5 Conclusions 48

Chapter 3 Fracture behaviour at the sharp notch tip of high-strength rail steels - Influence of stress triaxiality 50

3.1 Introduction 50
3.2 Theoretical model 53
3.2.1 Critical strain energy density factor 54
3.2.2 Equivalent plastic fracture strain 57
3.3 Experimental investigation 59
3.3.1 Materials and test specimens 59
3.3.2 Smooth specimens 60
3.3.3 Short-gauge specimens 62
3.3.4 Single-edge-notched bend (SENB) specimens 63
3.4 Numerical simulations 65
3.4.1 FE modelling of smooth specimens 66
3.4.2 Application of constitutive equations 70
3.4.2.1 FE modelling of short-gauge specimens 70
3.4.2.2 FE modelling of SENB specimens 73
3.5 Results 80
3.5.1 Equivalent plastic fracture strain of pre-cracked SENB specimen 80
3.5.2 K_{Ic} from SENB tests 82
3.5.3 K_{Ic} prediction 84
3.6 Conclusions 87

Chapter 4 A new constitutive model for high-strength rail steels by considering stress-triaxiality-dependent plasticity and damage 89

4.1 Introduction 89
4.2 New constitutive model 92
4.2.1 Damage-free constitutive equation and its dependence on stress triaxiality 94
4.2.2 Dependence of damage evolution on stress triaxiality 95
4.2.3 The explicit form of the new constitutive model 97

4.3 Characterization of conventional constitutive equation 98
4.3.1 Materials and test specimens 98
4.3.2 Fundamental mechanical properties 99
4.3.3 Conventional constitutive equation 100
4.4 Calibration of new constitutive model 102
4.4.1 Damage parameter 103
4.4.2 Damage-free constitutive equation 106
4.4.3 Material constant 112
4.5 Discussion 116
4.6 Conclusion 119

Chapter 5 Indentation fracture toughness of high-strength rail steels based on a stress-triaxiality-dependent ductile damage model 120

5.1 Introduction 120
5.2 Theoretical background 124
5.2.1 Indentation fracture toughness 124
5.2.2 Determination of critical contact depth 125
5.3 Experimental and numerical methodologies 129
5.3.1 Materials 129
5.3.2 Experimental details 130
5.3.3 Finite element modelling 134
5.4 Results 136
5.4.1 Locus of fracture strain versus stress triaxiality 136
5.4.2 Stress triaxiality effect on critical damage parameter 142
5.4.3 Indentation fracture toughness 148
5.4.3.1 Critical contact depth 149
5.4.3.2 Correlation of K_{Ind} and K_{Ic} 152
5.5 Conclusions 154
5.6 Appendix A 155

Chapter 6 Conclusions and Future Work 158

6.1 Conclusions 158
6.2 Future work 161

References 163

List of Tables

Table 2.1 Mechanical properties of rail head and foot from tensile tests at 23, -10 and -40°C 33
Table 2.2 Parameters in Eq. (2.4) for rail head and foot at all three temperatures 38
Table 2.3 K_{Ic} for rail head, web, and foot at temperature 23, -10, and -40°C..... 39
Table 3.1 Mechanical properties for the three rail steels at 23, -10 and -40°C. .. 61
Table 3.2 Parameters in Eq. (2.4) for three rail steels at temperature 23, -10, and -40°C..... 69
Table 3.3 Fracture strain of pre-cracked SENB specimen..... 82
Table 4.1 Fundamental mechanical properties for the CZ rail steel 100
Table 4.2 Summary of values for parameters in Eq. (4.9) for the CZ rail steel. 106
Table 4.3 Parameters in Eq. (2.4) for conventional and damage-free constitutive equations of smooth specimen 112
Table 5.1 Plastic fracture strain of the pre-cracked SENB specimen for the three rail steels 142
Table 5.2 Parameters of D and λ in Eq. (5.13) for three rail steels 147
Table 5.3 Critical contact depth h_c^* for the given D_{cr}^* values..... 151

List of Figures

Figure 1.1 A case of derailment that happened at Gainford, Alberta in 2013. Source: the Transportation Safety Board of Canada [6] 2
Figure 1.2 Distribution of derailments by incident cause and speed on main track rail, 2001-2014: (a) 0 to 16 km/h; (b) 16 to 40 km/h; (c) 40 to 64 km/h; and, (d) > 64 km/h. Source: Leishman, Eric M [4]. 2
Figure 1.3 Comparison of number of derailments between winter and summer caused by rail breaks in the period from 2001 to 2014. Source: Leishman, Eric M [4]. 3
Figure 1.4 Profile of produced rail steels 6
Figure 1.5 Rail defects resulting from head checks: (a) spalling originating at head checks, and (b) a rail fracture originating from a head check [3]. Copyright 2009. Reproduced with permission from Elsevier. 6
Figure 1.6 Rail defects resulting from squat: (a) top view showing damage to the running surface, and (b) side view showing the early propagation of a squat [3]. Copyright 2009. Reproduced with permission from Elsevier. 7
Figure 1.7 Transverse rail breaks due to internal defects [3]. Copyright 2009. Reproduced with permission from Elsevier. 7
Figure 1.8 Standardized fracture mechanics test specimens: (a) compact tension (CT) specimen, (b) disk-shaped compact tension specimen, (c) single-edge-notched bend (SENB) specimen, (d) middle tension (MT) specimen, and (e) arc-shaped tension specimen. Source: T.L. Anderson [31] 9
Figure 2.1 Sampling location for tensile specimens on the rail cross section (a) and dimensions and geometry of the uniaxial tensile specimens (b) .. 24

Figure 2.2 Uniaxial tensile test set-up (a) and one set of fractured tensile specimens (b) 24
Figure 2.3 Sampling location over the cross section of the rail (a) and dimensions of the SENB specimen (b) 26
Figure 2.4 Set-up of the SENB test..... 26
Figure 2.5 A typical load-displacement (P-δ) curve for the SENB specimens of rail steel, and auxiliary lines, marked 1 and 2, to determine P_Q 27
Figure 2.6 Test set-up, including the cooling chamber, for Vickers hardness test 27
Figure 2.7 The FE model of tensile testing: (a) the mesh pattern and (b) an example of the neck formation 30
Figure 2.8 Engineering stress-strain curves at temperatures 23, -10, and -40^{o}C for the rail head (a) and rail foot (b) 32
Figure 2.9 Curves of average true stress vs. logarithmic strain for rail head (a) and rail foot (b) at 23, -10 and -40°C..... 33
Figure 2.10 Three simulation attempts: (a) three equivalent stress-strain curves including the missing section in Figure 2.9, and (b) comparison of load-elongation curves between the three SAs and the experiment ... 35
Figure 2.11 Rail foot at 23^{o}C: (a) regeneration of the experimental results from the FE simulation, and (b) the corresponding equivalent stress-strain curve and values for the parameters in Eq. (2.4) 36
Figure 2.12 The equivalent true stress-strain curves of (a) the rail head, and (b) the rail foot, at temperatures 23, -10 and -40^{o}C..... 38
Figure 2.13 Vickers hardness distribution on rail head (a) and rail foot (b) at 23^{o}C 42
Figure 2.14 The indentation shape under six loading levels from 100 to 2000 gf 43

Figure 2.15 The relationship between indentation load and depth for (a) the rail head, and (b) the rail foot 43
Figure 2.16 Effect of temperature on the Vickers hardness for both the rail head and foot 44
Figure 2.17 The FE model of Vickers indentation test: (a) the model, and (b) the contour plot of von Mises stress showing the localized deformation. 45
Figure 2.18 The experimental and computational indentation load-depth curves of rail head (a) and rail foot (b) at temperatures 23, -10, and -40^{o}C... 46
Figure 3.1 The overall approach of correlating tensile properties to K_{Ic} based on an extended SED model 53
Figure 3.2 Geometry and dimensions of (a) smooth specimen, (b) short-gauge specimen, and (c) SENB specimen 59
Figure 3.3 Temperature effect on the mean true stress-logarithmic strain curves of smooth specimens for (a) CZ, (b) EV, and (c) JP high-strength rail steels 61
Figure 3.4 Temperature effect on the mean true stress-logarithmic strain curves of short-gauge specimens for (a) CZ, (b) EV, and (c) JP high-strength rail steels 63
Figure 3.5 Temperature effect on stress intensity factor versus CMOD (K_I - δ) curves of SENB specimens: (a) CZ, (b) EV, and (c) JP rail steels 65
Figure 3.6 Deformed shape and FE discretization of the smooth specimen of JP rail steel at 23^{o}C 68
Figure 3.7 Comparison of load-elongation and cross-section reduction between experimental testing and FE modelling of JP rail steel at temperature of (a) 23^{o}C, (b) -10^{o}C, and (c) -40^{o}C 68
Figure 3.8 Distribution of stress triaxiality and equivalent plastic strain along the minimum cross section at the onset of fracture initiation in the smooth specimen for JP rail steel at 23^{o}C 69

Figure 3.9 Evolution of stress triaxiality with the increase of the equivalent plastic strain of smooth specimens, and its average value at temperature 23, -10, and -40°C for (a) CZ, (b) EV, and (c) JP rail steels 70
Figure 3.10 Mesh pattern of the FE model for the short-gauge specimens, overlaid on a fractured JP specimen tested at 23°C 71
Figure 3.11 Comparison of experimental and simulation results of short-gauge specimens for (a) CZ, (b) EV, and (c) JP rail steels 72
Figure 3.12 Distribution of stress triaxiality and equivalent plastic strain on the minimum cross section of short-gauge specimen at the onset of fracture initiation for JP rail steel at 23°C..... 72
Figure 3.13 Stress triaxiality evolution with the increase of the equivalent plastic strain of short-gauge specimens, and its average value at temperature 23, -10, and -40°C for (a) CZ, (b) EV, and (c) JP rail steels..... 73
Figure 3.14 The SENB test of JP rail steel at 23°C: (a) the global mesh pattern and (b) the mesh pattern at the sharp notch tip, within the region enclosed in (a) 75
Figure 3.15 Plots of K_I versus CMOD from the FE modelling, superimposed on the curves in Figure 3.4 from the SENB tests, at temperature 23, -10, and -40°C for (a) CZ, (b) EV, and (c) JP high-strength rail steels..... 75
Figure 3.16 FE simulation results ahead of the sharp notch tip of SENB specimen for JP rail: (a) distributions of stress triaxiality and equivalent plastic strain along the crack path, and (b) comparison of FE models with standard and 1/r singularity, plane-strain elements..... 77
Figure 3.17 Stress triaxiality distribution ahead of the sharp notch tip of SENB specimen at the onset of fracture, for JP rail steel at 23°C 77
Figure 3.18 Determination of the characteristic distances with the maximum stress triaxiality for three rail steels at 23, -10, and -40°C..... 78

Figure 3.19 Stress triaxiality evolution with the increase of the equivalent plastic strain of SENB specimens, and its average value at temperature 23, -10, and -40^{o}C for (a) CZ, (b) EV, and (c) JP rail steel..... 78
Figure 3.20 Dependence of equivalent plastic fracture strain on stress triaxiality of three rail steels at (a) 23, (b) -10, and (c) -40^{o}C 81
Figure 3.21 Experimental data of K_{Ic} values among the three high-strength rail steels at temperature 23, -10, and -40^{o}C 83
Figure 3.22 Welch's t-test analysis: (a) t-distribution with 95% confidential level at degree of freedom 23, and (b) t-test results between the EV and JP rail steels at 23, -10, and -40^{o}C 84
Figure 3.23 Differences in the critical SED values of (a) smooth specimen, (b) short-gauge specimen, and (c) sharp notch tip of SENB specimen, among the three rail steels at temperature 23, -10, and -40^{o}C 86
Figure 3.24 Comparison of the predicted K_{Sc} values with the measured K_{Ic} for the three rail steels at temperature 23, -10, and -40^{o}C 86
Figure 4.1 The overall approach of constructing a new constitutive model for rail steels to explain the independence of the conventional constitutive equation from the stress triaxiality..... 92
Figure 4.2 Geometry and dimensions of (a) smooth and (b) short-gauge specimens 98
Figure 4.3 Typical experimentally-determined stress-strain curves for smooth and short-gauge specimens of the CZ rail steel 100
Figure 4.4 Comparison of load and diameter reduction as functions of elongation between experiment and FE simulation for (a) smooth and (b) short-gauge specimens 102
Figure 4.5 Summary of results from the experimental testing and the FE simulation for loading-unloading tests of smooth specimens: (a) numerical and experimental loading-unloading tensile tests, (b)

correction factor β, (c) effective elastic modulus E, and (d) damage parameter D..... 105
Figure 4.6 Comparison of data from the experimental testing with those from the FE simulation for smooth specimen, using separate material input for damage evolution and damage-free constitutive equation: (a) damage evolution as a function of equivalent plastic displacement, (b) load-elongation curve, and (c) diameter reduction as a function of elongation..... 108
Figure 4.7 Results from FE simulation of loading-unloading of smooth specimen at three points on the minimum cross section: (a) equivalent plastic strain, (b) damage evolution, and (c) equivalent stress-strain curves 108
Figure 4.8 Contour plots for equivalent plastic stain (PEEQ), von Mises stress (Mises in MPa), hydrostatic stress (Pressure in MPa), and damage parameter (SDEG) from the FE modelling: (a) using the conventional constitutive equation and (b) using separate inputs for damage evolution and damage-free constitutive equation 111
Figure 4.9 Comparison of conventional constitutive equation and damage-free constitutive equation for smooth specimens of the CZ rail steel 111
Figure 4.10 FE model of short-gauge specimen: (a) showing five zones in the gauge section with different material property inputs and (b) variation of equivalent plastic strain and stress triaxiality in the radial direction of the cross section and the corresponding average values for each of the five zones at the onset of fracture 115
Figure 4.11 Comparison of load-logarithmic strain curves for short-gauge specimen, from experimental testing and FE simulations (based on Eq. (4.10a) or the conventional constitutive equation) 115
Figure 4.12 Damage evolution in smooth and five zones of short-gauge specimens..... 116

Figure 4.13 Damage-free constitutive equations for smooth and five zones of short-gauge specimens 116
Figure 5.1 The overall approach to determine the critical contact depth based on the critical damage parameter at the crack tip for calculating the indentation fracture toughness 122
Figure 5.2 Dimensions and geometries of four types of axisymmetric tensile specimens: (a) smooth specimen, (b) notch type I (NTI) specimen, (c) short-gauge specimen, and (d) notch type II (NTII) specimen 132
Figure 5.3 Indentation test: (a) schematic presentation of the test set-ups and ball indenter and (b) a typical indentation loading-unloading curve (for JP rail steel) 133
Figure 5.4 Dimensions of the SENB specimen for the standard fracture toughness test 133
Figure 5.5 FE models of (a) smooth, (b) NTI, (c) short-gauge, and (d) NTII specimens 135
Figure 5.6 FE model for the SENB specimen (left) and details of the mesh pattern at the notch tip (right) 136
Figure 5.7 Comparison of experimental and numerical true stress-logarithmic strain curves of four types of tensile specimens for (a) JP, (b) EV, and (c) CZ rail steels 137
Figure 5.8 Contour plots of stress triaxiality at the onset of fracture for (a) smooth, (b) NTI, (c) short-gauge, and (d) NTII specimens of JP rail steel 138
Figure 5.9 Evolution of stress triaxiality and its average value in an element of FE modelling of four types of tensile specimens that has the maximum stress triaxiality at fracture initiation for: (a) JP, (b) EV, and (c) CZ rail steels 138

Figure 5.10 Dependence of equivalent plastic fracture strain on average stress triaxiality for (a) JP, (b) EV, and (c) CZ rail steels..... 140
Figure 5.11 Comparison of linear portion of P-δ curves between experiment and simulation for the JP rail steel..... 141
Figure 5.12 Distribution of stress triaxiality at the onset of fracture for the pre-cracked SENB specimen of the JP rail steel..... 142
Figure 5.13 Evolution of stress triaxiality and the corresponding average stress triaxiality values for the three rail steels, based on stress triaxiality evolution in an element that is located ahead of the crack tip with the maximum stress triaxiality..... 142
Figure 5.14 Experimental and numerical true stress-logarithmic strain curves from the loading-unloading smooth and short-tensile tests for JP rail steel..... 143
Figure 5.15 Depiction of the ductile damage model in Eq. (5.13) for smooth and short-gauge specimens of JP rail steel: (a) experimental unloading slope, S_{exp}, (b) correction factor, β, (c) change of elastic modulus, E, and (d) extrapolation of the measured E values to the stress triaxiality level at the crack tip of SENB specimen..... 144
Figure 5.16 Damage parameter and D_{cr} values for (a) smooth, (b) short-gauge, and (c) at the crack tip of pre-cracked SENB specimens of the three rail steels..... 148
Figure 5.17 Variation of h_{pile} as a function of h_{max} for the three rail steels.... 150
Figure 5.18 Variation of elastic modulus E^* in the ball indentation test for (a) JP, (b) EV, and (c) CZ rail steels..... 150
Figure 5.19 Damage development for the three rail steels under the ball indentation test..... 151

Figure 5.20 Curve fitting between the indentation load (F) and the contact depth (h_c) of three rail steels using quadratic polynomial functions 153
Figure 5.21 The indentation fracture toughness (K_{Ind}) estimated by adjusting the D_{cr} at the crack tip using κ in the range from 0.01 to 0.6, and compared with the K_{Ic} for the three rail steels 153
Figure 5.22 The conventional indentation fracture toughness ($K_{Ind,con}$) estimated by the D_{cr} from the smooth specimen, and compared with the K_{Ic} for the three rail steels 154
Figure 5.A1 Plots of (a) indentation load-unload curves and (b) Brinell hardness values for the standard testing block..... 157
Figure 5.A2 Determination of (a) frame compliance and (b) indentation elastic modulus for the standard hardness testing block 157

Nomenclature

ASTM	American Society for Testing and Materials
CMOD	Crack mouth opening displacement
CTOD	Crack tip opening displacement
CWR	Continuously welded rails
EDM	Electric discharge machining
HAL	Heavy axel loads
SED	Strain energy density
SENB	Single-edge-notched bend
UTS	Ultimate tensile strength
a, b, c, d, e, α, $\bar{\beta}$, γ, M, and *n*	Constants for constitutive equation
a_0	Pre-cracked length
A	Cross-sectional area during deformation
A_0	Original cross-sectional area
A_c	Contact area
A_f	Cross-sectional area measured after fracture
$\bar{B}$	Thickness of SENB specimen
C	Indentation total compliance
C_f	Indentation load frame compliance
C_s	Indentation specimen compliance
D	Damage parameter

D^*	Damage parameter under indentation
$\overline{D}$	Amount of damage parameter in smooth specimen at the onset of fracture
D_0	Initial amount of damage before the test
D_{cr}	Critical damage parameter
D_{cr}^*	Critical damage parameter under indentation compression
E	Elastic modulus of damaged material
E^*	Elastic modulus under indentation
E_0	Young's Modulus of specimen
E_{i}	Young's Modulus of indenter
E_{eff}	Effective modulus (Hertzian contact theory)
F	Indentation load
F_{max}	Maximum indentation load
H	Hardness
h_c	Contact depth
h_c^*	Critical contact depth
h_{pile}	Height of pile-up
h_{max}	Maximum recorded contact depth
K_{I}	Mode I stress intensity factor
K_{Ic}	Mode I critical stress intensity factor
K_{Sc}	Equivalent critical stress intensity factor
K_{min}	Minimum stress intensity factor

$K_{\max}$	Maximum stress intensity factor
l	Diagonal length of Vickers hardness
L	Tension load
L_f	Tension load at onset of fracture
P	Load in SENB test
P_{Q}	Provisional load of SENB test
$P_{\max}$	Maximum load of SENB test
p_{th}	Damage threshold strain in triaxial loading
R	Ball indenter radius
r_0	Characteristic distance ahead of crack tip
$\bar{S}$	Span length of SENB specimen
S	Contact stiffness
S_{D}	Total section area of flaws
S_0	Effective section area without flaws
S_{exp}	Unloading slope from experiment
S_{FEM}	Unloading slope from simulation
s	SED factor
s_c	Critical SED factor
W	Width of SENB specimen
w	Total strain energy density
w_e	Elastic strain energy density
w_p	Plastic strain energy density

w_c	Critical strain energy density
w_f	Specific fracture energy at the crack tip
w_{Ind}	Specific indentation energy to fracture
X	Distance ahead of the crack tip
δ	CMOD
κ	Adjusting parameter of indentation damage
λ	Exponent of ductile damage model
ν	Poisson's ratio
ν_i	Poisson's ratio of indenter
φ	Area contraction
ψ	Rice-Tracey-Huang material constant
Υ	Drucker-Prager material constant
ξ	Lode angle parameter
η	Stress triaxiality
η_0	Average stress triaxiality-smooth specimen
η_{av}	Average stress triaxiality-general
$\overline{\eta_{av}}$	Mean value of average stress triaxiality
σ	True stress
σ^*	Damage-free stress in general case
σ_f	Fracture stress
σ_{uts}	Ultimate tensile stress
σ_y	Yield stress

σ_{eq}	Equivalent stress
σ_{ij}	Cauchy stress tensor
σ_m^e	Elastic hydrostatic stress
σ_m^p	Plastic hydrostatic stress
σ_{eq}^e	Equivalent deviatoric elastic stress
σ_{eq}^p	Equivalent deviatoric plastic stress
σ_{eq}^0	Damage-free stress response of smooth specimen
$\boldsymbol{\varepsilon}$	Logarithmic strain
ε_l	Linear elastic strain
ε_y	Yield strain
ε_n	Strain for the onset of necking
ε_p	Logarithmic plastic strain
ε_{eq}	Equivalent strain
ε_e^f	Recovered elastic strain at fracture
ε_p^f	Plastic fracture strain of smooth specimen
ε_t^f	Total fracture strain of smooth specimen
ε_{th}	Damage threshold strain in uniaxial loading
ε_{ij}	Strain tensor
ε_{ii}^p	Plastic volume strain
ε_{eq}^p	Equivalent plastic strain
$\varepsilon_{eq,f}^p$	Equivalent plastic fracture strain

$\varepsilon_{eq,max}^{p}$	Maximum equivalent plastic strain
$\overline{\varepsilon_{eq}^{p}}$	Mean value of equivalent plastic strain
S_{ij}^{e}	Elastic deviatoric stress
S_{ij}^{p}	Plastic deviatoric stress
ϵ_{ij}^{p}	Plastic deviatoric strain
$\beta(\varepsilon_p)$	Correction factor for unloading slope

Chapter 1 Introduction

1.1 Background and motivation

The continuously increasing service demands on rails, such as heavy axel loads and high speed operations, are approaching the limits of rails' ability to act as an effective part of the track structure [1]. Also, at low temperatures, the increase of axial tensile stress and reduction of fracture toughness that occur in continuously welded rails (CWR) [2], make such an issue even worse. As a consequence of these, the frequency of rail breakage elevates [3], which is the most common cause of derailments [4, 5]. Figure 1.1 shows a case of catastrophic derailments which happened at Gainford in Alberta in 2013. The derailment was caused by broken rails, as reported by the Transportation Safety Board of Canada [6]. A recent study has suggested that the broken rails are almost the most significant cause of derailments in all types of railroad track classes in Canada from 2001 to 2014 [4], as shown in Figure 1.2. Thus, installing rail tracks using steels with both high material strength and fracture toughness is of considerable importance. Because the higher is the material strength of rail steels, the greater their wear resistance. Similarly, the tougher are the rail steels, the longer the critical crack size required for rail breakage—and thus, the greater the possibility for the cracks to be detected before the rail breaks. Clearly, this can reduce the risks of derailments.

During the past four decades, the quality of rail steels has been improved tremendously by refining their microstructures through heat-treatment [7-10] and controlling the chemical compositions [11-13]. In the context of such improvement, high-carbon, carbide-free bainitic steels have been found to possess higher wear and crack resistance than the conventional pearlitic steels [14, 15]. At present, however, rail tracks are commonly made out of pearlitic steels, as they

are the cheapest to produce and maintain excellent wear resistance. As well, the appropriate heat treatment has improved both the material strength and fracture toughness of pearlitic rail steels [8].

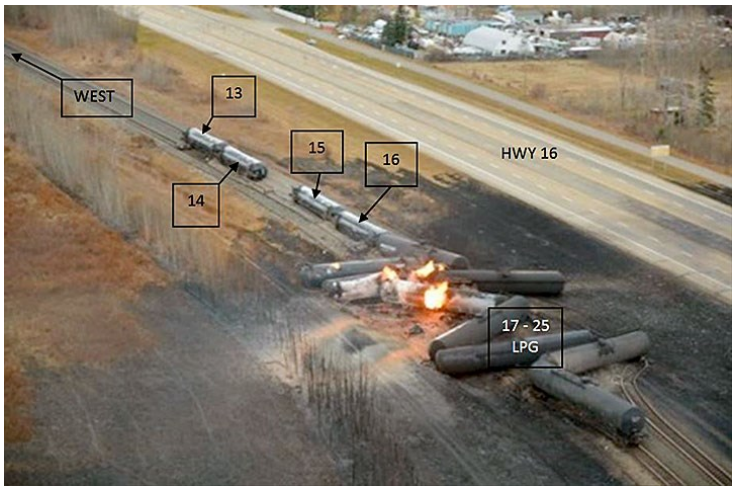

Figure 1.1 A case of derailment that happened at Gainford, Alberta in 2013. Source: the Transportation Safety Board of Canada [6]

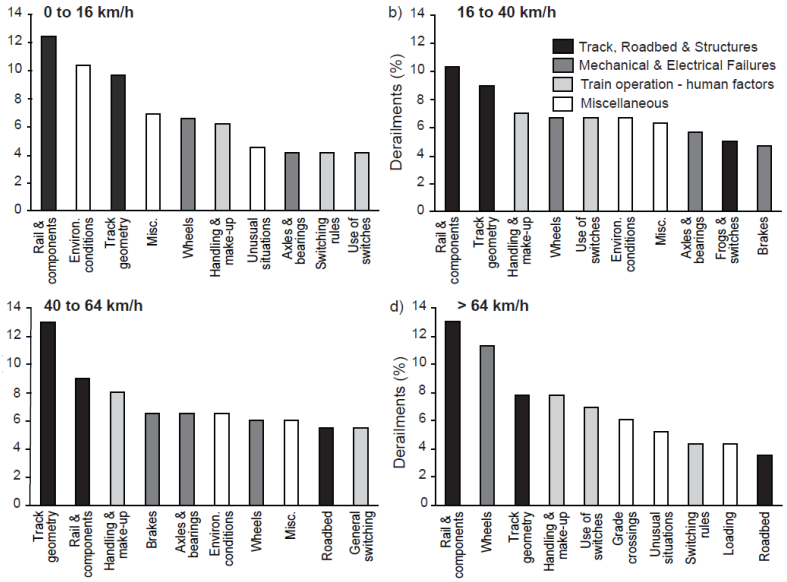

Figure 1.2 Distribution of derailments by incident cause and speed on main track rail, 2001-2014: (a) 0 to 16 km/h; (b) 16 to 40 km/h; (c) 40 to 64 km/h; and, (d) > 64 km/h. Source: Leishman, Eric M [4].

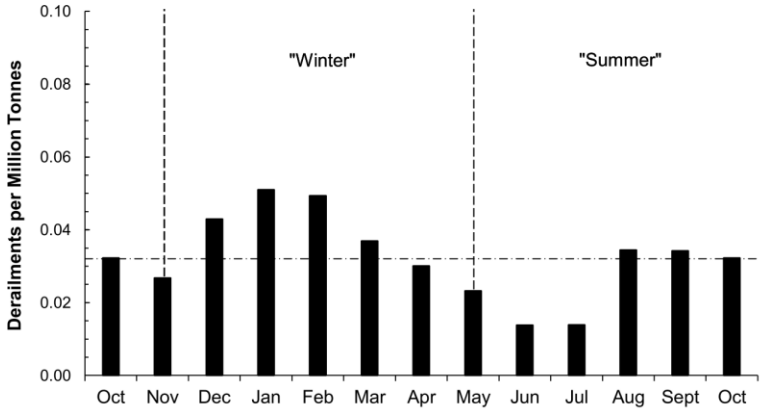

Figure 1.3 Comparison of number of derailments between winter and summer caused by rail breaks in the period from 2001 to 2014. Source: Leishman, Eric M [4].

As shown in Figure 1.3, because of the cold climate in Canada, Canadian train derailments due to rail failure are more prevalent during the winter period, when temperatures commonly fall to the range of -20 to -40^{o}C [16]. Due to this, Canadian railways have raised concerns that the premium high-strength rail steels produced for the North American market may not be optimum for resisting rail breaks in Canada. In view of the various types of high-quality pearlitic rail steels produced worldwide, the Canadian railway industry is looking for several specific types of high-strength pearlitic rail steels that possess good wear resistance and more importantly, have stronger crack resistance than the currently installed ones.

In order to fulfil the Canadian railway industry's requirement, the mechanical properties of different types of rail steels, such as their material hardness, strength, and fracture toughness, must be evaluated in detail. Although standard testing procedures following the American Society for Testing and Materials (ASTM) standards have been established for characterizing these material properties, these methods generally require specific specimen geometries and dimensions [17-19]. For example, in order to obtain material strength without considering the boundary effect, tests should employ a tensile specimen that satisfies a certain ratio of the cross-sectional dimension to the length of the

reduced gauge section. Especially for the fracture toughness testing, manufacture of either the single-edge-notched bend (SENB) specimens for the three-point bending test or the compact-tension (CT) specimens under tensile loading requires a series of facilities, such as electric-discharge machining (EDM) and abrasive waterjet to machine the special notch tip. In addition, the fatigue pre-cracking requires special high-frequency loading-unloading equipment that is not available in all research institutes. They thus make fracture toughness evaluation using the standard testing method not an easy task. Also, in view of the various types of rail steels, carrying out standardized tests for each of the potential candidates would be costly and time-consuming.

In this study, alternative testing methods of both a destructive and a non-destructive nature are proposed to predict the fracture toughness of rail steels. Both of the proposed methods are more convenient than the standard testing method. The non-destructive testing method in particular can be used for the in-field health monitoring of railway systems and for material evaluation at an early stage of the development of new rail steels.

1.2 Transverse rail breaks

Rails, as one of the most important components of the track structure, are made of high-carbon steel. Their profile, as shown in Figure 1.4, can be divided into three regions: rail head, web and foot. Rails are longitudinal steel members designed to support the heavy axle loads of rapidly moving trains by distributing concentrated wheel loads over the sleepers or supports. Although rails are expected to be serviceable long enough to provide return on investment costs, rail failure is becoming more frequent due to heavy axle loads, increasing traffic density, high train speeds, and axial tensile stress at low temperatures due to CWR. A brief description of the transverse, fissure-type rail breaks—the most

important crack type, and the fracture scenario most likely to cause catastrophic derailment [3, 20]—is provided in the next paragraph.

Transverse-fissure-type rail breaks are caused by either surface-induced cracks or internal defects in the rail head, both of which are generated by wheel-rail rolling contact fatigue (RCF) [3]. Typical surface-induced cracks include so-called “head checks” and “squats”. The first of these occurs preferentially at the corner of the gauge side of a rail, as shown in Figure 1.5(a). After the head checks have grown by several millimeters, the transverse fracture occurs once the crack size is extended to a critical length, as shown in Figure 1.5(b). Squats occur on the top of running surface and grow at a sharp angle with respect to the running surface until they turn in the transverse direction, as shown in Figure 1.6. Figure 1.7 shows the resulting transverse rail break, which is caused by the growth of some pre-existing internal flaws in the rail head, e.g., hydrogen shatter cracks, until a critical crack size is reached.

With the advantage of improved heat-treatment technology, pearlitic rail steels now have high stiffness, and excellent wear- and crack-resistance [21, 22]. The aim of the Canadian railway industry is to select several types of such pearlitic rail steels with optimum wear- and crack-resistance for operation in harsh environmental conditions. Since the wear resistance of pearlitic rail steels has been found to be closely correlated to their hardness [23-25], an indentation-based testing method is likely to be feasible in assessing the fracture toughness of rail steels.

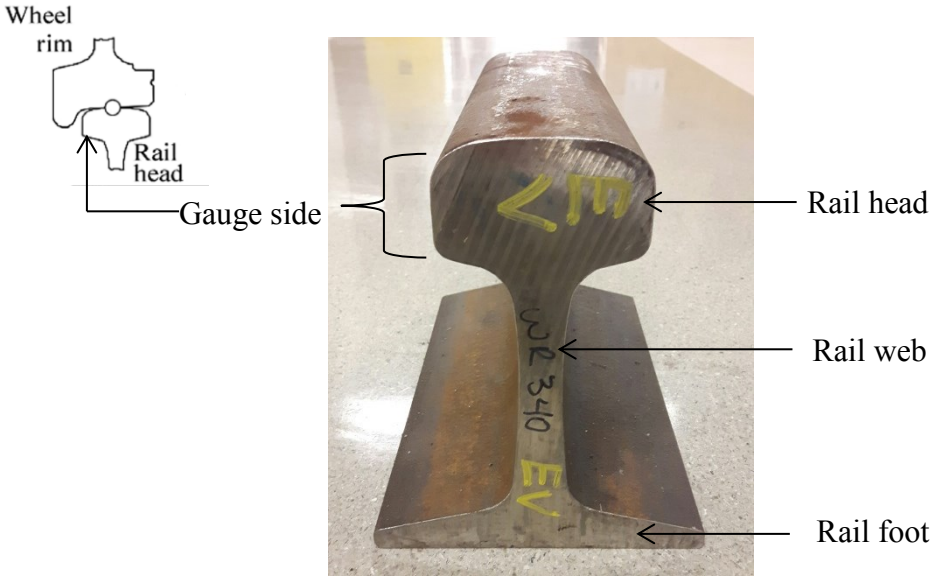

Figure 1.4 Profile of produced rail steels

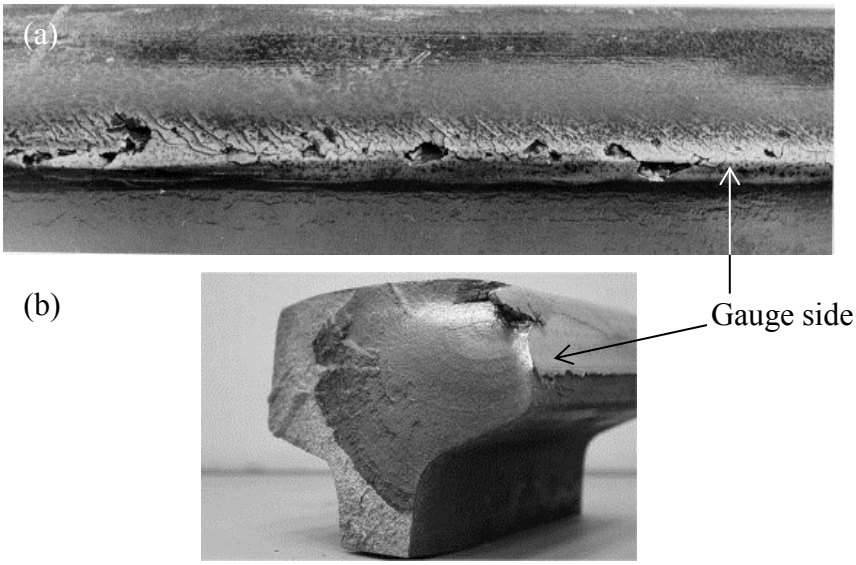

Figure 1.5 Rail defects resulting from head checks: (a) spalling originating at head checks, and (b) a rail fracture originating from a head check [3]. Copyright 2009. Reproduced with permission from Elsevier.

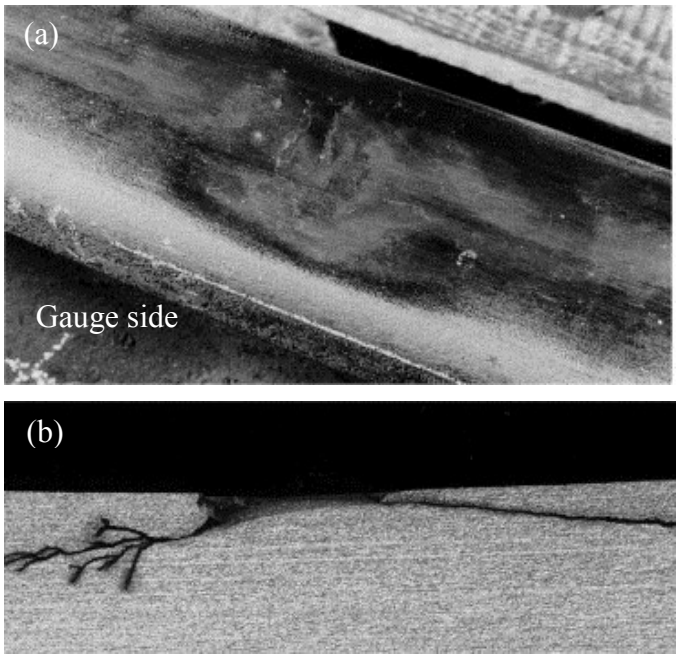

Figure 1.6 Rail defects resulting from squat: (a) top view showing damage to the running surface, and (b) side view showing the early propagation of a squat [3]. Copyright 2009. Reproduced with permission from Elsevier.

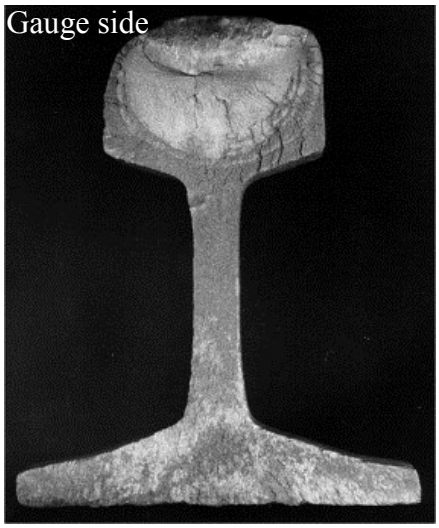

Figure 1.7 Transverse rail breaks due to internal defects [3]. Copyright 2009. Reproduced with permission from Elsevier.

1.3 Literature review on the characterization of fracture toughness

Mode I critical stress intensity factor, K_{Ic}, is a material property used to characterize the fracture toughness of rail steels. As stated in the previous two sections, the fracture toughness value for rail steel plays an important role in assessing railway integrity. Although a standard testing method for measuring the K_{Ic} of rail steels is available in the ASTM E399 [18], this method is not easy to use because of the complex process required for specimen preparation. In this section, in addition to the standard fracture toughness testing method, four existing methodologies for fracture toughness characterization are discussed in order to assess their applicability to rail steels.

1.3.1 Standard fracture toughness tests

In the ASTM E399 [18], the standardized testing procedures for K_{Ic} measurement consist of preparing specimen configurations, fatigue pre-cracking, conducting mechanical testing, and measuring the pre-cracked length from post-test specimens. The five types of standard specimen configurations are compact-tension (CT), single-edge-notched bend (SENB), arc-shaped, disk-shaped, and middle-tension (MT) specimens, shown in Figure 1.8. Among these five types of specimens, CT and SENB are the configurations most commonly used for fracture toughness tests. Fatigue pre-cracking is performed to generate a sharp crack for the proper application of fracture mechanics theory [26-30]. In order for fracture toughness to reflect the true properties of the material, the growth of the fatigue cracks during the pre-cracking process must be sufficiently slow to prevent development of a large plastic zone size. During mechanical testing, the applied load and the crack mouth opening displacement (CMOD) must be measured simultaneously. Although the mechanical testing is relatively straightforward, attention should be paid to the alignment of test set-ups. Data analysis is another

challenging process. Not only should the pre-cracked length be measured in the post-test specimens, but also, due to the strict size requirement in ASTM E399, the validity of the K_{Ic} values must be checked.

Due to the complexity of the testing procedure, completing such tests on one type of rail steels, based on our experience, takes approximately 6 months. Therefore, using the ASTM standard to examine the various types of rail steels is toilsome. In the following section, the existing methods for fracture toughness prediction are reviewed in order to establish new testing methods allowing for the quick estimation of the fracture toughness of rail steels.

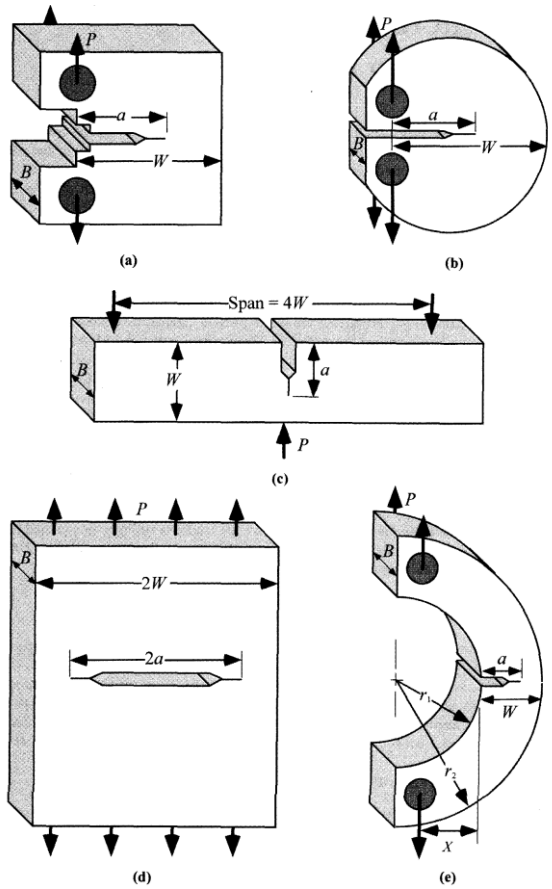

Figure 1.8 Standardized fracture mechanics test specimens: (a) compact tension (CT) specimen, (b) disk-shaped compact tension specimen, (c) single-edge-notched bend (SENB) specimen, (d) middle tension (MT) specimen, and (e) arc-shaped tension specimen. Source: T.L. Anderson [31]

1.3.2 Fracture toughness prediction

This section reviews four typical models for predicting fracture toughness. These approaches are (i) the critical fracture stress and fracture strain models, (ii) the notch stress intensity factor (NSIF) model, (iii) the strain energy density (SED) theory, and (iv) the non-destructive indentation technique.

1.3.2.1 Critical fracture stress and fracture strain models

Ritchie et al. [32] proposed the critical fracture stress criterion, known as the RKR model, to estimate the fracture toughness of high-nitrogen mild steels. The RKR model was postulated based on the development of fracture mechanics [26, 27, 29], through which the stress distribution at the crack tip was successfully derived for both linear-elastic [30, 33-35] and elastic-plastic materials [36-38]. By inferring the critical fracture stress based on the studies of stress distribution at the crack tip [36, 38], Ritchie et al. [32] successfully predicted the K_{IC} value of high-nitrogen mild steel at cryogenic temperatures by postulating that cleavage fracture occurred when the tensile stress at a characteristic distance ahead of the crack tip exceeded the critical fracture stress. In the RKR model, the characteristic distance was assumed to be equivalent to the order of two grain diameters. However, subsequent investigations [39, 40] revealed that no consistent relationship existed between the characteristic distance and the grain sizes. Recently, Neimitz et al. [41] reported a modified formula of the RKR model, demonstrating that the characteristic distance ahead of the crack tip should be defined as the order of the critical CTOD, or the distance of the maximum opening stress located in front of the crack tip for elastic–plastic material. Shlyannikov et al. [42] validated this definition in their study.

The critical fracture strain criterion was originally proposed by McClintock [43] and adapted by Mackenzie et al. [44] and Pandey and Banerjee [45] for

estimating the fracture toughness of ductile materials under stable crack growth where significant plastic deformation was dominant at the crack tip. Ritchie et al. [46] further developed this approach by postulating that fracture initiation occurred when the fracture strain at a characteristic distance ahead of the crack tip exceeded a critical value. The characteristic distance was still assumed to be at several grain diameters ahead of the crack tip.

In view of the above studies, although the concepts of critical fracture stress and fracture strain provide relatively simple means of estimating fracture toughness for ductile materials, determination of the characteristic distance has been reported to depend on the stress states and microstructures at the crack tip [39, 47, 48]. Because of this, the convenience of the above two models disappears. In order to apply the critical fracture stress or fracture strain model to rail steels, effects of the microstructure and the stress states on the characteristic distance, fracture stress, and fracture strain at the crack tip, must be investigated, which makes the critical fracture stress and strain models too complex for engineering applications.

1.3.2.2 Notch stress intensity factor (NSIF) model

Discussion of the NSIF model is limited to the special case of the NSIF for the sharp V-notched tip because the stress intensity factor (SIF) at the crack tip can be extrapolated from several NSIF values determined based on this particular NSIF model. The formulation of the NSIF model is extended from Williams' basic contribution for describing the stress field at the crack tip [30]. Therefore, the NSIF of the sharp V-notch tip has an expression similar to that of the SIF, but less marked singularities of stress and displacement distributions due to the finite notch angles of the sharp V-notches [49-52].

The NSIF model has been commonly used to assess the fracture strength of both brittle [53-56] and ductile materials [57, 58] for specimens with various notch geometries. This NSIF model can also be applied to estimate the fracture

toughness of materials based on an extrapolation of NSIF values determined from different sharp V-notched specimens [54]. However, in order to predict the fracture toughness at the crack tip, several sharp V-notched specimens with different notch angles are required. Moreover, stress distribution around the notch tip must be accurately determined in order to use this approach. Due to the complexity of these procedures, the NISF model is rarely recommended for K_{Ic} prediction. Instead, engineers use this model mainly to evaluate the fracture strength of structures with various types of notches [59].

1.3.2.3 Stress energy density (SED) theory

Sih and his co-workers [60-65] first proposed a special SED theory to study the mechanics and physics of crack propagation at the crack tip of brittle materials. In Sih's SED theory, the strain energy density factor (s) was defined as the product of the SED and a characteristic distance from the point of the crack tip. Crack initiation was controlled by the critical value of the SED factor (s_c), whereas the direction of the crack propagation was determined by imposing a minimum condition on s [60]. Thus, Sih's SED theory is more advanced than Griffith's energy balance theory [26], because the former takes into account both crack initiation and the direction of crack propagation.

Sih's SED theory was originally proposed only as a fracture criterion for brittle materials under mixed-mode loading. Later, this theory has also been adapted to predict the fracture toughness of ductile materials. Shlyannikov [66] extended Sih's SED theory by including the plastic portion of the SED based on the J-integral and accurately calculated the fracture toughness (K_{Ic}) values for both high-nitrogen mild steel and 30Cr steel. Taking a similar approach, Gillemot and his co-workers [67, 68] developed the concept of the absorbed specific fracture energy (ASFE). By extrapolating the SED and the elongation of the plastic zone from the plain and notched specimens to those the crack tip, the

product of the above two parameters was used to estimate the fracture toughness of low- and medium-strength structural materials.

Later, Lazzarin and his co-workers [59, 69-71] proposed a modified volume-based SED approach to assess the fatigue and static fracture of brittle and quasi-brittle engineering materials using notched specimen geometries. Unlike Sih's SED theory, which defines the point-wise critical SED factor as a fracture initiation criterion, the volume-based SED approach uses a line-wise criterion. That is, the determined SED is averaged over a controlled volume (which becomes an area in plane stress or plane strain condition), and failure occurs once the averaged SED value is equal to a critical value. The volume-based SED has been extended for the fracture assessment of ductile materials that are weakened by the presence of notches [72, 73]. The advantage of the volume-based SED approach over Sih's SED theory is that the former needs only a coarse mesh to determine the mean value of SED, while the latter requires a very refined mesh to calculate the SED value. This is because according to Sih's theory, the SED is calculated based on the product of local stresses and strains. Therefore, mesh density at a sharp notch tip should be dense enough to capture the stress singularity [62]. While for the volume-based SED method, the SED at the crack tip is directly determined from the nodal displacement without any calculation involving stresses and strains [74]; thus, only a coarse mesh is required. For instance, for a sharp V-notched tip, in order to obtain the accurate stress singularity more than 3,000 finite elements are required using Sih's SED theory; however, in the same region, the same accuracy can be obtained by only 64 elements using the volume-based SED method [59].

The above SED approach has been used mainly as a powerful fracture criterion for both linear-elastic and elastic-plastic materials that include notches or cracks. The SED approach can also be adapted as a simple method for predicting the fracture toughness of both brittle and ductile materials, similar to those proposed by Gillemot et al. [67], Shlyannikov [66], and Chaouadi et al. [75].

Therefore, the SED approach can be considered a promising candidate for estimating the fracture toughness of rail steels.

1.3.2.4 Indentation technique

In view of its non-destructiveness and convenience, the indentation technique is an ideal alternative to the standard testing method. In fact, the indentation test has been proposed as a promising technique to predict fracture toughness for both brittle and ductile materials [76-86]. In brittle material, such as ceramics, cracks are generated around the indent. Thus, fracture toughness can be characterized based on the crack dimensions and indentation load generated by an indenter [77-79]. In the case of ductile material, though cracks are unlikely to be generated during indentation, researchers have proposed the use of the indentation test to quantify fracture toughness; this involves indenting the material to a critical contact depth at which the specific indentation energy corresponds to the specific work of fracture for crack initiation at the crack tip [80, 82, 87]. This concept is based on the assumption that both the crack tip and indenter tip generate a highly concentrated stress field at similar levels of stress triaxiality. The existing approaches to determine the critical contact depth can be categorized based on the following three criteria: (i) the critical fracture stress [81, 87], (ii) the critical fracture strain [88, 89], and (iii) the critical damage parameter [82-86].

Byun et al. [87] adapted the critical fracture stress criterion [32] to predict the fracture toughness of reactor pressure vessel steels in the ductile-to-brittle transition temperature (DBTT) regime by using the ball indentation technique. This critical fracture stress criterion is difficult to apply because the characterization of the fracture stress at about two grain diameters ahead of the crack tip is obscure [47]. For example, the fracture stresses for either the nucleation of the fracture in the grain boundary or the fracture propagation across the adjacent grains are unlikely to be equal. Thus, the choice regarding which of these to apply as the critical value to determine the critical contact depth is

unclear. Moreover, previous investigations [39, 40] could not find a consistent relationship between characteristic distance and grain size. Therefore, determining the critical contact depth for rail steels based on the critical fracture stress criterion is difficult.

The critical fracture strain criterion was modified from the above critical fracture stress criterion [46] and adapted by Haggag et al. [88], who developed an automatic ball indentation (ABI) technique to estimate the fracture toughness for reactor pressure vessel and pipe steels. For the sake of convenience, instead of determining the exact value of the fracture strain at the crack tip for crack initiation, their approach identified the critical fracture strain with the strain-hardening exponent. Recently, Jeon et al. [89] improved the ABI technique by applying the fracture strain at the crack tip to determine the critical contact depth. However, the critical fracture strain criterion [45, 46] is applicable only to very tough materials in which significant plastic deformation occurs at the crack tip before crack initiation. Therefore, this special ABI technique can be applied only to estimate the indentation fracture toughness of very ductile materials. Since cleavage-like fractures, rather than ductile fractures, are observed at the crack tip of high-strength rail steels, the ABI technique is not appropriate for the current study.

Recently, Lee et al. [82] developed a new indentation model for predicting the fracture toughness of ductile materials based on the principles of continuum damage mechanics (CDM) [90]. The key concept involved in their study was obtaining the critical damage parameter for crack initiation and then using the indentation test to approach that critical damage parameter value until the specific indentation energy could be closely correlated to the specific work of fracture at the crack tip. This indentation model has been applied to predict fracture toughness of materials exhibiting both ductile and cleavage-like fracture behaviour [83-85]. However, previous researchers all assumed that the critical damage parameter is a material constant, independent of stress triaxiality [82-85].

Researchers have long argued about whether the critical damage parameter is indeed independent of stress triaxiality. On the one hand, some researchers, such as Tai [91] and Bonora et al. [92], have claimed that under different loading conditions, the critical damage parameter could be considered a material constant. On the other hand, experimental evidence has shown that with the increase of stress triaxiality, obvious ductile-to-brittle fracture transition was observed [93], indicating a change in the critical damage parameter under different loading conditions. More recently, based on the micro-mechanical studies of the stress triaxiality effect on damage evolution, researchers have found that the critical damage parameter for a representative volume element (RVE) increased with an increase in stress triaxiality [94-96].

As the above literature review demonstrates, both the SED theory and the CDM-based indentation technique are appropriate for estimating the fracture toughness of high-strength rail steels. Due to its convenience and non-destructive features, the indentation testing technique is deemed to be an ideal candidate to estimate the fracture toughness of rail steels. However, the stress triaxiality effect on the critical damage parameter should be further investigated for the application of this non-destructive indentation testing method to rail steels.

1.4 Objectives and outline of this study

The overall objectives of this research project are to investigate influence of temperature (23, -10, and -40^{o}C) on mechanical properties of high-strength rail steels, including the mode I stress intensity factor (K_{Ic}), constitutive equation, and Vickers hardness; and develop new testing methods for predicting fracture toughness of high-strength rail steels.

In this research project, three types of high-strength rail steels, JAPAN NSC FHH (JP), EVRAZ RMSM FHH (EV), and CZECH TZ IH (CZ), are selected as sample materials, which are provided by the Canadian National Railway

Company (CN). These three high-strength rail steels are all high-quality steels that will be installed in the mainline tracks in Canada. Therefore, it is necessary to characterize their material properties before the application.

The specific objectives of this thesis are to:

1. Test and compare mechanical properties of the above three types of high-strength rail steels at 23, -10, and -40^{o}C, including K_{Ic}, constitutive equation, and Vickers hardness, to establish a material database following the ASTM standards.
2. Develop a convenient testing method to quantify fracture toughness for the three high-strength rail steels by studying stress triaxiality effect on plastic deformation and fracture behaviour.
3. Establish a new constitutive model for high-strength rail steels by considering stress triaxiality-dependent plasticity and damage.
4. Develop a new non-destructive testing method for estimating fracture toughness of high-strength rail steels based on a stress triaxiality-dependent ductile damage model.

The remainder of this thesis is divided into five chapters corresponding with the steps in this project.

Chapter 2 explains the detailed experimental procedures on mechanical testing to determine material properties of the three high-strength rail steels, CZ, EV, and JP, at rail head, web, and foot at 23, -10, and -40^{o}C; here the CZ rail steel is used as an example to illustrate the procedures. Three types of mechanical tests, i.e., the standard monotonic tensile, Vickers hardness, and three-point bending tests, are carried out according to the ASTM standards E8/E8M, E384, and E399, respectively [17-19]. The effect of temperature on mechanical properties, including the constitutive equation, Vickers hardness, and mode I critical stress intensity factor (K_{Ic}), is investigated. In order to provide a full inspection of mechanical properties over a cross-section of rail track, the difference in the mechanical properties between the rail head and foot is also studied.

The study presented in Chapter 3 has two purposes. The first is to compare the mechanical properties of the three types of high-strength rail steels, including their tensile strength, ductility, and mode I critical stress intensity factor (K_{Ic}), at 23, -10, and -40^{o}C. Unexpectedly, neither the tensile strengths of the three types of rail steels nor their ductility corresponds to their K_{Ic} measures. That is, although the JP rail steel has the greatest material strength and ductility, its fracture toughness is less than that of the EV rail steel. In light of this result, the second part of Chapter 3 sets out to investigate the fracture behaviour at the crack tip of the three rail steels, and to examine the feasibility of applying the concept of strain energy density (SED) to correlate with K_{Ic} among the three types of rail steels at all three temperatures. To this end, mechanical properties are characterized for not only the smooth specimens but also specially designed short-gauge specimens. In addition, locus of the plastic fracture strain versus the stress triaxiality is established based on results from the smooth and short-gauge specimens using a theoretical model. The equivalent plastic fracture strain of the pre-cracked SENB specimen is then determined by extrapolating the fracture locus to the stress triaxiality level at the crack tip. Based on all of the above information and a determined characteristic distance ahead of the crack tip, the extended SED approach that considers the stress triaxiality effect on both distortional and dilatational SEDs under small-scale yielding, is proposed to predict K_{Ic} of the three rail steels at 23, -10, and -40^{o}C. Because of its simplicity, the extended SED approach can be considered as a destructive testing method for estimating the fracture toughness of rail steels.

In Chapter 4, a new constitutive model of stress triaxiality-dependent plasticity and damage is proposed for rail steels. This model characterizes the mechanisms of plastic deformation and ductile damage of high-strength rail steels and explains the independence of the constitutive equation from the stress triaxiality. In this study, smooth and short-gauge specimens are used to vary the stress triaxiality under tensile loading. Both monotonic and cyclic loading modes are used, with the assistance of numerical simulation, to determine the

constitutive equation and damage evolution, respectively. What motivates this study is the finding that even though stress triaxiality does not affect the conventionally-determined constitutive equation, it has a significant effect on damage evolution. In view of the well-accepted knowledge that the conventionally calibrated constitutive equation contains a coupled phenomenon of strain hardening and damage evolution, the new constitutive model, which takes into account the stress triaxiality effect on both plasticity and damage, is established. After calibrating the new constitutive model, the stress triaxiality effect on both the damage-free stress response to deformation and damage evolution is determined.

Chapter 5 describes the development of an improved non-destructive indentation technique for assessing the fracture toughness of high-strength rail steels. In this study, in view of the possible effect of stress triaxiality on the damage development, indentation fracture toughness (K_{Ind}) is calculated based on the D_{cr} at the crack tip. In addition, the study uses a parameter κ to accommodate the potential difference in D_{cr} values between the two loading modes (tensile fracture and indentation compression). The above approach is applied to three types of high-strength rail steels to determine their K_{Ind}. Two types of notch-free specimens (smooth and short-gauge) are used to calibrate a ductile damage model for predicting damage evolution in the three rail steels, and two additional types of round-notch specimens to establish loci of plastic fracture strain versus stress triaxiality for the three rail steels. After the calibration, damage evolution and D_{cr} value are predicted at the crack tip based on an extrapolation of the calibrated ductile damage model and fracture loci to the stress triaxiality level at the crack tip. These results are then applied to the indentation test, with κ as the adjusting parameter, to determine the critical contact depth for calculating K_{Ind}. On the other hand, K_{Ind} is also determined based on the D_{cr} from the smooth specimen, denoted as the conventional indentation fracture toughness ($K_{Ind,con}$). Validity of both K_{Ind} and $K_{Ind,con}$ are compared with the experimentally measured K_{Ic} values for the three rail steels.

Chapter 6 summarizes the main contributions of this work and recommends future work that has the potential to improve both destructive and non-destructive testing methods for fracture toughness characterization.

Chapter 2 Effect of temperature on deformation and fracture behaviour of high-strength rail steels[1]

2.1 Introduction

The frequency of cleavage fracture in continuously welded rails (CWR) elevates with the increase of heavy axle load (HAL) and high speed operations. The cleavage fracture of rails causes train derail, thus a severe safety concern. For this reason, lots of efforts have been made in the last 40 years to improve the rail steel, through approaches such as refining metallurgy and thermo-mechanical processes [97]. Although the improvement has been significant, cleavage fracture is still the major problem for the rail track due to the inherent poor toughness of the pearlite microstructure [14]. The problem is worsened in the cold regions due to a combined effect of HAL and contraction and fracture toughness reduction of rail at low temperature [98]. This has driven renewed interests in characterizing mechanical properties for the newly developed high-strength rail steels. In the previous studies, Szablewski et al. [99] evaluated mechanical properties for 10 premium and 8 intermediate hardness rail steels in both head and foot regions at room temperature, to investigate the potential variation in mechanical properties over the cross section. Wang et al. [100] measured fracture toughness for rail steels at low temperature, but only in the head region. Bandula-Heva and Dhanasekar [101] focused on establishing a true stress-strain relationship for the head region of the rail steels at room temperature, but did not consider the possibility of neck formation before the fracture. In fact, to our knowledge, a comprehensive study on all of the above material properties over the entire cross section of high-strength rail steel is scarce in the literature. In view of the extremely harsh winter condition in Canada, with the temperature dropping

[1] This chapter has been published in the following publication:
Yu, F., Jar, P.-Y.B., Hendry, M., 2015. Effect of temperature on deformation and fracture behaviour of high-strength rail steel. Engineering Fracture Mechanics 146, 41-55.

possibly down to -40°C, it is desirable to evaluate all of those mechanical properties for the newly developed high-strength rail steels at the rail head, web, and foot at low temperature.

Due to the complex procedures involved in the rail steels production [1], material properties may vary over the rail cross section [99]. In this study, true stress-strain relationship, mode I critical stress intensity factor (K_{Ic}), and Vickers hardness on rail head and foot are investigated at 23, -10, and -40°C. K_{Ic} is also determined in the web region. In view that the new generation of high-strength rail steel may involve necking before the onset of tensile fracture, the conventional test-based approach to determine the true stress-strain curve is no longer valid, especially in the strain range after the peak load [102]. Bridgman [103] proposed a revised formula to convert the results from the mechanical testing to the material true stress-strain curve, while others through the combination of mechanical testing and FE analysis [104-107]. In the present work, the latter approach is used to establish the entire true stress-strain curve for tensile loading of a high-strength rail steel (CZECH TZ IH) under large plastic deformation including necking. The true stress-strain curve is then applied to an FE model of Vickers indentation test to mimic the experimentally determined load-depth curve. The chapter also discusses the relevance of the results with those reported in the literature.

2.2 Mechanical testing and simulation

All the mechanical testing was conducted on specimens sampled from the high-strength rail steel CZECH TZ IH with intermediate hardness, supplied by the Canadian National Railway Company (CN). An Instron hydraulic universal testing machine, equipped with an Instron environmental chamber, was used for the uniaxial tensile and three-point bending tests at temperatures controlled by the environmental chamber. A LEITZ MINILOAD hardness tester was used to

measure the Vickers hardness. Specimen temperature for the Vickers hardness measurement was controlled using a custom-made cooling chamber, manufactured following the design described by Oku et al. [108]. Additional thermocouples were welded on each specimen for all three types of tests to ensure that temperature of the specimen reached the specified value before the tests were conducted.

In addition to the above mechanical testing, FE modelling using ABAQUS Standard (version 6.11) was performed to establish the constitutive equation for tensile deformation at 23, -10, and -40^{o}C. The FE modelling was also used to mimic the Vickers indentation test at those temperatures.

2.2.1 Mechanical testing

2.2.1.1 Uniaxial tensile test

Figure 2.1 presents geometry and dimensions for the tensile specimens, and location on the rail cross section where the specimens were sampled. The specimens were machined from the head and foot sections of the rail steel with the longitudinal direction parallel to the rolling direction. Thus, the gross fracture plane was perpendicular to the rolling direction in each test. Due to high-strength of the rail steel, diameter in the gauge section was chosen to be 6.0 mm so that the maximum load did not exceed the load cell capacity of the test machine. The length of the central section conformed to the ASTM E8/E8M [17], that is, more than 5 times of the diameter. During the tensile tests, no imperfection was introduced to control the location of necking and fracture.

The uniaxial tensile tests were performed at temperatures -40, -10 and 23^{o}C, using the environmental chamber to control the temperature to be within ±1^{o}C from the targeted value. In addition, a thermocouple was welded at the bottom nose of the reduced gauge section to ensure that the targeted temperature was reached before commencing the test. Three repeated tests were conducted at a

crosshead speed of 8.5×10^{-3} mm/s, equivalent to an initial strain rate of 2.36×10^{-4} /s. Figure 2.2(a) shows the specimen after fracture during the test, which depicts the fracture location to be outside the section covered by the axial extensometer. Figure 2.2(b) presents one set of the post-test tensile specimens, none of which had fracture occurred in the middle of the reduced gauge section. In addition to the axial extensometer, a diametric extensometer, also shown in Figure 2.2(a), was used to measure the diameter change in the middle of the gauge section. Since neither of the extensometers recorded the dimensional change during the necking process, the equivalent stress-strain relationship for the entire deformation process, including necking, was established using the FE modelling, as to be described in section 2.2.2.

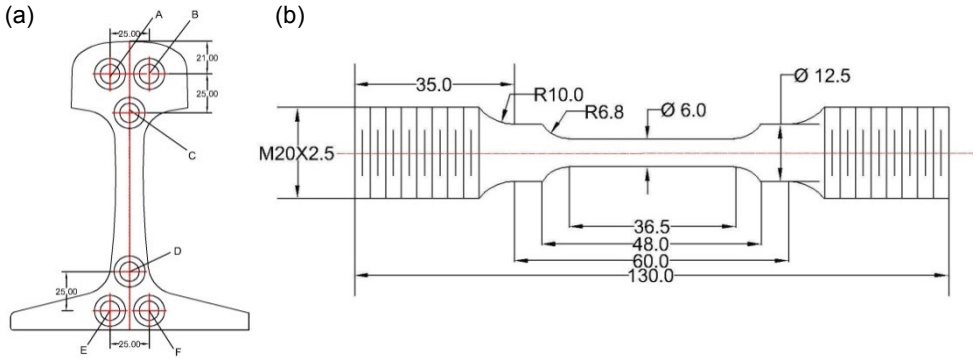

Figure 2.1 Sampling location for tensile specimens on the rail cross section (a) and dimensions and geometry of the uniaxial tensile specimens (b)

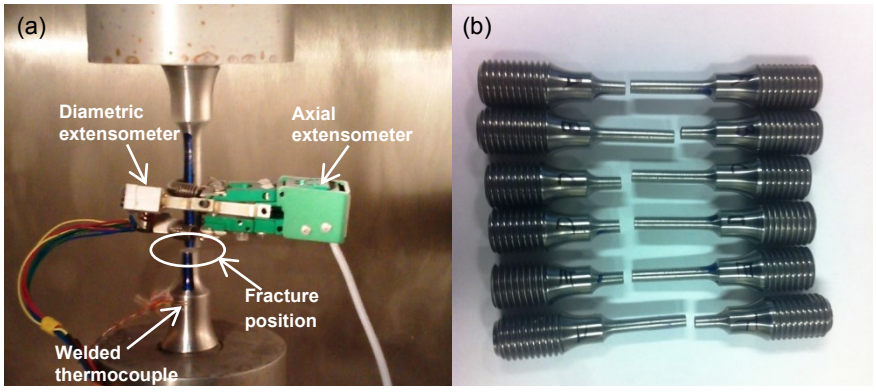

Figure 2.2 Uniaxial tensile test set-up (a) and one set of fractured tensile specimens (b)

2.2.1.2 Three-point bending test

The single-edge-notched bend (SENB) specimens were machined from the head, web, and foot of the high-strength rail steel CZECH TZ IH, at locations shown in Figure 2.3(a). Longitudinal direction of the specimens was along the rolling direction of the rail. Geometry and dimensions of the SENB specimens followed the specifications provided in the ASTM E399 [18], with thickness ($\bar{B}$), width (W) and span length ($\bar{S}$) being 12.5, 25 and 108 mm, respectively, as shown in Figure 2.3(b). The edge notch was first water-jetted and then the notch length was increased using electric-discharge machining (EDM). Pre-cracking was introduced at the notch tip through cyclic loading. The total crack length was controlled to be in the range of 0.5 to 0.53 of the specimen width (W).

In order to ensure the reliability of the measured fracture toughness at each temperature, a minimum of six SENB specimens were tested for each of the rail head, web, and foot regions. As shown in Figure 2.4, a clip-on extensometer was mounted to the mouth of the notch before each test and an additional thermocouple welded nearby the crack tip to monitor the specimen temperature. Crosshead speed for the SENB tests was set at 2×10^{-3} mm/s.

Figure 2.5 presents a sample curve of load, P, versus crack mouth opening displacement (CMOD), δ, to demonstrate the characteristics of cleavage fracture for the high-strength rail steel. The provisional load, P_Q, is determined by following the procedures specified in the ASTM E399 [18]. The value for K_Q was calculated using the following equations:

$$K_Q = \frac{P_Q \bar{S}}{\bar{B} W^{3/2}} . f\left(\frac{a_0}{W}\right) \tag{2.1}$$

$$f\left(\frac{a_0}{W}\right) = 3\sqrt{\frac{a_0}{W}} . \frac{1.99 - \left(\frac{a_0}{W}\right)\left(1-\frac{a_0}{W}\right)\left[2.15 - 3.93\frac{a_0}{W} + 2.7\left(\frac{a_0}{W}\right)^2\right]}{2\left(1+2\frac{a_0}{W}\right)\left(1-\frac{a_0}{W}\right)^{\frac{3}{2}}} \tag{2.2}$$

where, K_Q is the conditional stress intensify factor and a_0 the average initial pre-crack length measured along the crack front after the specimen was fractured.

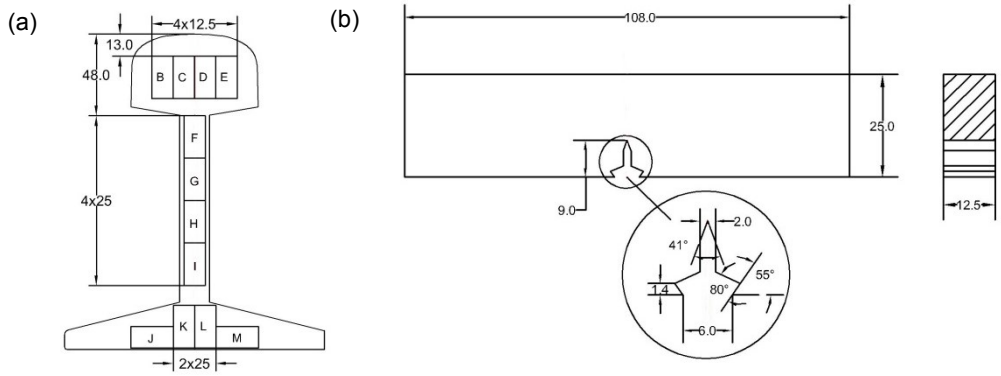

Figure 2.3 Sampling location over the cross section of the rail (a) and dimensions of the SENB specimen (b)

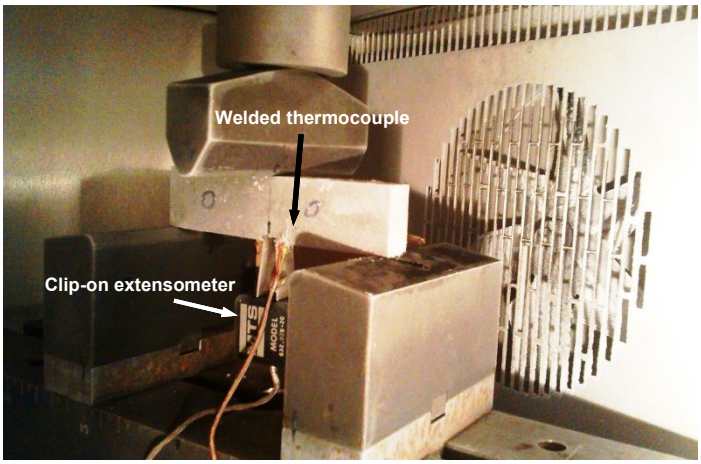

Figure 2.4 Set-up of the SENB test

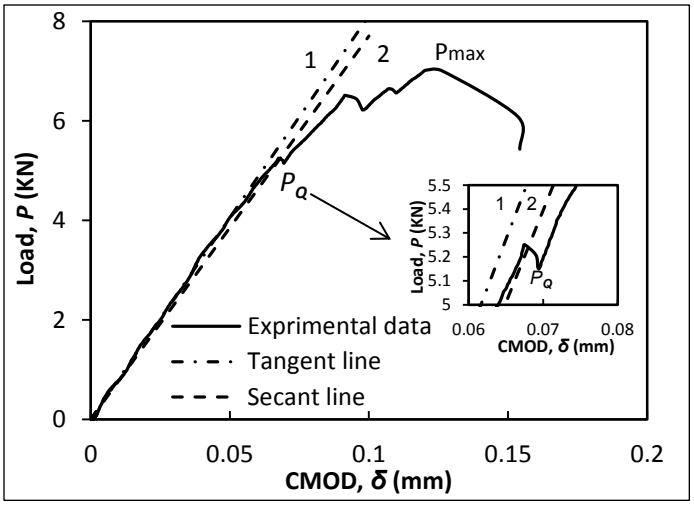

Figure 2.5 A typical load-displacement (P-δ) curve for the SENB specimens of rail steel, and auxiliary lines, marked 1 and 2, to determine P_Q

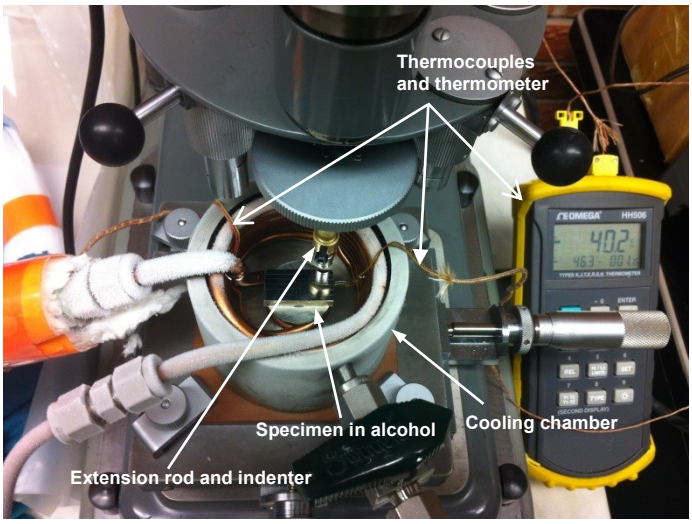

Figure 2.6 Test set-up, including the cooling chamber, for Vickers hardness test

2.2.1.3 Vickers hardness test

Specimens for the Vickers hardness test were cut from the post-tested SENB specimens on rail head and foot. Surface for the Vickers hardness test was gradually polished to a mirror-like finish using an alpha alumina polishing powder of 0.05μm at the final polishing step.

Figure 2.6 shows the apparatus for the Vickers hardness test, including the custom-made cooling chamber, a brass extension rod and an indenter with a 136° pyramidal diamond tip. The Vickers hardness tests at room temperature conformed to the ASTM E384 [19], while for the low-temperature tests, the polished specimens were welded with a thermocouple and bathed in the custom-made cooling chamber that had been filled with anhydrous ethanol to prevent the frost from building up and to keep the temperature uniform on the specimen surface. Two thermocouples were used to monitor the temperatures, one in the fluid and the other on the specimen. Before the test, the cavity inside the chamber wall was vacuumed and liquid nitrogen circulated in the copper coil placed in the chamber until the desired temperature was reached. A needle valve was used to control the flow rate of the liquid nitrogen and thereby to maintain the temperature to be within ± 0.5^{o}C from the aimed temperature.

The hardness test was conducted by first placing the indenter tip about 0.5mm above the specimen surface, and then applying one of the six pre-selected loading levels (100, 200, 300, 500, 1000, and 2000 gf) for a period of 30 seconds. After the load was removed, the specimen surface was quickly dried with a hot air gun and the diagonal length of the indent, generated by the pyramid indenter, was measured at room temperature using an optical microscope at a magnification of 400. The Vickers hardness value was then calculated using the following expression:

$$HV = (1854.4 \times F)/l^2 \tag{2.3}$$

where, F is the load in gram force, and l the mean diagonal length of the indent in μm.

2.2.2 FE modelling

The average true stress-strain curve determined directly from the experimental testing is often used to represent the constitutive equation for metallic materials under uniform deformation. Such a curve, however, is insufficient for large deformation when necking is involved in the deformation process. For CZECH TZ IH, since neck was formed before fracture, Eq. (2.4) that consists of four expressions had to be used to represent the constitutive equation in order to mimic the deformation behaviour for the entire strain range, including the necking, while minimizing the number of parameters in each expression. Caution was taken to ensure that continuity in the 0^{th} and 1^{st} order was met between the expressions at the coincident points among the four expressions.

$$\sigma_{eq}(\varepsilon_{eq}) = \begin{cases} \frac{3}{2(1+\nu)} E_0 \varepsilon_{eq} & \varepsilon_{eq} \le \varepsilon_l \ (a) \\ e + d\left\{\left[a(\varepsilon_{eq}+b)\right]^{(c-1)} - \left[a(\varepsilon_{eq}+b)\right]^{(-c)}\right\} & \varepsilon_l \le \varepsilon_{eq} \le \varepsilon_y \ (b) \\ \bar{\beta} - (\bar{\beta}-\alpha)exp(-\gamma\varepsilon_{eq}) & \varepsilon_y \le \varepsilon_{eq} \le \varepsilon_n \ (c) \\ M(\varepsilon_{eq})^n & \varepsilon_{eq} \ge \varepsilon_n \ (d) \end{cases} \quad (2.4)$$

where, σ_{eq} is the equivalent stress in MPa, ε_{eq} the equivalent strain, ε_l the linear elastic strain, ε_y the yield strain, ε_n the strain for the on-set of necking, ν the Poisson's ratio and the rest of the parameters (*a, b, c, d, e, α, β̄, γ, M*, and *n*) the user-defined parameters for which values are determined through iteration.

The first two expressions in Eq. (2.4) are for the elastic deformation. Hooke's law is adopted for the linear elastic part and the Ogden's equation [109] to represent the nonlinear elastic part before the yielding point. The third expression known as the Voce equation [110], covers the deformation behaviour from the yield point to the end of uniform deformation in the gauge section. The fourth expression is a power law function, also known as Hollomon equation [111], and is to represent the deformation behaviour from the neck formation to fracture.

Since deformation in the necking region was not recorded by the two extensometers, the criteria used to evaluate the suitability of the constitutive equation were based on following information obtained from the mechanical testing.

a) On the load-elongation curve: (i) the Young's Modulus and variation of load vs. elongation up to the peak point, and (ii) the curve profile during the load drop phase (i.e. after the necking starts).

b) On the cross-section reduction: (i) the variation of diameter at the middle of the reduced gauge section up to fracture, and (ii) the diameter at the minimum cross section (after fracture)

A two-dimensional (2-D) axisymmetric FE model, with dimensions following those given in Figure1, was generated to calibrate parameters in Eq. (2.4) so that deformation generated by the FE model meets the above criteria. The FE model had 6,392 axisymmetric 8-node elements and 20,173 nodes. The boundary condition was set to be the same as the experimental condition, i.e., with one end fixed in direction 2 and the other end moving at a constant crosshead speed of 8.5×10^{-3} mm/s. Figure 2.7(a) shows the mesh pattern and Figure 2.7(b) an example of the typical necking behaviour generated by the FE model. The necking was introduced at the location where the fracture occurred in the experiments by reducing its diameter by 0.1%.

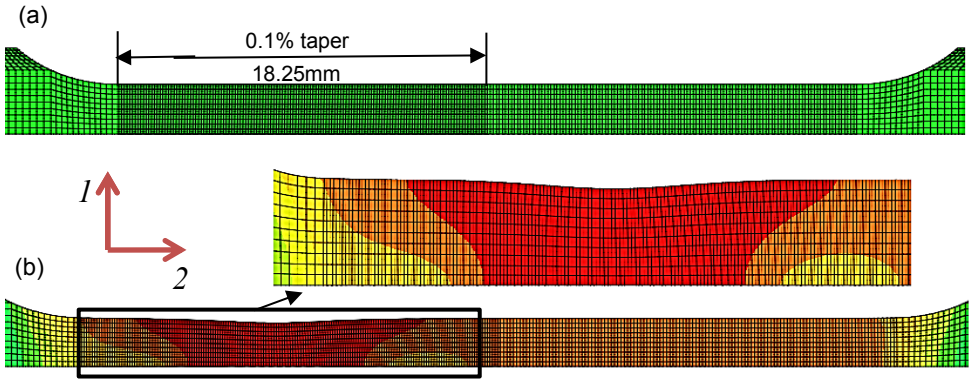

Figure 2.7 The FE model of tensile testing: (a) the mesh pattern and (b) an example of the neck formation

2.3 Results

2.3.1 True stress-strain relationship in tension

2.3.1.1 Mechanical testing results

Engineering stress-strain curves at all three temperatures are shown in Figure 2.8(a) and 2.8(b) for rail head and foot, respectively. Due to the good repeatability of the test results, each of the curves in Figure 2.8 is representative of results from the three tests in the same condition. Note that because the two extensometers did not cover the region where necking occurred, each engineering stress-strain curve in Figure 2.8 shows a sudden drop after the maximum load, which is different from the conventional engineering stress-strain curve that shows a gradual decrease of load after the maximum loading point [102]. The sudden load drop in Figure 2.8 is due to the localized deformation in the necked region, which causes the load drop but not the increase in elongation outside the necked region.

Curves of the corresponding average true stress versus logarithmic strain are shown in Figure 2.9(a) and 2.9(b) for rail head and foot, respectively, in which the continuous section corresponds to the loading section of Figure 2.8 up to the peak load, and the single points represent the final fracture points at each temperature. Note that values for the fracture stress (σ_f) and fracture strain (ε_t^f) for those single points were determined using the following two expressions, with the assumption of volume conservation and uniform stress across the minimum cross section during the deformation.

$$\sigma_f = L_f / A_t^f \tag{2.5}$$

$$\varepsilon_t^f = \ln(A_0 / A_t^f) = \varepsilon_e^f + \varepsilon_p^f \tag{2.6}$$

where, L_f is the load recorded at the onset of fracture, A_t^f the minimum cross sectional area including the elastic and plastic parts measured right before the onset of fracture, A_0 the original cross sectional area in the reduced gauge section, ε_e^f the recovered elastic strain, and ε_p^f the plastic strain measured from the fractured tensile specimen.

From Eq. (2.6), A_t^f can be expressed as:

$$A_t^f = A_o \exp[-(\varepsilon_e^f + \varepsilon_p^f)] \tag{2.7}$$

With an additional assumption of uniaxial loading at the fracture point, i.e., $\sigma_f = E_0 \varepsilon_e^f$, substituting A_t^f from Eq. (2.7) into Eq. (2.5) yields

$$(F_f / A_0)\exp(\varepsilon_e^f + \varepsilon_p^f) = E_0 \varepsilon_e^f \tag{2.8}$$

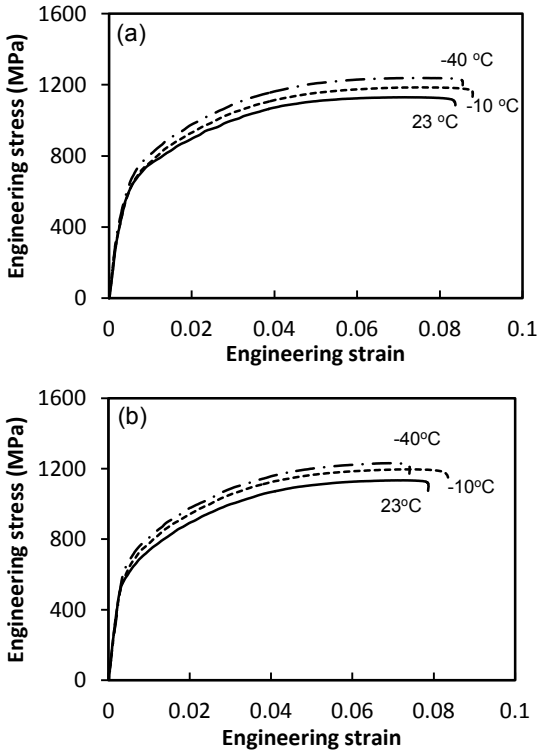

Figure 2.8 Engineering stress-strain curves at temperatures 23, -10, and -40°C for the rail head (a) and rail foot (b)

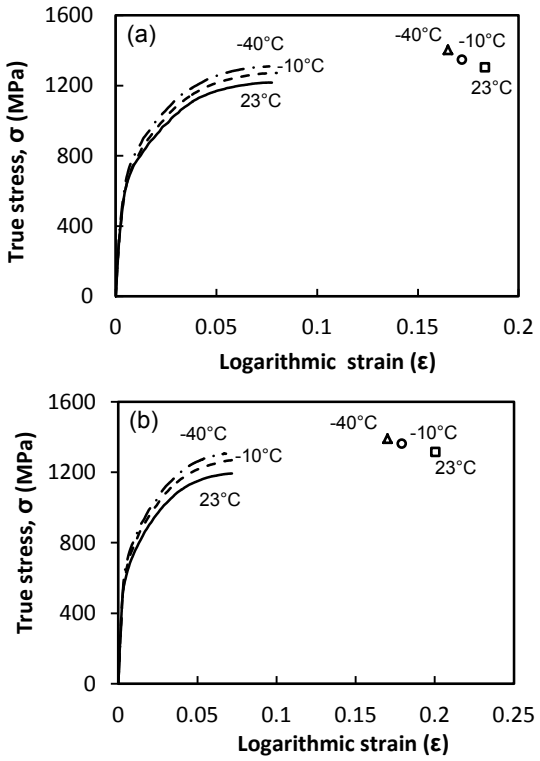

Figure 2.9 Curves of average true stress vs. logarithmic strain for rail head (a) and rail foot (b) at 23, -10 and -40°C

Table 2.1 Mechanical properties of rail head and foot from tensile tests at 23, -10 and -40°C

(°C)	Rail Head					Rail Foot				
	E_0(GPa)	σ_y(MPa)	σ_{uts}(MPa)	ε_p^f	φ(%)	E_0(GPa)	σ_y(MPa)	σ_{uts}(MPa)	ε_p^f	φ(%)
23	193	632	1130	18.3	16.2	205	635	1135	20.1	17.7
-10	193	638	1185	17.2	15.2	205	647	1197	17.9	15.9
-40	193	679	1230	16.5	14.6	205	692	1232	17.0	15.1

Eq. (2.8) can be used to determine value of ε_e^f at the fracture point, with A_o and ε_p^f measured from the original and post-tested tensile specimens, respectively. Then, A_f can be calculated from Eq. (2.7), based on which the fracture stress, σ_f, and logarithmic strain ε_t^f of those single points can be determined from Eqs. (2.5) and (2.6), and are given in Figure 2.9. As to be presented in section 2.3.1.2, an inverse, iterative method was applied to the FE modelling of tensile tests to

establish the missing section between the continuous curves and the single fracture points at all temperatures considered in this study.

Table 2.1 summarizes fundamental mechanical properties for rail head and foot at each temperature, determined directly from the experimental measurements, including Young's modulus E_0, yield stress σ_y, ultimate tensile stress σ_{uts}, plastic fracture strain ε_p^f, and percentage of maximum area reduction φ. Values in Table 2.1 indicate that at each temperature, mechanical properties for the rail head are quite similar to those for the rail foot except that at room temperature, ductility of the rail foot is about 10% higher than that of the rail head while at low temperatures the difference becomes negligible. Further, the difference in the Young's modulus between the rail head and the rail foot is approximate 5%, consistent with the range of variation reported in the literature [112, 113], caused by the hot rolling process during the rail steels production.

2.3.1.2 Simulation results

The equivalent stress-strain relationship, based on the four constitutive functions in Eq. (2.4) to include both uniform and non-uniform deformation, was established using FE modelling. Three typical simulation attempts (SAs) using different strain-hardening functions were considered to represent the stress-strain relationship of the missing section. The equivalent stress-strain curves of the three SAs are shown in Figure 2.10(a) in which SA1, SA2, and SA3 represent a single Hollomon function, a single Voce function and a combination of Hollomon and Voce functions, respectively. Values for the coefficients in these three types of constitutive functions were selected so that the FE model can regenerate the experimental load-elongation curve for the uniform deformation. Figure 2.10(b) compares the load-elongation curves from the three SAs with the curve obtained from the experiment. As shown in both figures of Figure 2.10, the single Hollomon function (SA1) overestimates the work hardening behaviour, with the tensile load deviating from the experimental value before the maximum load is

reached. Furthermore, necking could not be generated in the FE model based on SA1. The Voce function (SA2), on the other hand, underestimates the work hardening behaviour, leading to an early load drop, as shown in Figure 2.10(b). The FE model based on SA2 also generated the minimum diameter in the necked section that was approximately 30% smaller than that from the experimental measurement. By combining Hollomon and Voce functions (SA3), however, the FE model can generate the load-elongation curve that best fits the experimental measurement, even for the final load drop, as shown in Figure 2.10(b). Therefore, the combination of Voce and Hollomon functions was selected for the FE model to mimic the deformation behaviour during the plastic deformation of the tensile test.

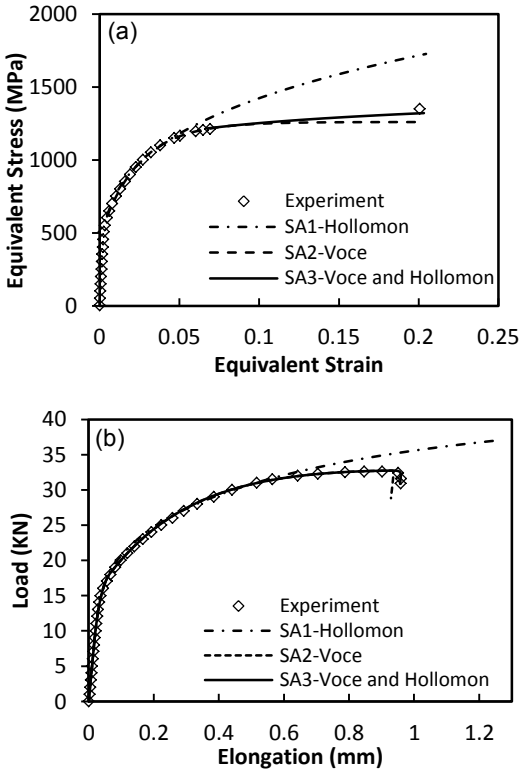

Figure 2.10 Three simulation attempts: (a) three equivalent stress-strain curves including the missing section in Figure 2.9, and (b) comparison of load-elongation curves between the three SAs and the experiment

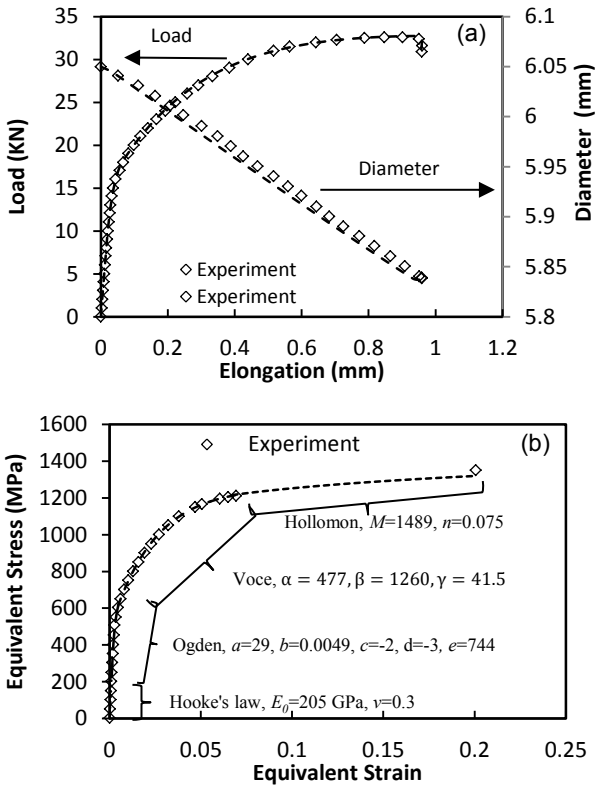

Figure 2.11 Rail foot at 23°C: (a) regeneration of the experimental results from the FE simulation, and (b) the corresponding equivalent stress-strain curve and values for the parameters in Eq. (2.4)

Values for parameters in Eq. (2.4) were finalized by confirming that the FE model could regenerate the load-elongation curve and cross-section reduction obtained from the experiments. Figure 2.11 presents an example for the rail foot at 23°C, in which Figure 2.11(a) illustrates the verification of the FE model by comparing the simulation results with the experimental measurements, and Figure 2.11(b) shows the corresponding parameter values for the four constitutive functions. Values for parameters in the first three constitutive functions were determined simply by the piecewise curve fitting technique based on the average true stress and strain values measured during the uniform deformation, but after the commencement of necking an iterative process was performed for the FE modelling to obtain the accurate stress coefficient M and strain hardening index n for the Hollomon function. In this iterative process, values for parameters in the

first three constitutive functions need to be adjusted slightly to ensure of the continuity in the 0^{th} and 1^{st} order between the functions at the coincident points, as mentioned earlier.

The procedure to determine the parameter values for the Hollomon function is described as follows. Firstly, the missing section of the curves in Figure 2.9 was generated using the stress-strain relationship represented by Eq. (2.4d) with M and n values adjusted so that the transition from the curve generated by the Voce equation to that by the Hollomon equation satisfies both the 0^{th} and 1^{st} order continuity. Secondly, the entire equivalent stress-strain curve generated by the four expressions of Eq. (2.4) was input into the FE model shown in Figure 2.7 to generate the load-elongation curve and the cross-section reduction, which were then compared with the experimental measurements. This process was iterated until results from the FE model met the two experimental phenomena given in section 2.2.2. The same procedure was performed to obtain the true stress-strain curves at all three temperatures for both rail head and rail foot. The final equivalent stress-strain curves are shown in Figure 2.12 and the corresponding values for the parameters in Eq. (2.4) are summarized in Table 2.2.

As shown in Figure 2.12, the Young's modulus of both rail head and foot was little affected by the temperature change from 23 to -40^{o}C. However, the mechanical strength increases and ductility decreases notably with the decrease of temperature. Values for parameters in Table 2.2 suggest that the difference in mechanical strength among the curves in Figure 2.12 is mainly a result of the difference of α and β in the Voce function and stress coefficient M in the Hollomon function. While values for the exponent γ and strain hardening index n for rail head and foot remain almost constant.

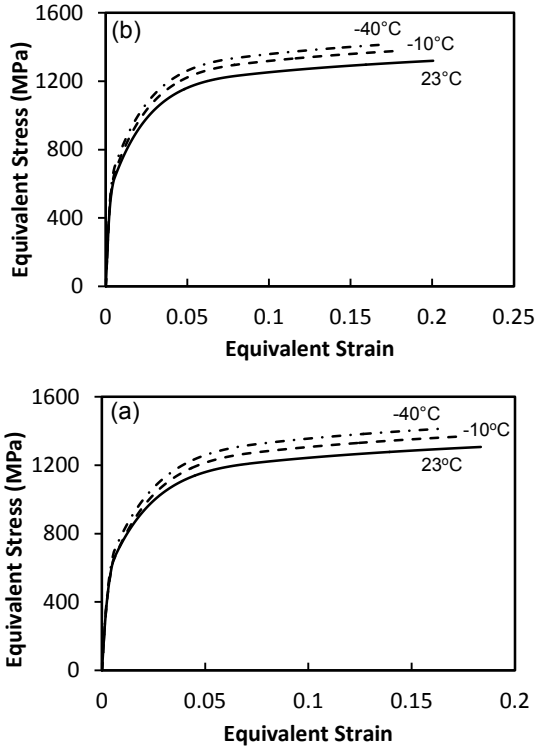

Figure 2.12 The equivalent true stress-strain curves of (a) the rail head, and (b) the rail foot, at temperatures 23, -10 and -40°C

Table 2.2 Parameters in Eq. (2.4) for rail head and foot at all three temperatures

Sections			Head			Foot		
°C			23	-10	-40	23	-10	-40
Parameter	Hooke's law (a)	E_0 (GPa)	193	193	193	205	205	206
		v	0.3	0.3	0.3	0.3	0.3	0.3
	Ogden equation (b)	a (MPa)	30	30	30	29	29	29
		b	0.01	0.01	0.01	0.0049	0.0049	0.0049
		c	-2	-2	-2	-2	-2	-2
		d	-26	-26	-26	-3	-3	-3
		e (MPa)	889	895	937	744	775	821
	Voce equation (c)	α (MPa)	452	478	504	477	495	530
		$\bar{\beta}$ (MPa)	1240	1305	1356	1260	1327	1367
		γ	45.0	45.0	43.5	41.5	41.5	41.5
	Hollomon equation (d)	M (MPa)	1502	1583	1608	1489	1568	1616
		n	0.082	0.083	0.084	0.075	0.075	0.075

2.3.2 Mode I critical stress intensity factor (K_{Ic})

The fracture toughness, K_{Ic}, for the pre-cracked SENB specimens of rail head, web, and foot at all three temperatures are summarized in Table 2.3. The table also includes pre-crack length a_0 and loads P_Q and P_{max} that are needed to validate K_Q for K_{Ic}. As stated in the ASTM E399 [18], the validity of K_{Ic} from K_Q can be confirmed only when the two criteria are satisfied; these are, the ratio of P_{max}/P_Q is smaller than 1.10 and also $2.5(K_Q/\sigma_y)^2$ is less than the specimen ligament length, W-a_0. In Table 2.3, the requirement of $2.5(K_Q/\sigma_y)^2 < W$-a_0 is satisfied for all of the tested SENB specimens. However, for most specimens listed in Table 2.3, their values of P_{max}/P_Q are slightly larger than 1.10, suggesting that limited plastic deformation is generated at the crack tip before the crack growth. Nevertheless, these values are within the range acceptable for evaluating the temperature effect on the plane strain fracture toughness of the CZ rail steel.

As shown in Table 2.3, the K_{Ic} values in each region of rail head, web, and foot show some scattering at all three temperatures. The maximum scattering of the K_{Ic} values for the rail head is 14% of the averaged value (at -40°C), 21% for the rail web (at 23°C), and 18% for the rail foot (also at 23°C). In spite of the scattering, the average K_{Ic} values for the head, web and foot regions, as presented in the right column of Table 2.3, show a clear trend of decrease with the decrease of temperature. The average K_{Ic} values for rail head, web, and foot as well as the standard deviation at each test temperature are listed in Table 2.3. It is clearly shown that for the rail steel studied, the average K_{Ic} values are the highest in the web and lowest in the head, and that K_{Ic} drops continuously with the decrease of temperature from 23 to -40°C. Overall, the decrease of temperature from 23 to -40°C reduces K_{Ic} by approximately 20%.

Table 2.3 K_{Ic} for rail head, web, and foot at temperature 23, -10, and -40°C

Rail section	T °C	Label	a_0 mm	P_Q kN	P_{max} kN	K_Q MPa·m$^{1/2}$	$2.5(K_Q/\sigma_y)^2$ mm	P_{max}/P_Q	K_{Ic} MPa·m$^{1/2}$	K_{Ic} MPa.m$^{1/2}$ (STD)
		B	12.29	6.51	8.97	33.96	7.22	1.38	33.96	34.26

		C	12.56	6.22	8.03	33.21	6.90	1.29	33.21	(0.84)
	23	C	13.27	5.63	7.30	33.73	7.12	1.30	33.73	
		D	12.86	6.22	7.64	34.97	7.65	1.23	34.97	
		E	13.50	5.71	7.34	35.50	7.89	1.29	35.50	
		E	12.55	6.34	8.10	34.20	7.32	1.28	34.20	
		B	12.62	5.61	6.95	30.58	5.74	1.24	30.58	30.06
		C	13.13	5.25	7.01	30.20	5.60	1.33	30.20	(0.66)
	-10	C	12.80	5.33	6.68	30.05	5.55	1.25	30.05	
		D	13.42	4.74	6.20	28.77	5.08	1.31	28.77	
Head		E	13.04	5.28	7.01	30.53	5.72	1.33	30.53	
		E	12.68	5.50	6.97	30.21	5.61	1.27	30.21	
		B	12.53	4.99	6.42	26.92	3.93	1.29	26.92	27.96
		C	13.20	4.92	5.68	28.62	4.44	1.16	28.62	(1.37)
	-40	C	12.66	5.43	5.92	29.94	4.86	1.09	29.94	
		D	13.52	4.30	5.79	26.07	3.69	1.35	26.07	
		E	12.49	5.19	6.57	27.67	4.15	1.27	27.67	
		E	12.56	5.28	6.10	28.53	4.41	1.16	28.53	
		F	12.70	6.34	7.96	34.88	7.61	1.26	34.88	36.03
	23	G	12.60	6.08	7.82	33.02	6.82	1.29	33.02	(2.87)
		H	12.94	6.25	7.45	35.69	7.97	1.19	35.69	
		H	12.85	6.44	7.93	35.82	8.038	1.23	35.82	
		I	13.59	6.64	7.21	40.76	10.40	1.09	40.76	
		F	13.05	5.85	6.75	33.45	6.89	1.15	33.45	31.95
		F	12.78	5.73	6.89	31.91	6.27	1.20	31.91	(1.29)
	-10	G	12.94	6.12	6.48	32.20	6.39	1.06	32.20	
Web		G	12.64	5.56	6.79	30.65	5.79	1.22	30.65	
		H	13.26	5.16	6.93	30.28	5.65	1.34	30.28	
		H	12.82	5.94	6.89	33.20	6.79	1.16	33.20	
		F	13.28	4.80	5.56	28.21	4.32	1.16	28.21	29.19
		F	12.76	5.23	5.92	29.00	4.56	1.13	29.00	(2.14)
		G	14.10	4.98	5.50	32.95	5.89	1.10	32.95	
	-40	G	12.98	5.50	6.09	31.19	5.28	1.11	31.19	
		G	12.65	5.08	6.00	27.93	4.23	1.18	27.93	
		H	12.46	5.31	6.44	28.30	4.34	1.21	28.30	
		I	13.28	4.53	5.75	26.75	3.88	1.27	26.75	
		J	13.02	5.98	8.02	34.07	7.20	1.34	34.07	35.20
		J	12.80	6.48	8.27	36.03	8.05	1.28	36.03	(2.37)
	23	K	13.14	6.43	7.24	37.08	8.52	1.13	37.08	
		K	12.64	5.99	7.99	32.58	6.58	1.33	32.58	
		L	12.87	5.67	7.16	32.08	6.38	1.26	32.08	
		M	12.91	6.87	7.60	38.50	9.19	1.11	38.50	
		M	12.57	6.60	7.82	36.05	8.06	1.19	36.05	
		J	12.97	4.97	6.84	28.25	4.77	1.38	28.25	30.74

		J	12.64	6.12	7.21	32.97	6.49	1.18	32.97	(1.71)
Foot	-10	K	13.27	5.44	6.52	31.89	6.07	1.20	31.89	
		K	12.78	5.43	6.96	30.08	5.40	1.28	30.08	
		L	12.52	5.42	6.80	29.14	5.07	1.25	29.14	
		M	12.88	5.50	6.77	30.65	5.61	1.23	30.65	
		M	12.64	5.91	7.44	32.18	6.18	1.26	32.18	
		J	12.76	5.63	6.35	27.63	3.99	1.13	27.63	28.46
		J	12.55	5.26	6.64	28.30	4.18	1.26	28.30	(0.73)
	-40	K	12.78	5.21	6.11	29.24	4.46	1.17	29.24	
		L	12.55	4.99	5.92	28.34	4.19	1.19	28.34	
		L	12.96	5.16	6.30	27.48	3.94	1.22	27.48	
		M	12.95	5.18	6.11	29.19	4.45	1.18	29.19	
		M	12.69	5.30	6.12	29.06	4.41	1.15	29.06	

2.3.3 Vickers hardness

2.3.3.1 Test results

Vickers hardness tests were conducted in two stages. The first stage was to apply a specified load of 2000 gf on rail head and foot to identify the hardness distribution on the rail cross section at room temperature. As shown in Figures 2.13(a) and 2.13(b), the test area was where SENB specimens were sampled for the fracture toughness measurement. Figure 2.13 suggests that the rail foot is slightly harder than the rail head, which is consistent with the tensile strength shown in Table 2.1. Figure 2.13 further suggests that the hardness distribution is relatively uniform in the rail head and foot, with insignificant change from the core to the edge.

The second stage of the hardness tests was to investigate the relationship between indentation load and depth by applying six loading levels (100, 200, 300, 500, 1000, and 2000 gf) using the Vickers hardness tester. Figure 2.14 shows the typical indentation shape under the six loading levels, of which the mean diagonal length and the corresponding loading level were used to determine the Vickers hardness value, *HV*, through Eq. (2.3). In view of the relatively uniform distribution of hardness in the rail head and foot regions for CZECH TZ IH, the

hardness values in each region were deemed to be insensitive to the location selected for the test. As a result, all hardness values at the same indentation load in each of the head and foot regions were grouped together to determine the average values. In this study, 16 tests were conducted at a given load and temperature in the head or foot regions. That is, totally 96 tests were performed to construct the curve of indentation load versus depth in the head or foot region at a given temperature, which are summarized in Figure 2.15. The indentation depth is ideally 1/7 of the mean diagonal length of the pyramid indenter used in this study [114]. As shown in Figure 2.15, decrease of the test temperature results in decrease of the indentation depth at each loading level, but only slightly. Furthermore, the amount of decrease in the indentation depth is smaller at a lower loading level.

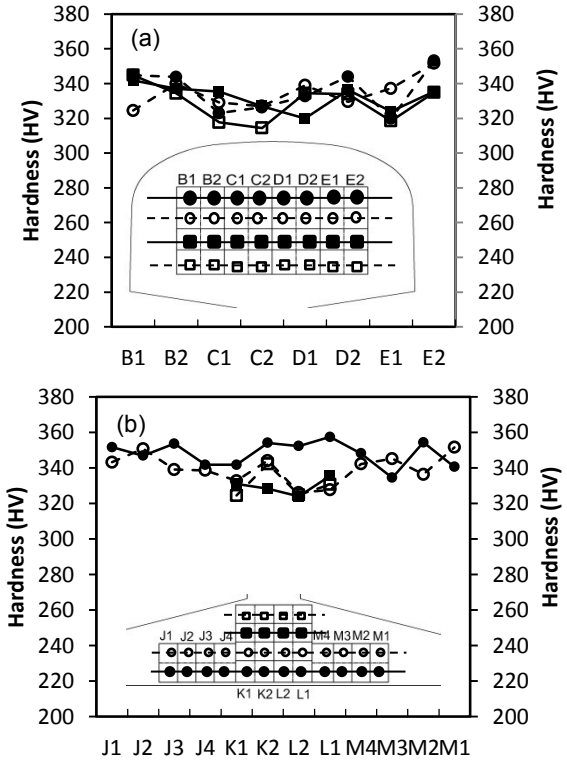

Figure 2.13 Vickers hardness distribution on rail head (a) and rail foot (b) at 23^{o}C

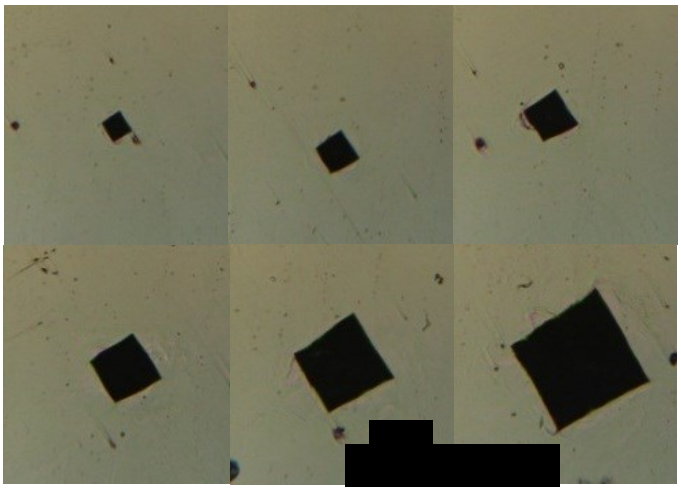

Figure 2.14 The indentation shape under six loading levels from 100 to 2000 gf

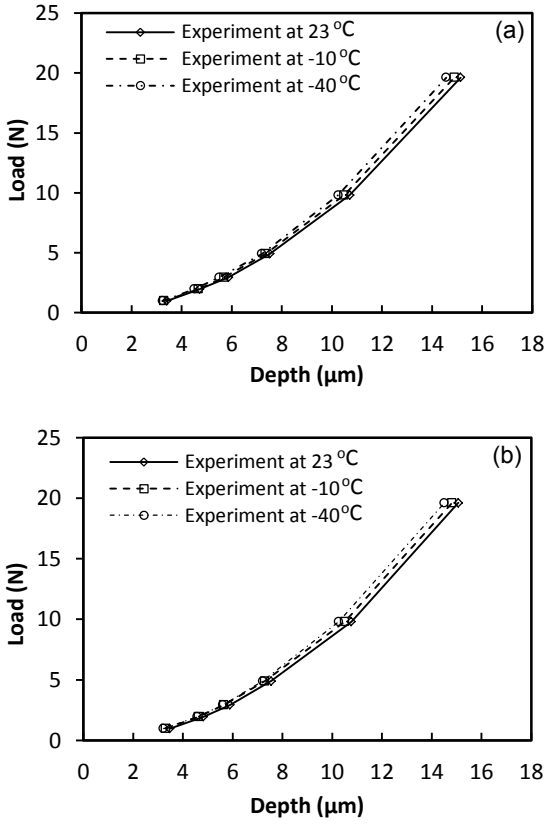

Figure 2.15 The relationship between indentation load and depth for (a) the rail head, and (b) the rail foot

Figure 2.16 summarizes the effect of temperature on the Vickers hardness for the rail head (solid symbols) and the rail foot (open symbols), measured at the six loading levels. The figure suggests that Vickers hardness increases with the drop of temperature from 23 to -40^{o}C, for both rail head and rail foot, but difference in the Vickers hardness between the two regions is quite small, of which the maximum is 5% at the small loading levels. Figure 2.16 also shows clearly that at each temperature the Vickers hardness decreases with the increase of load from 100 to 1000 gf, and then the Vickers hardness becomes relatively constant with further load increase from 1000 to 2000 gf. A similar phenomenon has been previously reported [115].

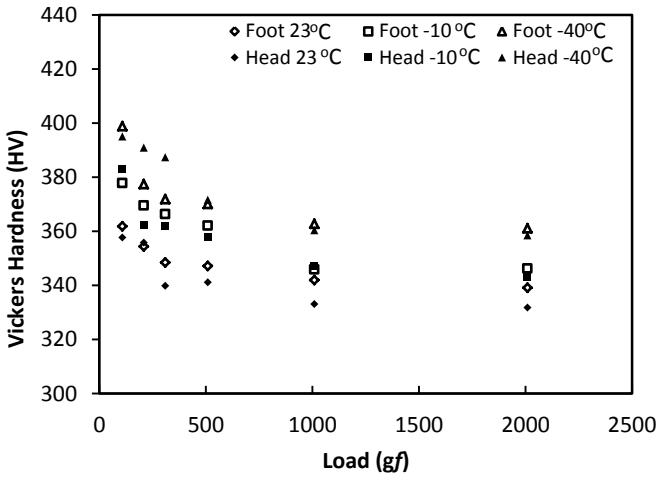

Figure 2.16 Effect of temperature on the Vickers hardness for both the rail head and foot

2.3.3.2 FE simulation of Vickers indentation

The constitutive equation established for the tensile test was applied to the FE model for the Vickers indentation test, to explore the possibility of regenerating the indentation load-depth curve shown in Figure 2.15.

The FE model for Vickers indentation is shown in Figure 2.17(a). Due to symmetry, only a quarter of the specimen and the indenter are considered. The

Vickers indenter is modelled as a rigid body of a pyramid shape with an angle of 136°. The specimen consists of 45,957 eight-node brick elements and 49,738 nodes. In the contact region, size of the elements is reduced to 2μm and the contact is regarded as frictionless [116]. Bottom surface of the specimen is constrained in the indentation direction (*y*-axis). Symmetric constraints are applied on surfaces 1 and 2, in *x* and *z* directions, respectively. Figure 2.17(b) shows a contour plot of von Mises stress generated by the indentation, suggesting that deformation introduced by the indentation is highly localized around the indenter. Therefore, size of the FE model is sufficient to act as a semi-infinite body without any influence of the boundary condition at the bottom surface on the simulation results.

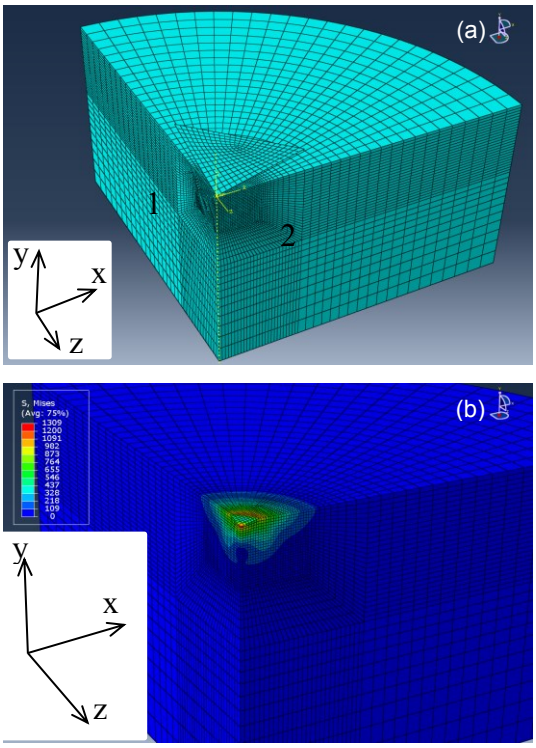

Figure 2.17 The FE model of Vickers indentation test: (a) the model, and (b) the contour plot of von Mises stress showing the localized deformation.

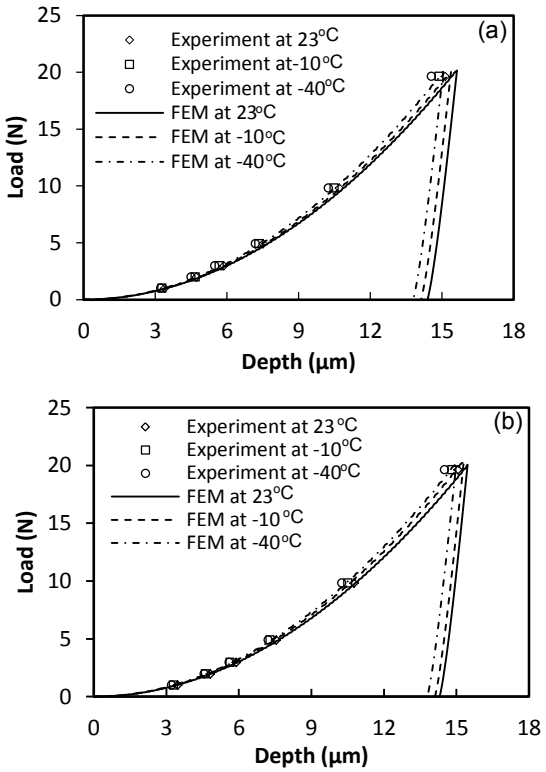

Figure 2.18 The experimental and computational indentation load-depth curves of rail head (a) and rail foot (b) at temperatures 23, -10, and -40°C

Figure 2.18 compares the indentation load-depth curves from the FE model (lines) with those from the experiments (symbols) at the three temperatures, for the rail head in Figure 2.18(a) and the rail foot in Figure 2.18(b). The figure suggests that at each temperature, the experimentally-determined load is slightly higher than the FEM counterpart at the same indentation depth. Otherwise, the trend with the temperature change from the FE simulation is the same as that from the experiments. That is, the indentation depth decreases with the decrease of the temperature from 23 to -40°C.

2.4 Discussion

Results indicate that mechanical properties for CZECH TZ IH are relatively uniform on the cross section, without much difference between the rail head and

the rail foot, unlike other high-strength rail steels [99]. The noticeable difference in mechanical properties between the rail head and foot is Young's modulus and ε_p^f at room temperature, about 5% and 10%, respectively, as shown in Table 2.1. The difference in Young's modulus is probably caused by the difference in the hot rolling process [112, 113], and ε_p^f by the cooling rate. Study by Alexander and Bernstein [117] has suggested that the relatively slow cooling rate in the core region of the rail head increases the interlamellar spacing of the pearlite, which results in the ductility reduction at fracture.

Although K_{Ic} in Table 2.3 shows some scattering, the averaged K_{Ic} values clearly suggest that the fracture toughness decreases with the decrease of temperature. In view that the theoretical prediction of the measured K_{Ic} scattering from the SENB test in cleavage fracture should be around 20% of its mean value [118], the scattering of K_{Ic} in Table 2.3 is believed to be due to the intrinsic nature of the experimental measurement, not reflecting any significant variation of fracture toughness on the cross section of the rail steel studied here.

It is worth mentioning that although the load-depth curves in Figure 2.18 show only a small difference between the experimental results and the FE simulation, it has long been questioned about the suitability of applying the true stress-strain curve from the uniaxial tensile test to modelling the material deformation in the indentation test. In general, indentation generates a multi-axial, compressive stress state, in contrast to the uniaxial, tensile stress state generated in the tensile test. Therefore, the difference between experimental and simulation results in Figure 2.18 may have been caused by the strength differential effect between tension and compression [119]. Although uniaxial compressive test has been suggested in some work to establish the proper stress-strain relationship for FE modelling of the indentation test [120, 121], the tensile stress-strain relationship has actually been satisfactorily used for this purpose in the literature [122, 123]. Since the FE simulation conducted in our study was performed using commercial software based on classical von Mises yield function and isotropic

hardening, no difference is expected between the tensile and compressive yield behaviours. Therefore, it is reasonable to apply the true stress-strain curve established from the uniaxial tensile test to the FE modelling of Vickers indentation test.

In spite of the small difference between the experimental measurement and the FE simulation in Figure 2.18, which is less than 8% for the indentation depth, the difference may not be negligible. Further study is being conducted to examine how the indentation load-depth curve can be changed if the constitutive equation is based on the compressive test results. Nevertheless, we do not expect any significant change from that shown in Figure 2.18 in view that the constitutive equations with very different work hardening behaviour have been reported to generate similar indentation loading-unloading curves from the FE modelling [124].

2.5 Conclusions

The effect of temperature on the mechanical properties at head and foot regions of high-strength rail steel, CZECH TZ IH, has been investigated. The results suggested similar equivalent stress-strain relationship for rail head and rail foot at all three temperatures of 23, -10, and -40^{o}C. FE modelling was used to establish the true stress-strain relationship for large deformation including necking, which was verified by both experimental load-elongation curve and cross-section reduction. The work found that a combined Voce and Hollomon function can provide an accurate expression for the true stress-strain curve under large plastic deformation of the rail steel.

Fracture toughness, in terms of K_{Ic}, was determined over the cross section of the rail steel. Due to the nature of cleavage fracture at the crack tip, the resulted K_{Ic} values show some scattering but the scattering is still within the expected range. The results show a clear effect of temperature on the K_{Ic} values, with an

approximate 20% reduction of K_{Ic} for rail head, web, and foot with the decrease of temperature from 23 to -40^{o}C.

Vickers hardness tests were performed both experimentally and in FE simulation. The former was to study the influence of temperature on the hardness variation. The test results suggest that both rail head and foot show relatively uniform hardness distribution and the Vickers hardness value increases by about 9% with the decrease of temperature from 23 to -40^{o}C. The Vickers hardness values were also found to decrease with the increase of the indentation load at micro loading range, which is consistent with that reported in the literature. The FE modelling was used to explore the possibility of applying the true stress-strain curves established from the tensile test to the indentation tests. The results suggest that the stress-strain relationship provides a reasonable, but slightly different indentation load-depth curve from that obtained experimentally. This is probably because of the complex multi-axial compressive loading that is not considered in the true stress-strain curve for the FE simulation. Further study will be conducted to clarify this issue.

Chapter 3 Fracture behaviour at the sharp notch tip of high-strength rail steels - Influence of stress triaxiality[2]

3.1 Introduction

For metallic materials, results from both theoretical and experimental studies have demonstrated the strong dependence of fracture strain on stress triaxiality [125-128]. Influence of stress triaxiality on fracture strain has often been evaluated using circumferentially-notched tensile specimens, with stress triaxiality value determined from the Bridgman's formula [103]. These studies led to the establishment of a failure envelope [129] that depicts the reduction of fracture strain with the increase of stress triaxiality. However, the Bridgman's formula does not take into account material properties or change in specimen geometry during the test. In view of these problems, recent studies have relied on finite element (FE) modelling to determine the stress triaxiality, using the realistic material properties as the input to the FE model. The FE modelling can also determine the variation of stress triaxiality during the deformation process, which has been successfully applied to butterfly specimens under pure shear deformation [130] and sharp-notched specimens under tension [131]. In the current study, the FE modelling is used to determine variation of stress triaxiality during the mechanical testing. Average of the stress triaxiality value for the entire deformation process, as to be detailed later, is then used to represent the stress triaxiality for a given specimen geometry.

Although it is well recognized that stress triaxiality affects fracture strain, limited information is available on the stress triaxiality at the crack tip and its influence on critical strain and fracture toughness for the onset of crack growth. Among the work available in the literature, Mackenzie et al. [44] established the

[2] This chapter has been published in the following publication:
Yu, F., Jar, P.-Y.B., Hendry, M., 2017. Fracture behaviour at the sharp notch tip of high-strength rail steels - Influence of stress triaxiality. Engineering Fracture Mechanics 178, 184-200.

relationship between stress triaxiality and fracture strain for round-notched tensile specimens, based on which fracture toughness (K_{Ic}) for high-strength-low-alloy steels was estimated. Ritchie et al. [46], in view that crack tip opening displacement (CTOD) could be related to plastic fracture strain at the crack tip, developed a stress-modified critical fracture strain model to investigate the dependence of fracture toughness on test temperature and strain rate for two steels used to construct nuclear pressure vessels. In their study, plastic fracture strain at the crack tip was also determined based on an extrapolation of the fracture strains from notched specimens. Gillemot and his co-workers [67, 68] developed the concept of absorbed specific fracture energy (ASFE) by extrapolating both strain energy density (SED) and elongation of plastic zone from notched specimens to those at the crack tip to estimate fracture toughness of low and medium strength structural materials. However, it should be noted that all of the above studies are only suitable for prediction of fracture toughness for ductile materials that involve significant plastic deformation at the crack tip before the onset of crack growth.

For fracture initiation with small-scale yielding, Ritchie et al. [32] defined a parameter based on critical fracture stress at a location about two grain diameters ahead of the crack tip as a criterion to estimate fracture toughness. Although the critical fracture stress could be derived using Hill's slip-line field theory, study has shown that microstructural features such as carbide thickness and nucleation mechanism could affect the critical fracture stress [132]. Alternatively, the SED approach has been developed as a powerful tool for fracture toughness prediction. A special SED theory, first proposed by Sih and his co-workers [61, 64, 133], was used to estimate fracture toughness for linear elastic materials under a mixed mode loading based on the strain-energy-density factor, S. This theory employs the concept of total SED at the crack tip and suggests that both distortional and dilatational energy dissipation should be considered for crack initiation. Mode I fracture was deemed primarily due to dilatation and secondarily due to distortion [62, 65]. The total SED theory was later extended to prediction of fracture toughness under small and large scale yielding [66, 134]. A volume-based total

SED approach was developed by Lazzarin et al. [59, 69-71, 135-138] for assessment of static and fatigue strength when the mean value of the total SED over a control volume reaches a critical level. Although the volume-based SED approach was originally developed for failure assessment of engineering materials with brittle and quasi-brittle fracture [59], it is now extended to small and large scale yielding [72]. Its latest application is for creep fracture and nanoscaled singular stress field [139, 140]. Recently, the SED theory led to development of a new equivalent material concept (EMC) [141, 142], for assessment of ductile fracture in notched components. In spite of the wide range of applications, as described above, it should be pointed out that in the existing SED approaches; the total SED concept is only applicable to elastic deformation. For plastic deformation, because of the assumption of J_2 flow theory only the distortional SED, rather than the total SED, has been considered for the fracture assessment under both small and large scale yielding.

In this chapter, K_{Ic} for three high-strength rail steels was predicted based on the concept of total SED that considers contribution from both distortion and dilatation to fracture initiation of a sharp-notch tip under small-scale yielding. The equivalent plastic fracture strain for the pre-cracked SENB specimen was estimated through extrapolation to the stress triaxiality level which is equivalent to that for the sharp-notch tip, using test results from two types of notch-free specimens (to be named smooth and short-gauge specimens). Experimental testing and FE modelling were carried out to establish the fracture locus of stress triaxiality and plastic fracture strain for smooth and short-gauge specimens. The FE modelling of SENB specimen was also used to determine stress triaxiality and a characteristic distance ahead of the sharp notch tip of SENB specimen. The above information (including stress triaxiality, equivalent plastic fracture strain and the characteristic distance for the sharp notch tip) was then used with constitutive equation to calculate the critical strain energy density factor and the corresponding equivalent critical stress intensity factor (K_{Sc}) for the three high-strength rail steels at three temperatures (i.e., at 23, -10, and -40^{o}C). The

estimated K_{Sc} values were compared with those for K_{Ic}, to explore the feasibility of using mechanical properties of notch-free specimens to predict K_{Ic}.

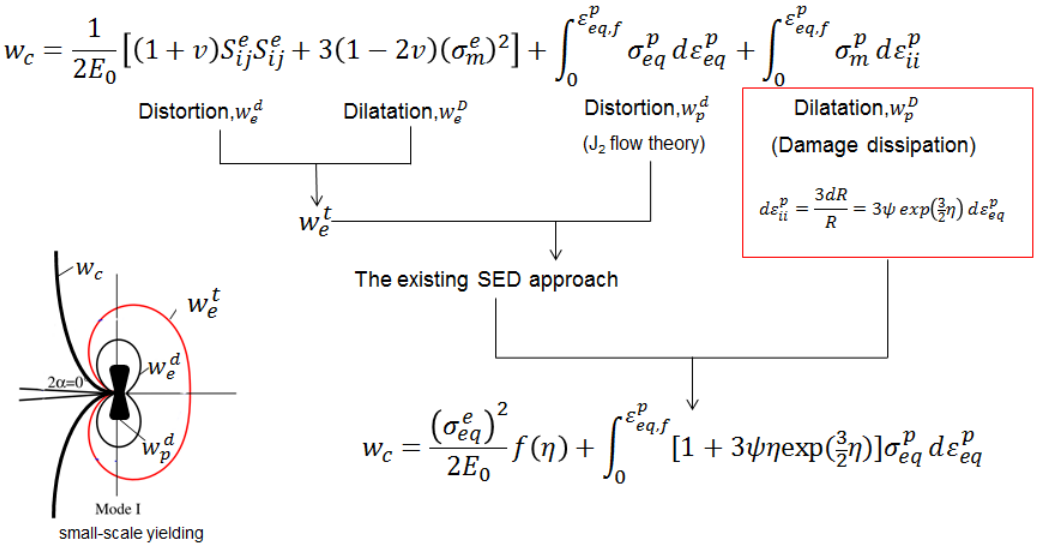

Figure 3.1 The overall approach of correlating tensile properties to K_{Ic} based on an extended SED model

3.2 Theoretical model

Figure 3.1 shows the overall approach for correlating the tensile properties to K_{Ic} based on the application of an extended strain energy density (SED) model. Due to the large stress triaxiality at the crack tip, the assumption of incompressibility in the von Mises criterion is no longer valid [60, 64, 71, 75]. Therefore, in addition to the existing SED approach which only considered elastic SED and distortional plastic SED (w_p^d) for the elastic-plastic deformation, the dilatational plastic SED (w_p^D), which represents damage energy dissipation, is also considered in the present study. The expression of void growth rate proposed by Rice and Tracey [126] is used to represent the change of volume plastic strain. Based on this, the amount of energy dissipation, including elastic, plastic and damage, can be modelled as a function of equivalent stress, stress triaxiality, and

equivalent plastic fracture strain. The above information can be used to calculate the magnitude of SED for the mode I fracture at the crack tip under small-scale yielding. Details of this approach are described as follows.

3.2.1 Critical strain energy density factor

The SED, w, as defined in the classical elastic-plastic theory, is expressed as

$$w = w_e + w_p = \int \sigma_{ij}\, d\varepsilon_{ij} \tag{3.1}$$

where w_e and w_p are the elastic and plastic parts of SED, and σ_{ij} and ε_{ij} the total stress and strain, respectively. Both the w_e and w_p can be expressed in terms of deviatoric and hydrostatic parts, where the deviotoric component is for the distortional energy and the hydrostatic part for the dilatational energy [60, 64, 71, 75]. That is,

$$w = \frac{1}{2E_0}\left[(1+v)S_{ij}^e S_{ij}^e + 3(1-2v)(\sigma_m^e)^2\right] + \int S_{ij}^p d\epsilon_{ij}^p + \int \sigma_m^p d\varepsilon_{ii}^p \tag{3.2}$$

where, E_0 and v are the Young's modulus and Poisson's ratio, respectively, S_{ij}^e and σ_m^e the deviatoric and hydrostattic stresses in the elastic region, respectively, S_{ij}^p, ϵ_{ij}^p, σ_m^p, and ε_{ii}^p the deviatoric stress, deviatoric strain, hydrostatic stress, and volume strain in the plastic region, respectively.

Based on the concept of von Mises equivalent stress and equivalent strain, the w can be expressed as

$$w = \frac{\left(\sigma_{eq}^e\right)^2}{2E} f(\eta) + \int \sigma_{eq}^p d\varepsilon_{eq}^p + \int \sigma_m^p d\varepsilon_{ii}^p \tag{3.3}$$

where, $\sigma_{eq}^{e} = (\frac{3}{2} S_{ij}^{e} S_{ij}^{e})^{0.5}$, $\sigma_{eq}^{p} = (\frac{3}{2} S_{ij}^{p} S_{ij}^{p})^{0.5}$, and $\varepsilon_{eq}^{p} = (\frac{2}{3} \epsilon_{ij}^{p} \epsilon_{ij}^{p})^{0.5}$ are the elastic equivalent deviatoric stress, plastic equivalent deviatoric stress, and plastic equivalent deviatoric strain, respectively, and $f(\eta)$ the triaxiality factor, as proposed by Lemaitre [127], is given in the expression below:

$$f(\eta) = \frac{2}{3}(1 + v) + 3(1 - 2v)(\eta)^2 \tag{3.4}$$

where η is the stress triaxiality defined as ratio of the hydrostatic stress to the von Mises stress.

For the classical plasticity theory that assumes incompressibility during the plastic deformation, i.e., $d\varepsilon_{ii}^{p} = 0$, the third term for *w* in Eq. (3.3) should always be zero, thus having no contribution to w_p. However, previous studies have shown that a ductile fracture process in metals involves both dislocation movement and cavity development [143, 144]. By taking into account the latter, the $d\varepsilon_{ii}^{p}$ can be related to the cavity growth rate, expressed as follows [75, 126],

$$d\varepsilon_{ii}^{p} = \frac{3dR}{R} = 3\psi \, exp\left(\tfrac{3}{2}\eta\right) d\varepsilon_{eq}^{p} \tag{3.5}$$

where R is the cavity radius, and dR/R the cavity growth rate. The factor ψ was originally assumed to be constant for materials that follow the von Mises criterion [126]. Later, the assumption was modified [145] to have a constant ψ value of 0.427 for η>1 and $\psi = 0.427\eta^{0.25}$ for 0.33< η<1. In the current study, this η-dependent ψ expression is adopted for calculating w.

Thus, by substituting Eq. (3.5) into Eq. (3.3), and after rearranging, Eq. (3.3) leads to,

$$w_c = \frac{\left(\sigma_{eq}^{e}\right)^2}{2E} f(\eta) + \int_0^{\varepsilon_{eq,f}^{p}} \left[1 + 3\psi \, \eta \, exp\left(\tfrac{3}{2}\eta\right)\right] \sigma_{eq}^{p} \mathrm{d}\varepsilon_{eq}^{p} \tag{3.6}$$

where, w_c is the critical strain energy density, which includes energy dissipation for both distortion and dilatation under elastic-plastic deformation until fracture occurs, and $\varepsilon_{eq,f}^{p}$ the equivalent plastic fracture strain for a given type of specimen.

According to the SED theory [60], in order to estimate crack growth resistance at the crack tip, the above w_c should be converted to the critical strain energy density factor at a characteristic distance ahead of the crack tip, as follows:

$$s_c = r_0 w_c \tag{3.7}$$

where, S_c is the critical strain energy density factor, and r_0 the characteristic distance along the crack growth path which is from the crack tip to the location where the maximum stress triaxiality occurs, as suggested in refs. [41, 42]. Consequently, the equivalent critical stress intensity factor, K_{Sc}, is estimated using the following expression [34]:

$$K_{Sc} = \sqrt{2Es_c} \tag{3.8}$$

In view of Eqs. (3.6), (3.7) and (3.8), in order to determine the K_{Sc} for the three rail steels at 23, -10, and -40°C, values of η, r_0, $\varepsilon_{eq,f}^{p}$, and σ_{eq}^{p} must be determined for the pre-cracked SENB specimen. To this end, the values of η and r_0 are determined using FE modelling of the pre-cracked SENB specimen, the constitutive equation, contanintg information of E, v, σ_{eq}^{e} and σ_{eq}^{p}, is calibrated from the smooth tensile specimen, and the $\varepsilon_{eq,f}^{p}$ of the pre-cracked SENB specimen is determined by extrapolation, as to be elaborated in the following section.

3.2.2 Equivalent plastic fracture strain

Since the equivalent plastic fracture strain ($\varepsilon_{eq,f}^{p}$) for the pre-cracked SENB specimen cannot be measured directly from the mechanical testing, its value is estimated through extrapolation of the measured fracture strain values for the smooth and short-gauge tensile specimens to the stress triaxiality level that corresponds to the crack tip.

Studies of stress state effect on material ductility [93, 146-148] have shown that the fracture strain value depends more significantly on the stress triaxiality than on either the strain rate or Lode angle parameter. Therefore, fracture strain is assumed here to be solely a function of the stress triaxiality.

The extrapolation of fracture strain to the stress triaxiality level at the crack tip is based on a locus of plastic fracture strain versus stress triaxiality which was originally proposed by Bonora [128], and modified in this study to consider the variation of stress triaxiality due to the neck formation. The original relationship between plastic fracture strain and stress triaxiality is

$$\varepsilon_{eq,f}^{p} = p_{th}\left(\frac{\varepsilon_{p}^{f}}{\varepsilon_{th}}\right)^{1/f(\eta)} \tag{3.9}$$

where ε_{p}^{f} is the plastic fracture strain measured from the smooth tensile specimen, ε_{th} and p_{th} the damage threshold strains for the uniaxial and triaxial stress states, respectively. In this study, damage is assumed to start from the yield point and the two threshold strains are both set to be 0.002 for all the cases studied using the three rail steels.

Note that in order to consider the loading history effect [130], η value in the above expressions is replaced by the average stress triaxiality (η_{av}), hereafter, as defined in Eq. (3.10) below.

$$\eta_{av} = \frac{1}{\varepsilon^p_{eq,max}} \int_0^{\varepsilon^p_{eq,max}} \eta(\varepsilon^p_{eq}) d\varepsilon^p_{\mathrm{eq}} \tag{3.10}$$

where $\eta(\varepsilon^p_{eq})$ and $\varepsilon^p_{eq,max}$ are the stress triaxiality as a function of ε^p_{eq} and the maximum value of ε^p_{eq}, respectively, both being determined from an element of a FE model which has the maximum η value when the simulation reaches the critical deformation level for fracture initiation in the testing. That is, η_{av} for the two types of tensile specimens is evaluated at the central element on the cross-section of their FEM models, and η_{av} for the pre-cracked SENB specimen determined at a characteristic distance ahead of the crack tip along the crack growth path of its FE model (simply referred to as 'η_{av} at the crack tip' in the rest of the text).

In addition to the use of η_{av} to represent the stress triaxiality, Eq. (3.9) has also been modified to accommodate the shape change in the smooth tensile specimen due to the neck formation. Therefore, the final expression used in the extrapolation procedure to determine the $\varepsilon^p_{eq,f}$ for the pre-cracked SENB specimen is

$$\varepsilon^p_{eq,f} = 0.002 \left(\frac{\varepsilon^f_p}{0.002} \right)^{f(\eta_0)/f(\eta_{av})} \tag{3.11}$$

where η_0 is the average stress triaxiality for the smooth tensile specimen, and η_{av} the average stress triaxiality for the smooth, short-gauged or pre-cracked SENB specimen. When η_{av} is equal to η_0, $\varepsilon^p_{eq,f}$ value represents ε^f_p for the smooth tensile specimen. Since ε^f_p is measured from the smooth tensile specimen and both η_0 and η_{av} from FE simulation, Eq. (3.11) does not contain any adjusting parameter.

3.3 Experimental investigation

3.3.1 Materials and test specimens

A test program was conducted at 23, -10, and -40^{o}C, which included the use of smooth, short-gauge, and pre-cracked SENB specimens, as shown in Figure 3.2. Three high-strength rail steels, JAPAN NSC FHH (JP), EVRAZ RMSM FHH (EV), and CZECH TZ IH (CZ), supplied by the Canadian National Railway Company (CN), were used in the test program. All three types of mechanical testing were conducted on specimens prepared from the railhead region. An Instron hydraulic universal testing machine was used, with temperature control using an Instron environmental chamber. For tests at low temperatures, additional thermocouples were welded on each specimen to ensure that temperature of the specimens had reached the targeted value before the tests were conducted.

The smooth and short-gauge specimens were used to establish the fracture loci of stress triaxiality and plastic fracture strain, from which the results were then applied to Eq. (3.11) for predicting the equivalent plastic fracture strain for the pre-cracked SENB specimens. Effect of temperature on fracture toughness for the three rail steels was characterized directly using experimental data from the SENB specimens. The K_{Ic} values were also used to evaluate validity of K_{Sc} defined in Eq. (3.8) for estimating fracture toughness of the three rail steels.

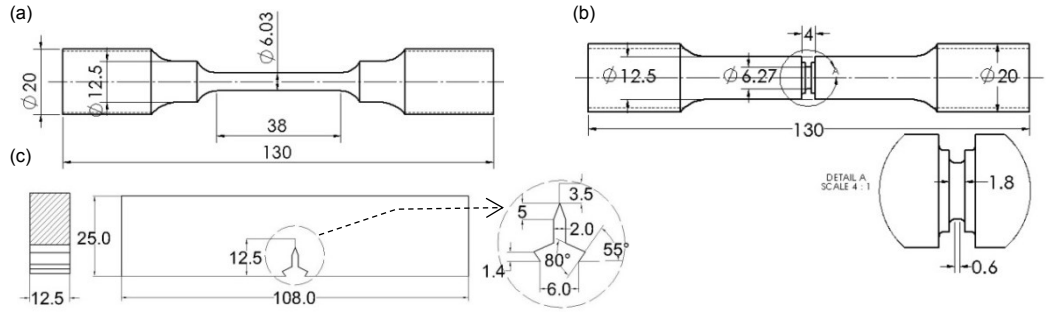

Figure 3.2 Geometry and dimensions of (a) smooth specimen, (b) short-gauge specimen, and (c) SENB specimen

3.3.2 Smooth specimens

Tests on smooth specimens were carried out according to the procedure specified in ASTM E8/E8M [17], to establish a reference on the material ductility and tensile strength for all three rail steels. At each temperature, three specimens were tested at a crosshead speed of 8.5×10^{-3} mm/s, equivalent to an initial strain rate of 2.36×10^{-4} /s. Each smooth specimen had two extensometers placed in the gauge section, to be able to measure simultaneously elongation and diameter changes. Based on the assumption of uniform stress-strain distribution along the minimum cross section, the plastic fracture strain ε_p^f was calculated using the equation below [103]:

$$\varepsilon_p^f = ln\left(A_0/A_f\right) \tag{3.12}$$

where A_0 is the original cross-sectional area in the reduced gauge section and A_f the corresponding area measured at the minimum cross section after fracture.

As shown in Figure 3.3, all three rail steels show excellent ductility at all three temperatures, with some neck development before fracture is initiated. Figure 3.3 also suggests that JP rail steel possesses the largest ductility and the highest tensile strength among the three, while CZ the lowest.

The fundamental mechanical properties for the three rail steels at temperature 23, -10, and -40^{o}C are summarized in Table 3.1 which suggests that with the decrease in test temperature from 23 to -40^{o}C, the three rail steels show a consistent increase in strength by approximately 10%. However, the corresponding reduction in ductility varies slightly among the three rail steels. That is, by decreasing the temperature from 23 to -40^{o}C the plastic fracture strain is reduced from 0.5 to 0.4 for JP rail steel, from 0.30 to 0.24 for EV, and from

0.183 to 0.165 for CZ. For details of the test procedures, please refer to the information in Chapter 2.

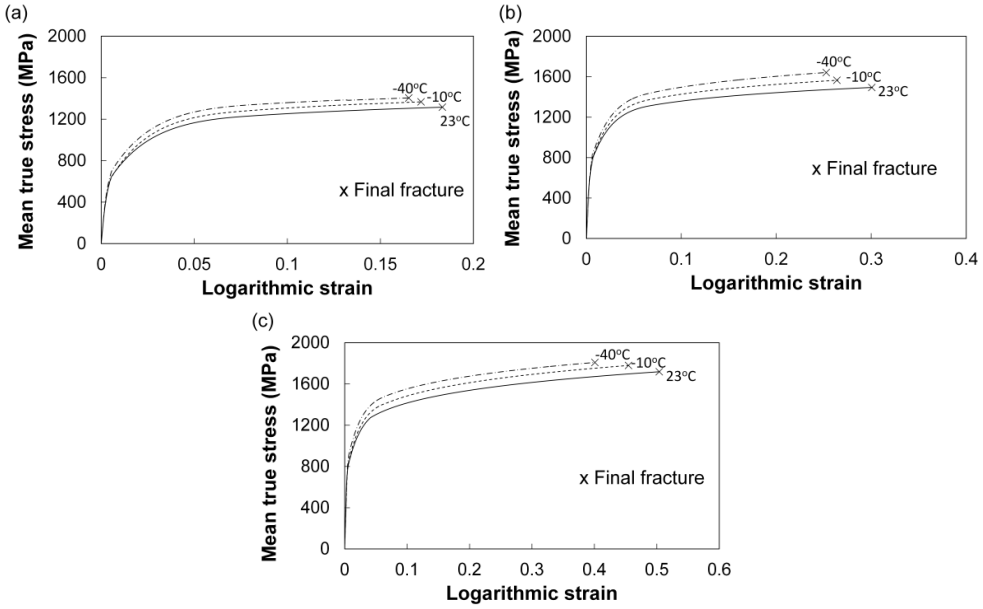

Figure 3.3 Temperature effect on the mean true stress-logarithmic strain curves of smooth specimens for (a) CZ, (b) EV, and (c) JP high-strength rail steels

Table 3.1 Mechanical properties for the three rail steels at 23, -10 and -40°C.

		Smooth tensile					Short-gauge tensile	
Rails	**°C**	E_o(GPa)	σ_y(MPa)	σ_{uts} (MPa)	σ_f(MPa)	ε_p^f (%)	σ_f (MPa)	ε_p^f (%)
	23	193	632	1130	1307	18.3	1587	3.4
CZ	-10	193	638	1185	1367	17.2	1543	2.4
	-40	193	679	1230	1405	16.5	1544	2.0
	23	195	714	1207	1422	30.1	1750	4.0
EV	-10	195	782	1291	1524	26.7	1725	3.1
	-40	195	823	1345	1585	24.4	1754	2.2
	23	200	820	1280	1634	50.4	1862	4.7
JP	-10	200	837	1338	1692	45.4	1862	3.9
	-40	200	901	1400	1774	40.1	1809	2.8

3.3.3 Short-gauge specimens

Tests on short-gauge specimens were also carried out to investigate the change in fracture strain with the increase of stress triaxiality from that for the smooth specimens. Again, at least three tests were conducted for each of the rail steels at each temperature and at the initial strain rate same as that used for the smooth specimens. Since length of the gauge section for this type of specimens is 1.8 mm, strain is characterized only by a diametric extensometer, placed in the middle of the gauge section. The measured diametric change is used to calculate the logarithmic strain to represent the deformation generated during the test. Diameter of the post-test specimens was used to determine the equivalent plastic fracture strain using Eq. (3.12).

Figure 3.4 presents typical true stress-logarithmic strain curves for the short-gauge specimens at temperature 23, -10, and -40^{o}C, with values for fracture stress and strain also summarized in Table 3.1. Figure 3.4 shows clearly that with the decrease of temperature from 23 to -40^{o}C, the plastic fracture strain is reduced from 0.047 to 0.028 for JP rail steel, from 0.04 to 0.022 for EV, and from 0.034 to 0.020 for CZ. The fracture stress, on the other hand, is not much affected by the temperature changes.

Results in Table 3.1 indicate that for all three rail steels, reduction of the specimen gauge length from 38 mm to less than 2 mm has caused a significant reduction in the fracture strain, but only a slight increase in the fracture stress, though their ranking among the three rail steels remains unchanged. For instance, at 23^{o}C, the equivalent fracture strains for the short-gauge specimens of CZ, EV, and JP rail steels are about 10 times smaller than that for their smooth specimens, but the corresponding increase in fracture stress is less than 20%. This, as to be discussed later, is an indication of the stress triaxiality having a stronger influence on fracture strain than on fracture stress.

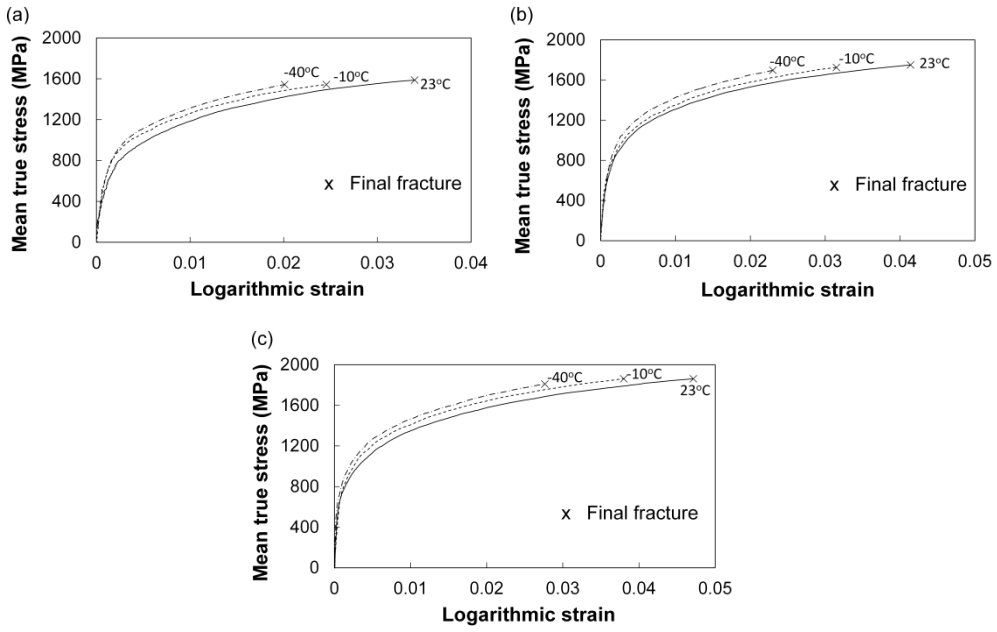

Figure 3.4 Temperature effect on the mean true stress-logarithmic strain curves of short-gauge specimens for (a) CZ, (b) EV, and (c) JP high-strength rail steels

3.3.4 Single-edge-notched bend (SENB) specimens

The SENB tests were performed for two purposes. One is to investigate the effect of temperature on fracture toughness (K_{Ic}) and the other to identify the crack mouth opening displacement (CMOD) for the first apparent pop-in which is assumed to be the moment when the fracture initiation occurs in the SENB specimens. In this study, pre-crack length of all the SENB specimens were controlled to reach approximately 3.5 mm using fatigue testing by keeping the maximum stress intensity factor (K_{max}) and the minimum stress intensity factor (K_{min}) to be 14 and 5 MPa.m$^{0.5}$, respectively. The SENB tests were then conducted at the crosshead speed of 2×10^{-3} mm/s. CMOD was measured using a clip-on extensometer, mounted to the mouth of the notch before each test. The K_{Ic} values were determined from eight specimens for CZ rail steel and twelve for each of EV and JP rail steels at each temperature. Use of the additional four specimens for EV

and JP rail steels is because these two rail steels have very similar K_{Ic} values, thus requiring additional specimens to distinguish their difference if any. Figure 3.5 summarizes the typical curves of mode I stress intensity factor (K_I) versus CMOD (δ). Following ASTM E399 [18], the K_I value was calculated using the equations below.

$$K_I = \frac{P\bar{S}}{\bar{B}W^{3/2}} \cdot f\left(\frac{a_0}{W}\right) \tag{3.13}$$

$$f\left(\frac{a_0}{W}\right) = 3\sqrt{\frac{a_0}{W}} \cdot \frac{1.99 - \left(\frac{a_0}{W}\right)\left(1-\frac{a_0}{W}\right)\left[2.15 - 3.93\frac{a_0}{W} + 2.7\left(\frac{a_0}{W}\right)^2\right]}{2\left(1+2\frac{a_0}{W}\right)\left(1-\frac{a_0}{W}\right)^{\frac{3}{2}}} \tag{3.14}$$

where P is the load, a_0 the average initial pre-crack length, measured along the crack front after the specimen was fractured, and $\bar{B}$, W, and $\bar{S}$ specimen thickness, height, and span length, respectively. Dimensions of the SENB specimens used in this study are given in Figure 3.2(c).

After ensuring that both a_0 and B had satisfied the criteria for small scale yielding, values for the critical stress intensity factor, K_{Ic}, were determined using the procedures described in ASTM E399, that is, using a secant line with the slope of 95% of the tangent line to identify the intersection point with the experimental P-δ curve. In most cases, fracture initiation was deemed to occur at the first pop-in. But when a negligible pop-in occurred, such as the one circled in Figure 3.5(c) for -40°C, the K_{Ic} value was determined at the next pop-in, following the recommendation given in the ASTM standard.

Figure 3.5 suggests that all of the three rail steels show the decrease in K_{Ic} with the decrease of temperature, but as to be discussed later, difference in K_{Ic} among the three rail steels varies with the test temperature. That is, at 23 and -10°C, K_{Ic} values for JP and EV are clearly higher than CZ, but at -40°C difference of K_{Ic} among the three rail steels is significantly reduced.

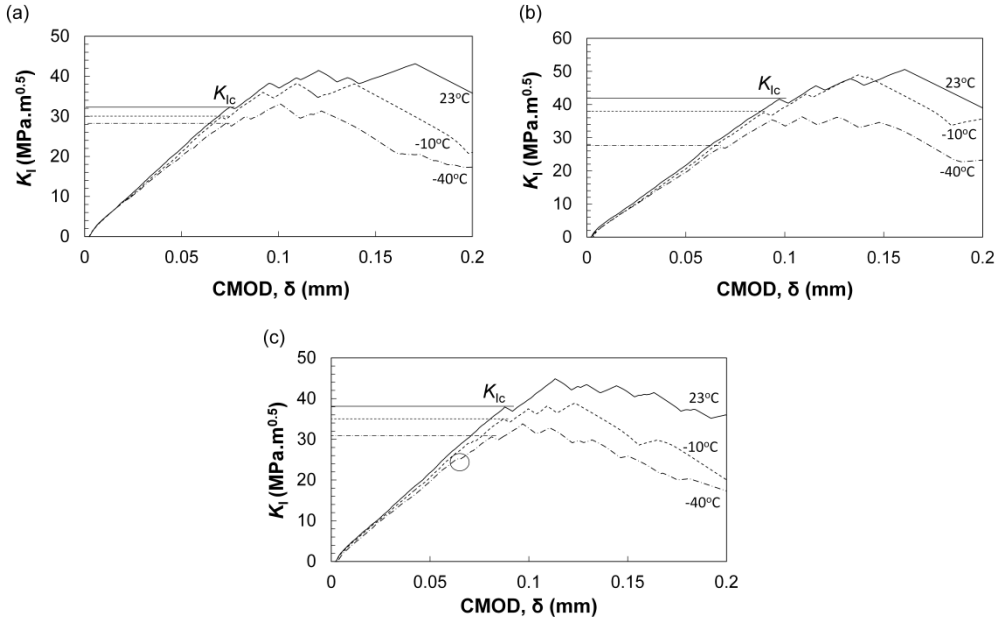

Figure 3.5 Temperature effect on stress intensity factor versus CMOD (K_I - δ) curves of SENB specimens: (a) CZ, (b) EV, and (c) JP rail steels

3.4 Numerical simulations

$\varepsilon_{eq,f}^{p}$ value for the pre-cracked SENB specimen is estimated using Eq. (3.11), based on plastic fracture strain (ε_p^f), average stress triaxiality (η_0) for the smooth specimen and average stress triaxiality at the sharp notch tip of the SENB specimen (η_{av}). Value for η_{av} was determined using Eq. (3.10) based on the stress triaxiality evolution established from the FE modelling. In this section, details for the FE models for smooth, short-gauge and SENB specimens are described. The FE modelling was performed using ABAQUS standard 6.13, with the consideration of change in the gauge section profile during the deformation. It should be pointed out that for a given type of specimen the increase of strain hardening in the constitutive equation can reduce the rate of stress triaxiality evolution.

3.4.1 FE modelling of smooth specimens

Numerical simulation was carried out to mimic the deformation behaviour of smooth specimens at temperature 23, -10, and -40^{o}C, in order to establish the constitutive equations for the three rail steels at each temperature. Each of the constitutive equations was then used to determine the evolution of the stress triaxiality until the critical point for fracture initiation was reached, which occurred at the minimum cross section of the gauge section.

An axisymmetric FE model of 6,392 quadrilateral 8-node elements and 20,173 nodes was used for the simulation, with dimensions following those given in Figure 3.2(a). Boundary conditions were set to be the same as those for the testing, i.e., with one end fixed and the other end moving at a specified displacement rate. Figure 3.6 shows an example of the typical necking behaviour generated by the FE model, overlaid on a fractured smooth specimen of JP rail steel which was tested at 23^{o}C. As the smooth specimens were prepared without any tapering, location for the neck formation and fracture occurred asymmetrically. Thus, in the FE modelling, necking was generated by introducing a slightly tapered gauge section with the diameter of the minimum cross section reduced by 0.1%, at the location where fracture was initiated in the experimental testing.

The same phenomenological model that consists of four functions of equivalent stress versus strain in Eq. (2.4), was used to establish the constitutive equations for the three rail steels, based on test data from smooth specimens. Values for the constants in the four functions of Eq. (2.4) were tuned in an iterative process so that the FE model could regenerate the load-elongation and diameter reduction curves from the experimental testing, of which an example is illustrated in Figure 3.6 for the JP rail steel at all three temperatures.

Details of this iterative process to establish those expressions were given in Chapter 2. The resulted constants for the three rail steels are listed in Table 3.2. Note that values for constants E, v, a, c, d, and γ are intentionally kept constant

for each of the three rail steels, while the other constants adjusted based on variation of the experimental data with temperature. It is shown that as temperature drops from 23 to -40^{o}C the decrease of parameter b is related to the increase of initial strain-rate before the yielding point, while the increase of parameters e, α, $\bar{\beta}$, M, and n is related to the increase of the work-hardening behaviour.

In view of the good agreement between the experimental testing and the FE modelling, as shown in Figure 3.7, stress variation with deformation given by the FE models is used to determine the evolution of stress triaxiality of smooth specimens for the three rail steels, at all temperatures considered in this study. As an example, Figure 3.8 shows the distribution of stress triaxiality and equivalent plastic strain for the smooth specimen of JP rail steel at the onset of fracture initiation, as a function of distance from the centre in the radial direction on the minimum cross section of the FE model. The figure shows that maximum values for both the stress triaxiality and the equivalent plastic strain occur at the centre of the cross section.

Figure 3.9 depicts evolution of stress triaxiality at the centre of smooth specimens, for the three rail steels at temperature 23, -10, and -40^{o}C. As mentioned earlier, values for the average stress triaxiality were determined using Eq. (3.10). Since JP rail steel showed the most significant necking behaviour, this rail steel has also been expected to have the largest average stress triaxiality value. The CZ rail steel, on the other hand, has the smallest value. Figure 3.9 suggests that evolution of the stress triaxiality is not much affected by the test temperature, but value for the average stress triaxiality decreases with the decrease of the test temperature.

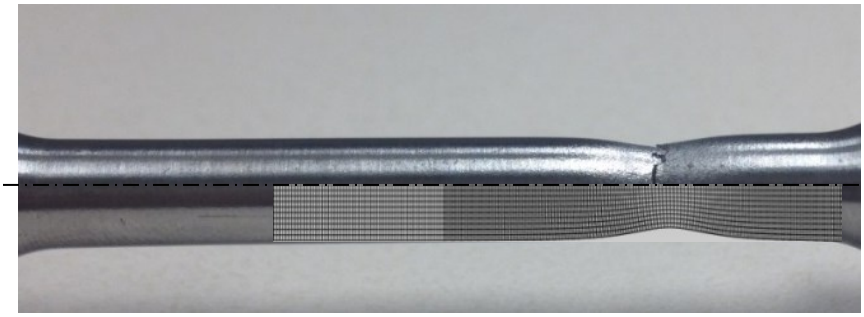

Figure 3.6 Deformed shape and FE discretization of the smooth specimen of JP rail steel at 23^{o}C

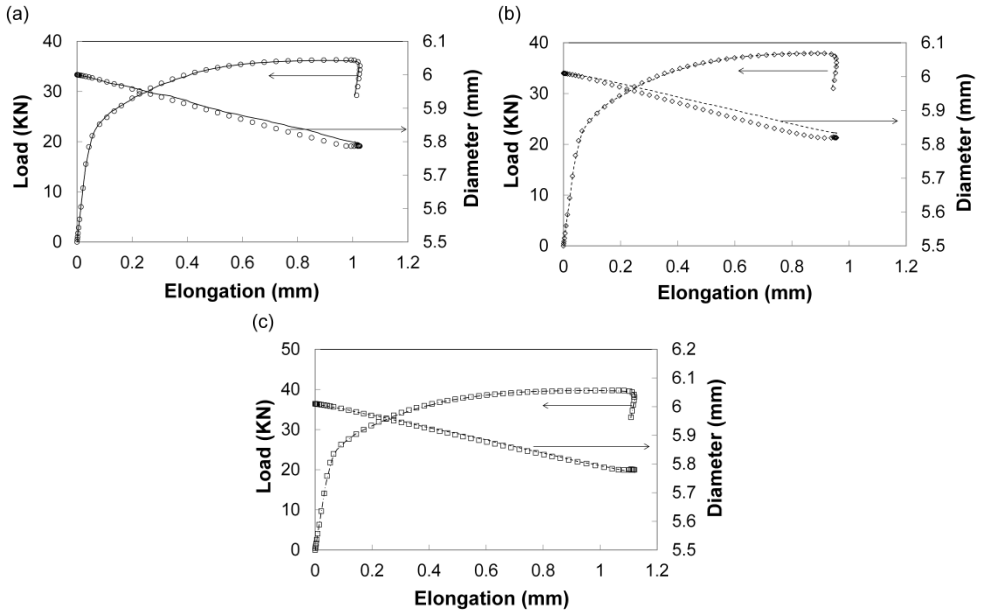

Figure 3.7 Comparison of load-elongation and cross-section reduction between experimental testing and FE modelling of JP rail steel at temperature of (a) 23^{o}C, (b) -10^{o}C, and (c) -40^{o}C

Table 3.2 Parameters in Eq. (2.4) for three rail steels at temperature 23, -10, and -40°C

Parameters \ Rails	CZ			EV			JP		
	23 °C	-10 °C	-40 °C	23 °C	-10 °C	-40 °C	23 °C	-10 °C	-40 °C
E (GPa)	193	193	193	195	195	195	200	200	200
ν	0.3	0.3	0.3	0.3	0.3	0.3	0.3	0.3	0.3
a (MPa)	30.0	30.0	30.0	29.6	29.6	29.6	30	30	30
b	0.0101	0.0101	0.0099	0.0096	0.0094	0.0092	0.0092	0.0088	0.0085
c	-2	-2	-2	-2	-2	-2	-2	-2	-2
d	-26	-26	-26	-26	-26	-26	-24	-24	-24
e (MPa)	889	895	937	994	1037	1082	1080	1100	1150
α (MPa)	452	478	504	564	581	611	645	651	700
$\bar{\beta}$ (MPa)	1240	1305	1320	1350	1415	1470	1400	1450	1530
γ	45.0	45.0	45.0	45.0	45.0	45.0	45.0	45.0	45.0
M (MPa)	1502	1583	1608	1640	1752	1838	1710	1802	1910
n	0.082	0.083	0.084	0.085	0.090	0.093	0.086	0.090	0.092

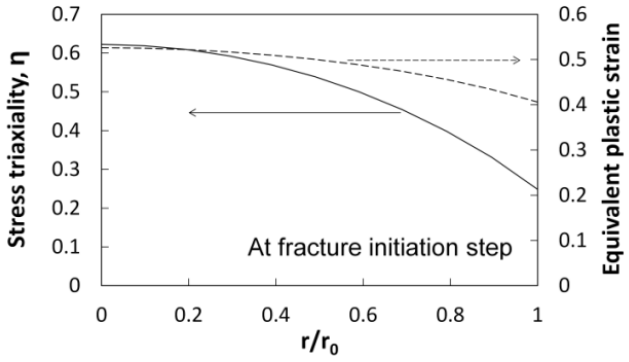

Figure 3.8 Distribution of stress triaxiality and equivalent plastic strain along the minimum cross section at the onset of fracture initiation in the smooth specimen for JP rail steel at 23°C

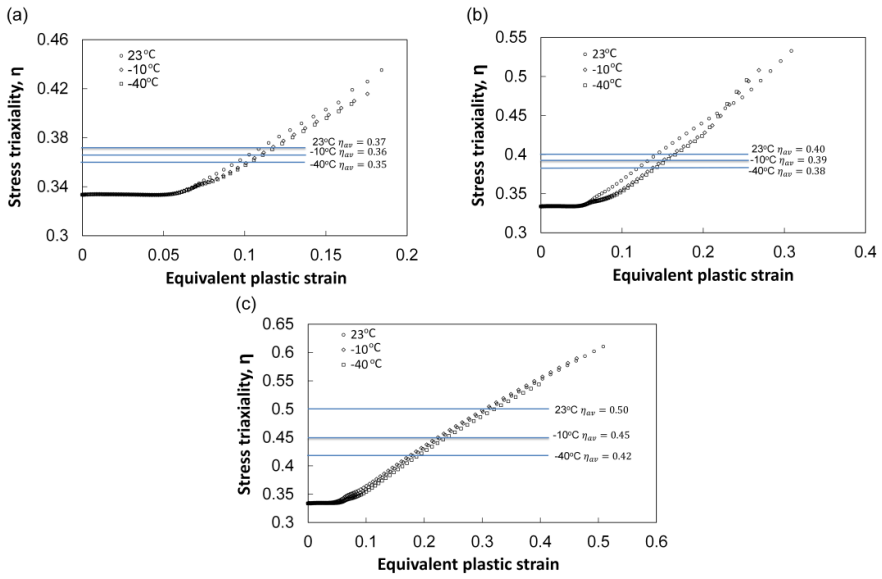

Figure 3.9 Evolution of stress triaxiality with the increase of the equivalent plastic strain of smooth specimens, and its average value at temperature 23, -10, and -40°C for (a) CZ, (b) EV, and (c) JP rail steels

3.4.2 Application of constitutive equations

3.4.2.1 FE modelling of short-gauge specimens

The constitutive equations established for smooth specimens were applied to a quarter, axisymmetric FE model of short-gauge specimens to determine the average stress triaxiality. The model consists of 4,930 quadrilateral 8-node elements and 15,119 nodes, with dimensions same as those given in Figure 3.2(b). One end of the model that represents the central cross section in the gauge section has a symmetric displacement boundary condition, while the other end is subjected to the displacement-controlled boundary condition. Figure 3.10 shows the mesh pattern of the FE model, overlaid on a fractured specimen of JP rail steel, tested at 23°C. As shown in the figure, necking does not occur in the specimen, possibly because of its short gauge length that has introduced some constraints for the localized cross sectional contraction. As a result, ductility at

fracture for the short-gauge specimens is much lower than that for the smooth specimens.

Figure 3.11 presents both the experimentally determined curves (represented by lines) of mean axial true stress versus logarithmic area strain for the short-gauge specimens, and the corresponding curves generated from the FE models (represented by symbols), for all three rail steels at all temperatures considered in the study. In view of good agreement between simulation and experimental results, we believe that the high-strength rail steels can be categorized as pressure-insensitive metals of which the constitutive equations are independent of stress triaxiality, similar to that for the 1045 steel [146].

Distribution of the stress triaxiality and equivalent plastic strain along a radial direction on the central cross section of the gauge section, at the onset of fracture, is presented in Figure 3.12 for JP rail steel at 23^{o}C. The figure suggests that the maximum stress triaxiality occurs at the centre of cross section (r/r_0=0), but the maximum equivalent plastic strain occurs along a circular band that is close to the circumference of the cross section. According to the study on the fracture initiation in the notched tensile specimens [75, 149], fracture of the short-gauge specimens is expected to start from the centre of the cross section.

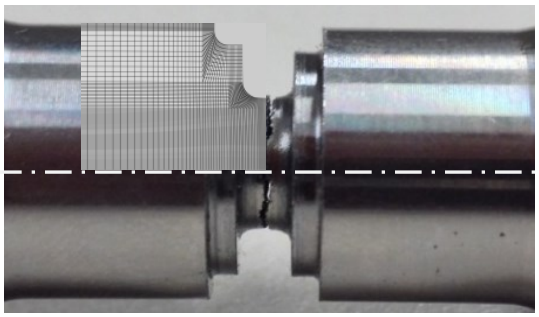

Figure 3.10 Mesh pattern of the FE model for the short-gauge specimens, overlaid on a fractured JP specimen tested at 23^{o}C

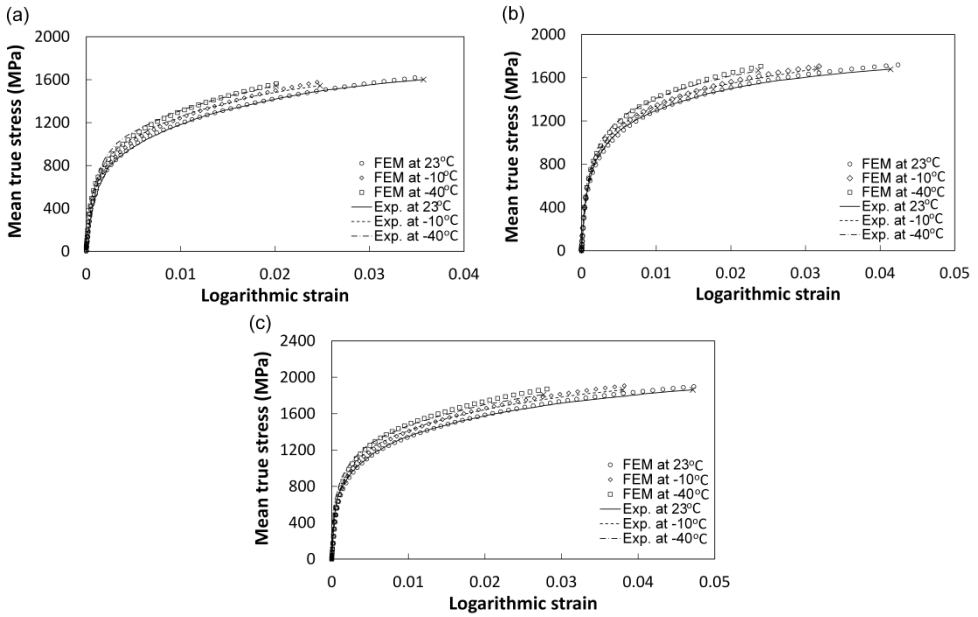

Figure 3.11 Comparison of experimental and simulation results of short-gauge specimens for (a) CZ, (b) EV, and (c) JP rail steels

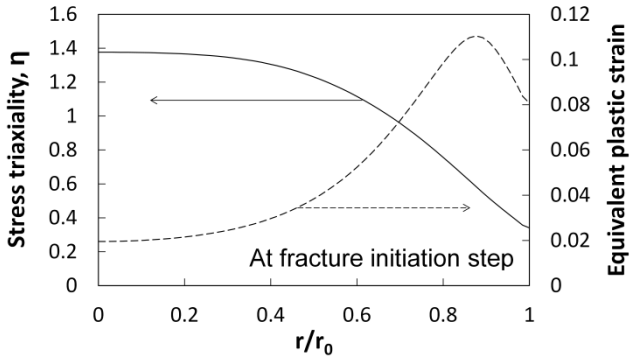

Figure 3.12 Distribution of stress triaxiality and equivalent plastic strain on the minimum cross section of short-gauge specimen at the onset of fracture initiation for JP rail steel at 23°C

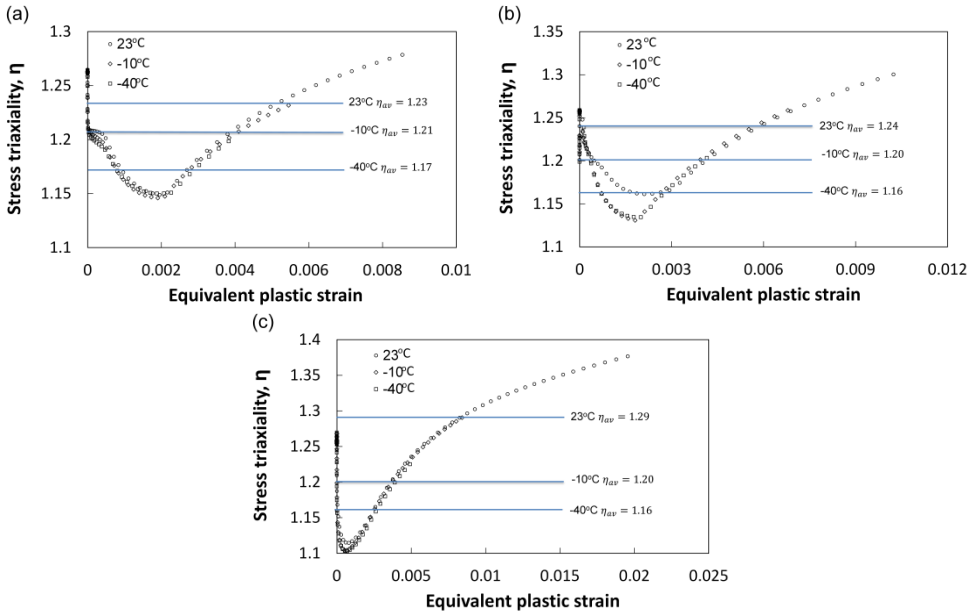

Figure 3.13 Stress triaxiality evolution with the increase of the equivalent plastic strain of short-gauge specimens, and its average value at temperature 23, -10, and -40°C for (a) CZ, (b) EV, and (c) JP rail steels

The average stress triaxiality for the short-gauge specimens was determined using Eq. (3.10), based on the evolution of stress triaxiality of the central element on the minimum cross section. Figure 3.13 summarizes evolution of the stress triaxiality for the three rail steels, at all temperatures considered in the study. Similar to that shown in Figure 3.9, Figure 3.13 also suggests that for each of the three rail steels, evolution of the stress triaxiality does not show much dependence on the test temperature. But, as indicated by three horizontal lines in each plot of Figure 3.13, the average stress triaxiality decreases with the decrease of the test temperature, which is believed mainly due to the decrease of fracture strain.

3.4.2.2 FE modelling of SENB specimens

The constitutive equations established for the smooth specimens were also applied to the FE modelling of SENB specimens, to determine the average stress

triaxiality at the sharp notch tip for the three rail steels at 23, -10, and -40^{o}C. Figure 3.14 presents the FE model overlaid on a SENB specimen of JP rail steel. The model is 2-dimensional (2D), with dimensions following those specified in Figure 3.2(c), and contains 29,155 quadrilateral 8-node elements and 88,200 nodes. The sharp notch tip has a quarter-circular profile, with an initial radius of 0.1 μm, which is determined based on the strip yield model [150] and falls within the range of practical fatigue crack size [151]. In order to capture the large stress and strain gradients around the sharp notch tip, the quarter circular arc along the sharp notch tip was divided into 18 sections. Such division is repeated in the radial direction around the sharp notch tip, to generate one hundred layers of fan elements in the radial direction.

It should be noted that because the crack tip region is divided into a very high density of standard solid elements, it would be too expensive to use a 3-dimensional (3D) FE modelling to simulate the deformation behaviour. Rather, the more conservative 2D modelling with a plane-strain condition was used. Because of the use of 2D FE simulation, the change of the constraint condition on the fracture toughness variation, especially in the thickness direction, was not considered. A 3D FE analysis of such an effect has been investigated [152, 153]. In view that dimensions of the SENB specimens used in our study follow those specified in the standard test for the plane-strain condition, we believe that such an effect should not be significant for our specimens.

Boundary conditions for the FE model are set to be the same as those introduced in the experiment. The central loading pin was constrained to allow only the displacement-controlled, downward movement, while the support pin was fixed in space. A finite-sliding, surface-to-surface contact algorithm was introduced to simulate the interaction between the specimen surface and the pin. The contact friction was based on the classical Coulomb's law.

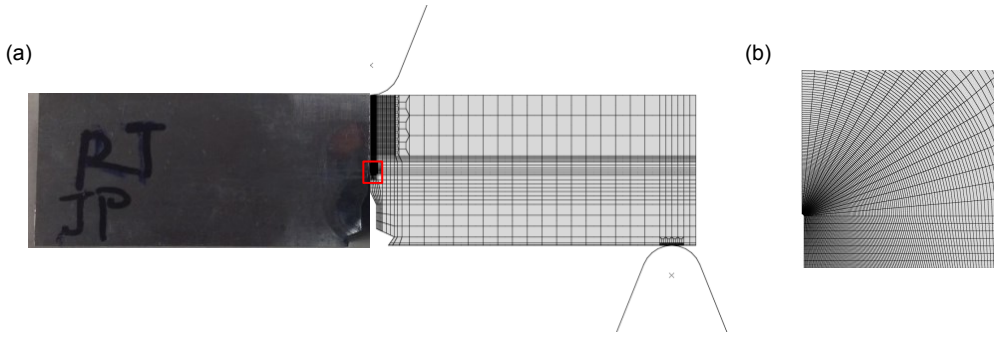

Figure 3.14 The SENB test of JP rail steel at 23°C: (a) the global mesh pattern and (b) the mesh pattern at the sharp notch tip, within the region enclosed in (a)

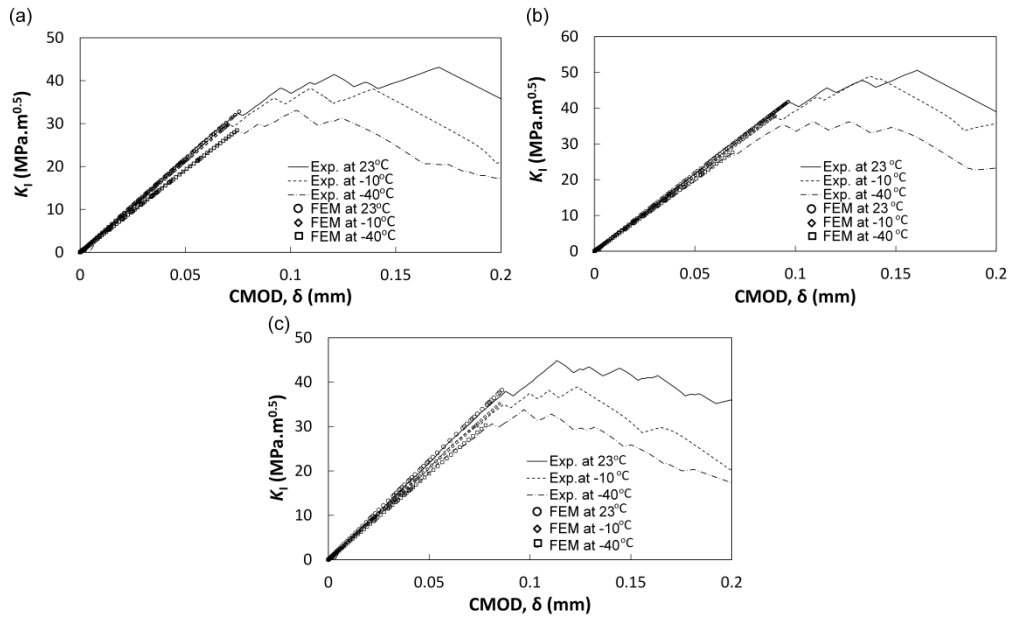

Figure 3.15 Plots of K_I versus CMOD from the FE modelling, superimposed on the curves in Figure 3.4 from the SENB tests, at temperature 23, -10, and -40°C for (a) CZ, (b) EV, and (c) JP high-strength rail steels

The FE model for SENB specimen is also based on the J_2 plasticity theory. As shown in Figure 3.15, the FE model was calibrated by regenerating the linear portion of the experimental data before the first obvious pop-in occurred. Friction coefficient between the pins and the specimen surface was adjusted so that the

FEM-generated curve fits the experimental data. It was found that for all three rail steels, the friction coefficient value should be 0.35, 0.2, and 0.1 for temperature 23, -10, and -40^{o}C, respectively. Reduction of the friction coefficient with the decrease of temperature was probably due to the presence of a thin layer of ice in the contact region at low temperatures.

Figure 3.16 illustrates the simulation results in the region ahead of the sharp notch tip for JP rail steels at 23^{o}C. In Figure 3.16(a), variations of stress triaxiality and equivalent plastic strain at the critical loading level (the first pop-in) have been plotted as functions of distance from the sharp notch tip (X) in the crack growth direction. Note that abscissa of Figure 3.16(a) is X normalized by the critical value of crack tip opening displacement (CTOD) at the onset of crack growth. The figure suggests that the equivalent plastic strain shows singularity at the sharp notch tip, and its value decreases very rapidly to almost zero at a distance about 5 times of the critical CTOD. On the other hand, the stress triaxiality increases from zero at the sharp notch tip to about 3.0 at a distance of approximately twice of the critical CTOD. Such variation of stress and strain ahead of the crack tip is similar to those reported before [38, 154]. In order to further ensure of the accuracy of the current FE model for simulating the stress and strain distribution in front of the sharp notch tip, linear portion of the experimental data was also generated by a classical FE model of SENB specimen for elastic-plastic materials, with 1/r singularity for stress distribution at the crack tip [155]. Figure 3.16(b) compares distributions of stress triaxiality and von Mises stress in front of the crack tip from the classical model (presented by open squares) with the results from the model of Figure 3.14 (solid lines). The comparison suggests that results from the two models agree well with each other. Therefore, the FE model in Figure 3.14 that uses a very dense mesh of standard solid elements has captured the high-gradient stress-strain distribution in front of the crack tip.

In addition to distribution of stress triaxiality ahead of the sharp notch tip, the FE model in Figure 3.14 was also used to determine the characteristic distance

ahead of the sharp notch tip. As suggested in most recent studies [41, 42], the characteristic distance is the distance from the sharp notch tip to an element along the crack growth path which has the maximum stress triaxiality at the onset of fracture, as illustrated in Figure 3.17 which is for the JP rail steel.

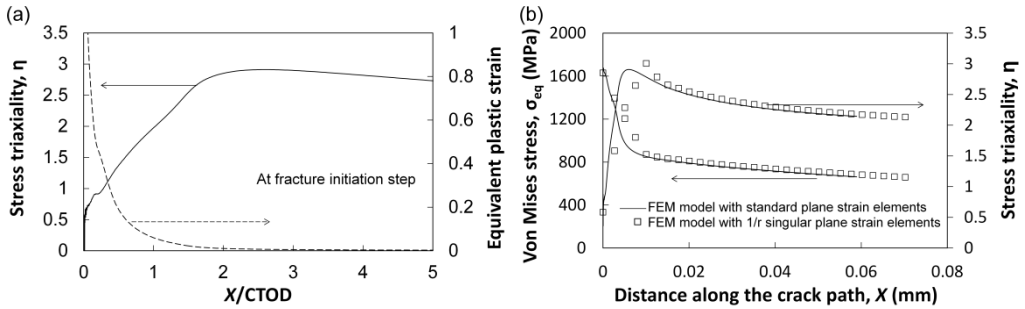

Figure 3.16 FE simulation results ahead of the sharp notch tip of SENB specimen for JP rail: (a) distributions of stress triaxiality and equivalent plastic strain along the crack path, and (b) comparison of FE models with standard and 1/r singularity, plane-strain elements

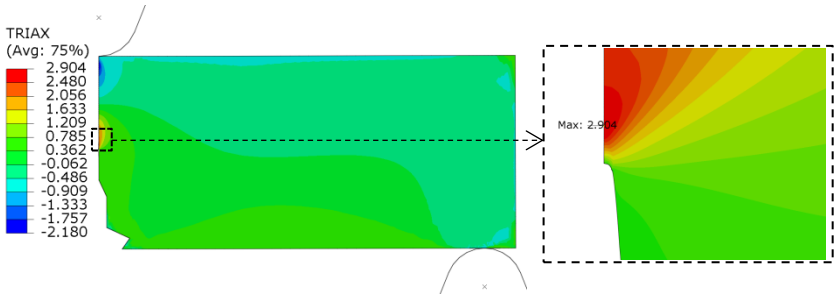

Figure 3.17 Stress triaxiality distribution ahead of the sharp notch tip of SENB specimen at the onset of fracture, for JP rail steel at 23°C

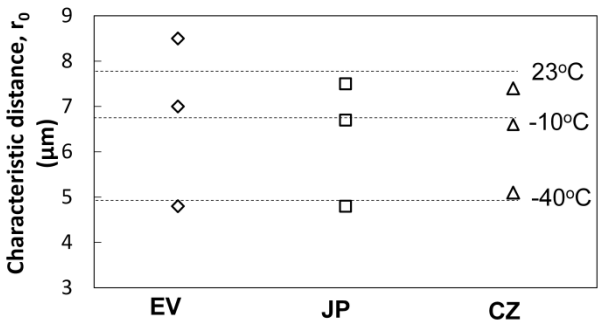

Figure 3.18 Determination of the characteristic distances with the maximum stress triaxiality for three rail steels at 23, -10, and -40°C

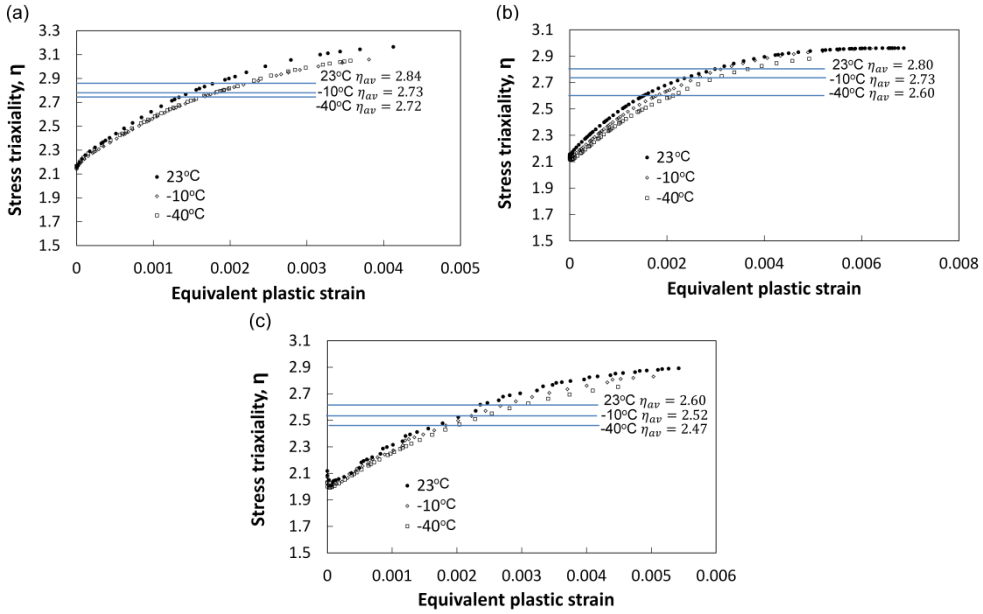

Figure 3.19 Stress triaxiality evolution with the increase of the equivalent plastic strain of SENB specimens, and its average value at temperature 23, -10, and -40°C for (a) CZ, (b) EV, and (c) JP rail steel

Figure 3.18 summaries values for the characteristic distance for all three rail steels at 23, -10, and -40°C, showing that the characteristic distance has relatively

constant values among the three rail steels at each temperature. The figure also shows that the characteristic distance decreases with the decrease of temperature.

Figure 3.19 presents evolution of stress triaxiality for the element that is located at the characteristic distance ahead of the sharp notch tip, as a function of equivalent plastic strain till fracture is initiated, and its corresponding average stress triaxiality level. Each of the three plots in Figure 3.19 summarizes results for a given rail steel at all three temperatures of 23, -10, and -40^{o}C, showing that the average stress triaxiality decreases with the decrease of temperature. Figure 3.19 suggested that at a given temperature, ranking of the three rail steels for their average stress triaxiality at the characteristic distance ahead of the sharp notch tip is opposite to that shown in Figure 3.9 for smooth specimen. The opposite ranking is believed to be caused by the influence of fracture strain on the calculated value for the average stress triaxiality. In Figure 3.9, the very different fracture strains among the three rail steels has resulted in higher average stress triaxiality for the rail with a larger fracture strain. In Figure 3.19, because of the similar fracture strains among the three rail steels, difference of the average stress triaxiality is believed to be mainly caused by the different rate of increase of the stress triaxiality with the increase of the equivalent plastic strain.

Results from the above FE simulations suggest that the average stress triaxiality is affected not only by the difference in specimen geometry, but also by the difference in mechanical properties such as fracture strain and constitutive equation, though the former is believed to play a primary role and the latter secondary. This speculation is supported by the previous works [92, 156] in which materials with greater work hardening generate smaller stress triaxiality. Therefore, evolution of stress triaxiality in a given type of rail steel specimen can be affected by the change in either steel type or test temperature both of which change mechanical properties that govern the evolution of stress triaxiality with deformation.

3.5 Results

3.5.1 Equivalent plastic fracture strain of pre-cracked SENB specimen

The equivalent plastic fracture strain ($\varepsilon_{eq,f}^{p}$) for the pre-cracked SENB specimens was estimated using Eq. (3.11) based on the relationship between $\varepsilon_{eq,f}^{p}$ and the average stress triaxiality for the smooth and short-gauge specimens. Figure 3.20 summarizes curves of $\varepsilon_{eq,f}^{p}$ generated from Eq. (3.11) for all three rail steels at all temperatures considered in this study, compared with the data obtained from the experimental testing on the two notch-free specimens (i.e., smooth and short-gauge specimens). The figure shows good agreement between the curves and the test data. By extrapolating the curves in Figure 3.20 to the η_{av} values at the sharp notch tip, as shown in Figure 3.19, the corresponding $\varepsilon_{eq,f}^{p}$ values of SENB specimen for the three rail steels, at temperature 23, -10, and -40^{o}C, are estimated and listed in Table 3.3. It is shown that all of the $\varepsilon_{eq,f}^{p}$ values of the pre-cracked SENB specimens are in the vicinity of the yield strain and show little sensitivity to the temperature change. Furthermore, those values are significantly smaller than the fracture strain for smooth specimens, due to the increase of the stress triaxiality. Although ranking of the three rail steels based on the $\varepsilon_{eq,f}^{p}$ value for SENB specimen is similar to that for the notched-free specimens, the trend of variation of $\varepsilon_{eq,f}^{p}$ with temperature between the SENB specimens and the notched-free specimens is different for each of the three rail steels. This is further discussed as follows.

It has long been known and clearly shown in Table 3.1 that material ductility (represented by fracture strain here) is expected to decrease with the decrease of temperature. However, such a trend is not obvious for the pre-cracked SENB specimens of the three rail steels, as shown in Table 3.3. For CZ and EV rail steels, values for $\varepsilon_{eq,f}^{p}$ in Table 3.3 actually show a very small increase with the

decrease of temperature from 23 to -40°C. This is believed to be caused by the counter effect of the drop of η_{av} value at the sharp notch tip with the decrease of temperature. As shown in Figure 3.19, η_{av} value decreases with the decrease of temperature. And based on the trend line shown in Figure 3.20, decrease of the η_{av} value should cause increase of $\varepsilon_{eq,f}^{p}$, which may offset the decrease of $\varepsilon_{eq,f}^{p}$ due to the decrease of temperature. Therefore, the trend of change for $\varepsilon_{eq,f}^{p}$ with temperature change, as shown in Table 3.3, is probably caused by the combined effect of temperature and stress triaxiality. That is, fracture strain of SENB specimen decreases with the decrease of temperature, but increases with the decrease of η_{av}. As a result of the combined effect of temperature and stress triaxiality, $\varepsilon_{eq,f}^{p}$ values in Table 3.3 show very little change with the decrease of the test temperature.

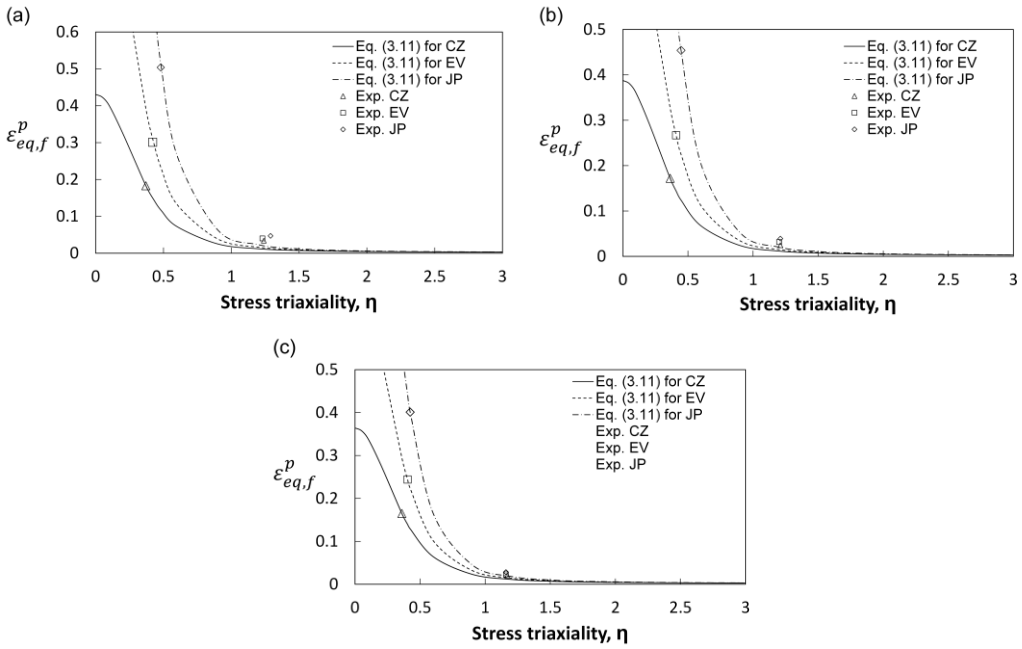

Figure 3.20 Dependence of equivalent plastic fracture strain on stress triaxiality of three rail steels at (a) 23, (b) -10, and (c) -40°C

Table 3.3 Fracture strain of pre-cracked SENB specimen

Rail steels / °C	CZ	EV	JP
23	0.00309	0.00343	0.00406
-10	0.00317	0.00341	0.00406
-40	0.00316	0.00353	0.00403

3.5.2 K_{Ic} from SENB tests

Figure 3.21 summarizes the measured K_{Ic} values for the three rail steels at temperature 23, -10 and -40°C. Each of the rail steels shows decrease in the average K_{Ic} value by approximately 20% with the decrease of temperature from 23 to -40°C. Also, at all three temperatures the EV and JP rail steels seem to have similar K_{Ic} values, while both of them clearly have higher K_{Ic} values than that for the CZ rail steel. The difference of K_{Ic} among the three rail steels, however, is reduced at -40°C, suggesting that all three rail steels are almost equally susceptible to break in service at -40°C.

In order to examine any difference in the K_{Ic} values between the EV and JP rail steels at 23, -10, and -40°C, Welch's t-test is applied in this study [157]. As the experimental data of the two rail steels are with unequal sample sizes and unequal variances, the following equations are adopted:

$$d.f. = \frac{\left(s_1^2/N_1 + s_2^2/N_2\right)^2}{\left(s_1^2/N_1\right)^2/(N_1-1) + \left(s_2^2/N_2\right)^2/(N_2-1)} \tag{3.15}$$

$$t = \frac{\overline{X_1} - \overline{X_2}}{\sqrt{s_1^2/N_1 + s_2^2/N_2}} \tag{3.16}$$

where $d.f.$ is the degree of freedom according to sample sizes; t is the statistic to test whether the means of two samples are different; $\overline{X_1}$, s_1^2, and N_1 are mean,

population variance, and sample size, respectively, for the 1st sample; while $\overline{X_2}$, s_2^2, and N_2 for the 2nd sample.

Figure 3.22(a) plots the two-tails t-distribution with the *d.f.* of 23 which is calculated using Eq. (3.15) according to the sample sizes of EV and JP rail steels [158]. Based on the number of *d.f.*, the *t* critical value with the confidence level of 95% is read as 2.07 from the *t* table [159]. This states the criterion that when the calculated *t* values are bigger than 2.07 or smaller than -2.07, the null hypothesis for the K_{Ic} values between the EV and JP rail steels can be rejected.

Figure 3.22(b) shows the t-test results for the K_{Ic} values between the EV and JP rail steels at each temperature; as well, the mean and standard deviation of K_{Ic} values for the three rail steels are plotted at the three temperatures. Both the *t* and *P* (probability) values are shown in Figure 3.22(b), the former are calculated using Eq. (3.16), and the latter the ratio of the 'area', integrated under the t-distribution curve from the point greater than the calculated t-value, to the whole area under the t-distribution curve. Based on the t-test results, difference of K_{Ic} values between the EV and JP rail steels is identified at the three temperatures. Here we found that at 23 and -10°C the difference in K_{Ic} value exists between the EV and JP rail steels as the *t* values are bigger than 2.07. While at -40°C their difference in K_{Ic} value is negligible because the *t* value is smaller than 2.07.

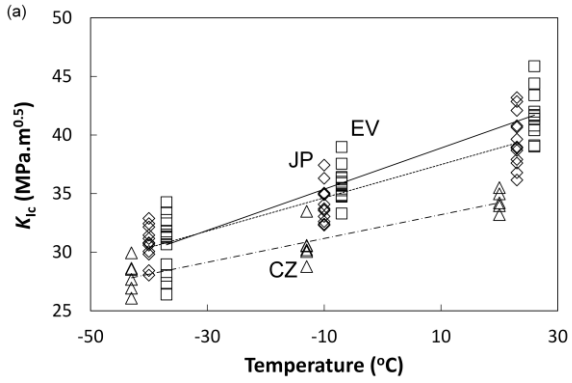

Figure 3.21 Experimental data of K_{Ic} values among the three high-strength rail steels at temperature 23, -10, and -40°C

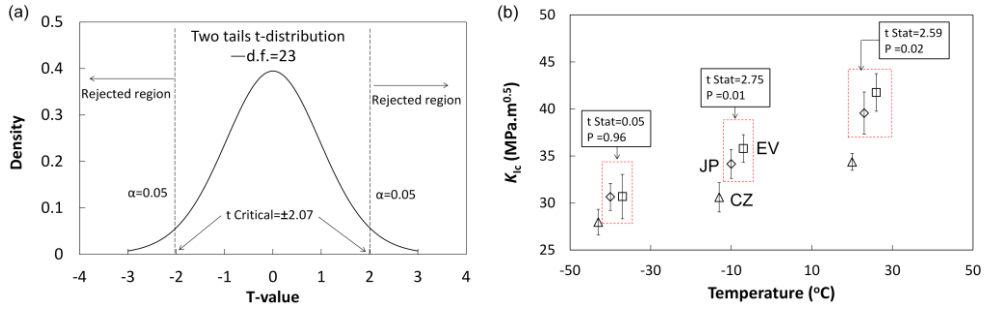

Figure 3.22 Welch's t-test analysis: (a) t-distribution with 95% confidential level at degree of freedom 23, and (b) t-test results between the EV and JP rail steels at 23, -10, and -40°C

3.5.3 K_{Ic} prediction

As mentioned earlier, the main objective for the current study is to explore the feasibility of using results from smooth and short-gauge specimens to predict the trend of change for K_{Ic} values among the three rail steels at 23, -10, and -40°C. In this section, information from the constitutive equation, the characteristic distance, r_o, the average stress triaxiality at the characteristic distance ahead of the sharp notch tip, and the equivalent plastic fracture strain of SENB specimen are used to calculate K_{Sc} based on the critical strain energy density factor (s_c) using Eq. (3.7). The predicted K_{Sc} values are also compared with the experimentally measured K_{Ic} values.

As suggested by Eq. (3.6), both distortional and dilatational SEDs for elastic-plastic deformation are included in the critical strain energy density, w_c. As shown in Figure 3.22, with the determined information of average stress triaxiality, constitutive equation and equivalent plastic fracture strain, w_c values are determined for smooth, short-gauge, and SENB specimens of the three rail steels, at each of the three temperatures considered in this study. Figures 3.22(a) and 3.22(b) show that JP rail steel has the largest w_c values at all three temperatures and CZ the smallest for both types of notch-free specimens. And the

difference of w_c values among the three rail steels becomes smaller for the short-gauge specimens. These trends are consistent with the results for the two notch-free specimens which are shown in Figures 3.3 and 3.4. However, Figure 3.22(c) suggests that at the sharp notch tip of SENB specimen difference between JP and EV is reversed, though w_c for CZ remains to be the lowest at all three temperatures. Therefore, the trend of change for w_c from the tensile tests does not reflect that at the sharp notch tip.

As shown in Figure 3.23, the calculated K_{Sc} using Eq. (3.8) shows a linear relationship with K_{Ic} for all three rail steels at temperature 23, -10, and -40^{o}C. The good agreement between K_{Ic} and K_{Sc} is probably because the total SED concept are implemented in the present study where both distortional and dilatational SEDs have been taken into account to calculate s_c. For ductile fracture, such as that for a notch-free specimen in tension, variation of distortional SED is expected to have a strong influence on the s_c value. While at the sharp notch tip of SENB specimen, on the other hand, because of the very limited plastic deformation that is involved in the fracture process, as suggested in Table 3.3, the contribution of distortional SED to s_c should be small, which according to our calculation for the three rail steels, is about two orders of magnitude smaller than the dilatational counterpart. Therefore, the s_c value for a sharp notch tip is expected to be dominated by the dilatational SED. Correctness of using total SED, instead of distortional SED only, has also been examined by Radaj et al. [71] for failure assessment of mode I brittle fracture where the dilatation SED should also be dominant. Thus, it is suggested that assessment on mode I fracture resistance in small-scale yielding should consider both distortional and dilatational SEDs.

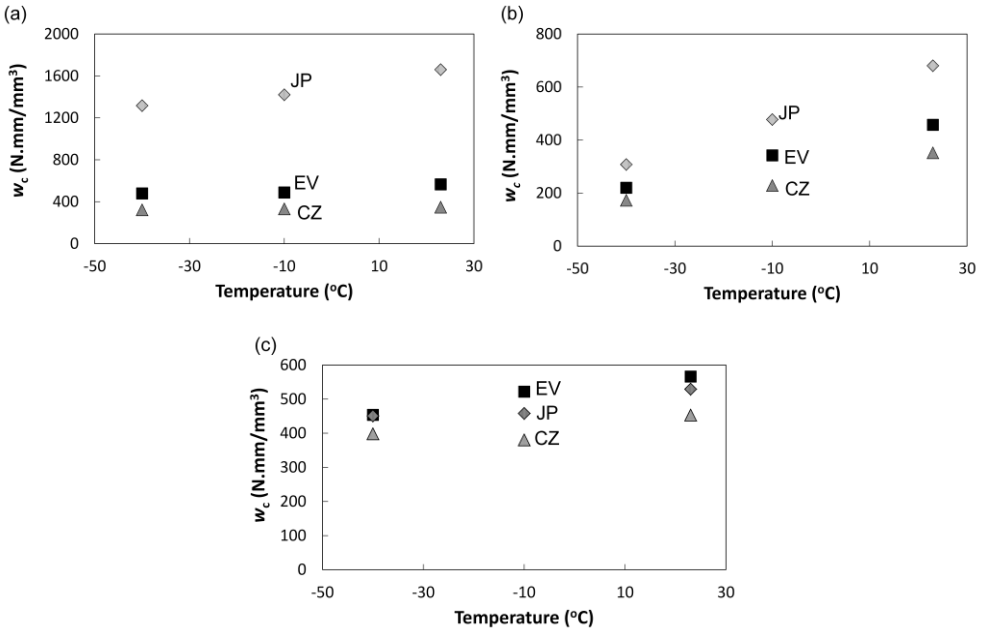

Figure 3.23 Differences in the critical SED values of (a) smooth specimen, (b) short-gauge specimen, and (c) sharp notch tip of SENB specimen, among the three rail steels at temperature 23, -10, and -40°C

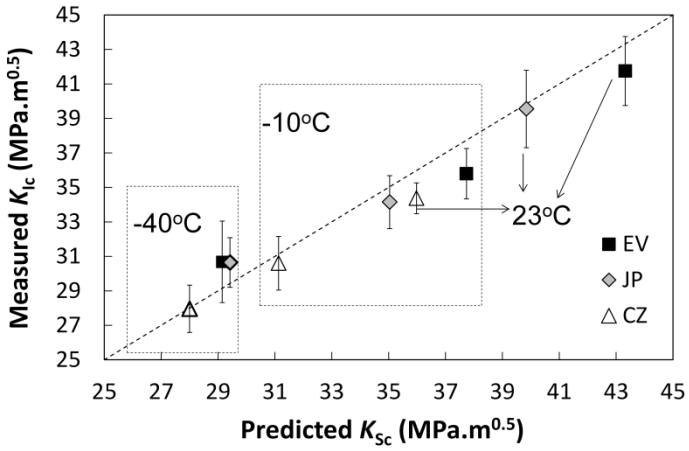

Figure 3.24 Comparison of the predicted K_{Sc} values with the measured K_{Ic} for the three rail steels at temperature 23, -10, and -40°C

3.6 Conclusions

The study investigated mechanical properties of three types of high-strength rail steels at 23, -10, and -40°C using notched (SENB) and notch-free (i.e., smooth and short-gauge) specimens. By establishing the fracture loci of stress triaxiality versus fracture strain from notch-free specimens, a modified Bonora's model is used to predict the equivalent plastic fracture strains ($\varepsilon_{eq,f}^{p}$) of pre-cracked SENB specimen. The study shows that the $\varepsilon_{eq,f}^{p}$ values can be reduced significantly, to the vicinity of yield strain, by the increase of stress triaxiality to the level at a sharp notch tip. The study also shows that the value for $\varepsilon_{eq,f}^{p}$ at the sharp notch tip of SENB specimen does not change much with the change of temperature, and suggests that this is because the $\varepsilon_{eq,f}^{p}$ value also depends on the stress triaxiality.

By combining FE simulation and experimental testing, average stress triaxiality (η_{av}) has been determined for all three types of specimens used in the study. The study found that ranking of η_{av} among the three rail steels is opposite between SENB and notch-free specimens. This phenomenon has been successfully explained using the influence of fracture strain and constitutive equation on the η_{av} value. That is, for the smooth specimens, difference of the η_{av} values is dominated by the large difference of the fracture strains among the three rail steels (Figure 3.9). For the SENB specimens, however, the fracture strains for the three rail steels at all three temperatures have similar values. Therefore, the change of η_{av} at the sharp notch tip of SENB specimen is mainly due to the variation of the constitutive equations (Figure 3.19). Furthermore, the study found that since both temperature and η_{av} affect fracture strain, the fracture strain at the sharp notch tip shows little change with the change of temperature, which is different from the dependence of fracture strain for the notch-free specimens on the temperature change.

The study also shows the possibility of predicting the trend of K_{Ic} for all three rail steels at 23, -10, and -40°C using K_{Sc} that is based on the critical strain energy

density factor (s_c), a product of w_c and r_o. The study found that this is possible because w_c considers both distortional and dilatational SEDs for fracture initiation under small-scale yielding. For the notch-free specimens, w_c value is dominated by the distortional SED while at the sharp-notch tip of SENB specimen, its value is dominated by the dilatational SED. It is therefore concluded that both distortion and dilatation are indispensable parts that need to be considered for the energy consumption in the elastic-plastic deformation process that leads to fracture.

Chapter 4 A new constitutive model for high-strength rail steels by considering stress-triaxiality-dependent plasticity and damage[3]

4.1 Introduction

J_2 flow theory for plastic deformation [103, 160, 161] has a profound influence on engineering practice, in which two fundamental tenets, i.e., independence of yielding on stress triaxiality and incompressibility of plastic deformation, have been extensively examined by generations of material scientists and engineers. Some studies obtained results that challenge these two tenets. For example, Spitzig and Richmond [162] and Spitzig et al. [163, 164] conducted extensive tensile and compressive tests with the superimposed hydrostatic pressure, on quenched and tempered AISI 4310 and 4330, maraging, and HY-80 steels, and found that the experimentally characterized constitutive equations for those metals are actually pressure-dependent, which is consistent with the prediction based on the Drucker-Prager yield function [165]. It should be pointed out that work from the same group also showed that for 1045 steel, the constitutive equation is insensitive to the increase of the superimposed hydrostatic pressure, though the ductility is [166]. Wilson [167] reexamined the classical metal plasticity theory for aluminum alloy 2024-T351, and found that prediction based on the Drucker-Prager yield criterion agrees better with the experimentally established constitutive equation than the J_2 flow theory does. Since Lode angle parameter (or the third deviatoric stress invariant) is also known to play an important role on the applied stress for the yielding [168-175], a new metal plasticity model has been developed by Bai and Wierzbicki [176] for engineering

[3] Part of this chapter has been published in the following publications:
1. Yu, F., Jar, B. and Hendry, M., Stress triaxiality effect on damage evolution of high-strength steels. 24th International Congress of Theoretical and Applied Mechanics (ICTAM2016), Montreal, Quebec, 21-26 August.
2. Yu, F., Jar, B. and Hendry, M., A constitutive model for metals with the consideration of stress-triaxiality-dependent plasticity and damage. (under review at International Journal of Solids and Structures)

materials, to consider the influence of both stress triaxiality and Lode angle parameter on the deformation behaviour.

In spite of the above development, the constitutive equation based on the J_2 flow theory is still very popular, considered to be well suited for many engineering materials. For example, Bai et al. [146] found no dependence of the constitutive equation for 1045 steel on the stress triaxiality, and Mirone and Corallo [177] reported a negligible influence of stress triaxiality on the stress level for yielding, though the stress triaxiality poses a noticeable influence on the fracture strain. Such difference in the material characteristics has been generally attributed to the inconsistency of the influence of stress triaxiality on the constitutive equations [176], denoted as the conventional constitutive equations in this chapter. However, it is now widely accepted that materials in the above studies have deformation and fracture behaviour governed by two coupled attributors of plastic deformation and damage evolution. If each of these two attributors could be analyzed for their dependency on the stress triaxiality, the inconsistence about the sensitivity of the conventional constitutive equations on the stress triaxiality might be resolved.

The development of damage theories has enabled the incorporation of various damage accumulation concepts in the deformation process. This has successfully captured the transition from plastic deformation to ductile fracture, but yet to be able to reconcile the inconsistency about the different levels of sensitivity of the conventional constitutive equation on the stress triaxiality. The existing works that consider the damage criteria in the constitutive equations can be summarized into two groups, one based on micromechanics models and the other phenomenological models. The former was first proposed by McClintock [125] and Rice and Tracey [126], and further developed to become the well-known Gurson-Tvergaard-Needleman (GTN) model [143, 144]. The latter, on the other hand, was based on continuum damage mechanics (CDM) in the framework of thermodynamics [90, 178]. Both groups adopted the concept that development of the ductile damage depends on stress triaxiality and Lode angle parameter [96,

179-187]. However, even with the consideration of effects of both stress triaxiality and Lode angle parameter on the damage development [96, 185], the relationship between stress and strain is still based on the original concept that uses the classical J_2 plasticity theory. That is, stress triaxiality and Lode angle parameter are deemed to affect the development of ductile damage only, not the damage-free stress-strain relationship. Recently, Chaboche et al. [188] proposed the use of two state variables to include damage evolution and plastic compressibility in the conventional constitutive equation for the ductile deformation. Brünig et al. [189, 190] who interpreted the conventional constitutive equation as the result of the combined effect of damage development and plastic deformation also proposed to reexamine the independence of flow stress on the stress triaxiality, but in their works the ductile damage was imbedded in expressions that use three stress invariants as the variables, not explicitly in terms of the actual damage parameter. Therefore, to our knowledge, no conventional constitutive equation has been interpreted explicitly using the separate expressions for the influence of stress triaxiality on the damage evolution and on the damage-free stress response to deformation. The damage-free stress response to deformation is referred to as the damage-free constitutive equation in the rest of the text.

This study uses experimental testing under monotonic and cyclic loading, with the assistance of numerical simulation, to establish the conventional constitutive equation and damage evolution for a high-strength rail steel. Two types of notch-free specimens, named smooth and short-gauge specimens, are used to generate different stress triaxiality levels. The results depict the insensitivity of the conventional constitutive equation to the change of stress triaxiality. The change of stress triaxiality, on the other hand, shows a strong influence on the damage evolution. A constitutive model is then postulated for the dependence of damage evolution and damage-free constitutive equation on the stress triaxiality, in search for explanations for the inconsistent influence of stress triaxiality on the conventional constitutive equation among metallic materials. Note that since

geometry for specimens used in the study was axisymmetric, the Lode angle parameter remained constant during the deformation [176], thus not considered here.

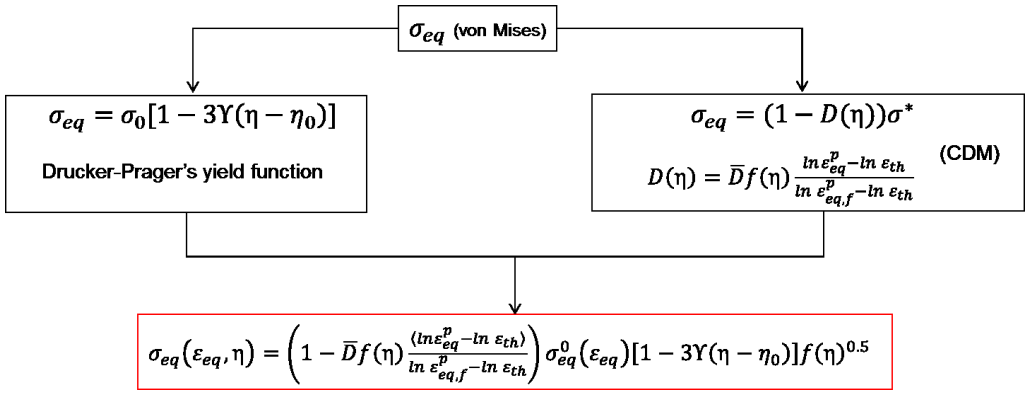

Figure 4.1 The overall approach of constructing a new constitutive model for rail steels to explain the independence of the conventional constitutive equation from the stress triaxiality

4.2 New constitutive model

This study is based on the concept that two factors, i.e., damage evolution and plastic deformation, affect the change of mechanical properties for metals. Figure 4.1 shows the development of a new constitutive model to explain why the conventional constitutive equation of rail steels is insensitive to stress triaxiality.On one hand, the experimentally calibrated conventional equivalent stress-strain curve (denoted as the conventional constitutive equation) is following the von Mises stress criterion, however, the conventional constitutive equation of some other materials are reported to follow the Drucker-Prager's yield function. On the other hand, based on CDM, the conventional constitutive equation can be interpreted as a combination of damage parameter and damage-free constitutive equation, where the former has been found as a function of stress triaxiality during deformation and the latter is still assumed to follow the von Mises criterion. In this study, the damage-free constitutive equation is proposed to follow the Drucker-Prager's yield function. In addition, a triaxiality factor is

added in the new constitutive model. Development of the postulated constitutive equation is detailed as follows.

Damage evolution is based on CDM, using damage parameter D to characterize the damage state. Here, D is assumed to be isotropic and related to the surface density of microdefects [191], that is,

$$D = \frac{S_D}{S_0} \tag{4.1}$$

where S_D is the total area of microcracks and cavities generated during the deformation and S_0 the overall cross sectional area of the loaded region. D can also be expressed in terms of the change of elastic modulus, as shown below, based on the concept of effective stress and with the hypothesis of strain equivalence [127].

$$D = 1 - \frac{E}{E_0} \tag{4.2}$$

where E is the effective elastic modulus which deceases as the total area covered by the microdefects increases, and E_0 the Young's modulus of the virgin material.

Due to the presence of microdefects, the equivalent stress decreases and can be expressed using the following expression [127, 191]:

$$\sigma_{eq} = (1 - D)\sigma^* \tag{4.3}$$

where σ_{eq} is the equivalent stress used in the conventional constitutive equation for a continuum medium, and σ^* the corresponding stress used in the damage-free constitutive equation for a continuum medium without the presence of damage. In general, σ_{eq} should depend on equivalent strain (ε_{eq}), stress triaxiality (η), Lode angle parameter (ξ) and D [176, 185, 189]. In the conventional constitutive

equation, σ_{eq} is often expressed solely in terms of ε_{eq}, showing little dependence on the other variables, including η [146, 177], which is the foundation for the classical metal plasticity.

4.2.1 Damage-free constitutive equation and its dependence on stress triaxiality

In the previous studies [96, 127, 143, 144, 187], damage-free stress, σ^*, which represents the mechanical response of materials without the presence of damage, is often assumed to follow J_2 flow theory or von Mises criterion. In the current work, σ^* is treated as a function of ε_{eq} and η, as shown below, with ξ value being constant because of the axial symmetry of the specimen geometry in this study:

$$\sigma^*\left(\varepsilon_{eq}, \eta\right) = \sigma_{eq}^0(\varepsilon_{eq})\, g(\eta) \tag{4.4}$$

where $\sigma_{eq}^0(\varepsilon_{eq})$ is the damage-free stress response to the equivalent strain (ε_{eq}) for a smooth specimen, and $g(\eta)$ a function of stress triaxiality which consists of both Drucker-Prager yield condition [165] and Lemaitre's triaxiality factor, $f(\eta)^{0.5}$ [127]. Eq. (4.4) can be explicitly expressed as:

$$\sigma^*\left(\varepsilon_{eq}, \eta\right) = \sigma_{eq}^0(\varepsilon_{eq})[1 - 3\Upsilon(\eta - \eta_0)]f(\eta)^{0.5} \tag{4.5}$$

where Υ is a proportional, material-dependent constant, η_0 the stress triaxiality for smooth specimen under uniaxial tension, and $f(\eta)$ expressed also as a function of the Poisson's ratio, v [127]:

$$f(\eta) = [\tfrac{2}{3}(1 + v) + 3(1 - 2v)(\eta)^2] \tag{4.6}$$

Following the approach proposed by Bao and Wierzbicki [130], η_0 and η values are calculated based on the concept of average stress triaxiality (η_{av}), as defined below, to take into account the loading history involved in the deformation process.

$$\eta_{av} = \frac{1}{\varepsilon^p_{eq,max}} \int_0^{\varepsilon^p_{eq,max}} \eta(\varepsilon^p_{eq}) d\varepsilon^p_{eq} \tag{4.7}$$

where ε^p_{eq}, $\varepsilon^p_{eq,max}$ and $\eta(\varepsilon^p_{eq})$ are the equivalent plastic strain, maximum equivalent plastic strain (i.e., at onset of fracture), and evolution of stress triaxiality as a function of ε^p_{eq}, respectively, obtained from an element chosen from a finite element (FE) model based on the conventional constitutive equation, as to be detailed later. Note that in this work, η_{av} value will be used to represent η in Eq. (4.5).

4.2.2 Dependence of damage evolution on stress triaxiality

Damage parameter *D* defined in CDM is a variable of thermodynamic state and is used to characterize material degradation during the plastic deformation. Lemaitre [127] and Bonora [128] both proposed ductile damage models that use stress triaxiality and plastic strain as variables. Damage parameter in both models is quantified using repeated loading-unloading tensile tests, but the former assumes a linear relationship between damage accumulation and plastic deformation and the latter a nonlinear relationship. In our study, as to be shown in section 4.4.1, the damage accumulation in the smooth specimen turns out to be a nonlinear function of plastic strain. Thus, Bonora's nonlinear damage model is adopted and modified to fit the experimentally measured data obtained from the study. The original form of the Bonora's damage model is

$$D = D_0 + (\overline{D} - D_0)\left\{1 - [1 - \frac{ln\,\varepsilon_{eq}^{p} - ln\,\varepsilon_{th}}{ln\,\varepsilon_{eq,f}^{p} - ln\,\varepsilon_{th}} f(\eta)]^{\lambda}\right\} \quad (4.8)$$

where D_0 is the initial amount of damage in the specimen before the test, $\overline{D}$ the amount of damage in a smooth specimen at the onset of fracture if the fracture occurs during the homogeneous deformation, $\varepsilon_{eq,f}^{p}$ the equivalent plastic fracture strain for the smooth specimen under uniaxial tension (defined as ε_p^f in the previous two chapters), ε_{th} the threshold plastic strain for damage initiation for which the value is assumed to be the same in both uniaxial and multiaxial stress states, and λ the damage exponent which serves as an adjusting parameter for the calculated deterioration of elastic modulus to fit those measured experimentally.

In the current study, D_0 is chosen to be 0 (i.e., assuming no damage before the test) and λ to be 1. Using the relationship between D and E shown in Eq. (4.2), Eq. (4.8) can be converted to an expression that depicts deterioration of elastic modulus in a deformation process, that is,

$$E = E_0\left[1 - \overline{D} f(\eta_{av}) \frac{ln\varepsilon_{eq}^{p} - ln\varepsilon_{th}}{ln\,\varepsilon_{eq,f}^{p} - ln\,\varepsilon_{th}}\right] \quad (4.9)$$

Note that value for λ in Eq. (4.8) cannot be a fraction, as a fraction value for λ with η larger than 1/3 (the smallest η value for smooth specimen under uniaxial tension) can result in an imaginary number for D once ε_{eq}^{p} approaches the critical value for fracture initiation. Among the possible whole numbers for the λ value, 1 is chosen to fit the experimental data from the loading-unloading tests of smooth specimens, to establish deterioration of elastic modulus with increase of strain, as to be illustrated in section 4.4.1.

4.2.3 The explicit form of the new constitutive model

A constitutive model, as shown below, is proposed here to take into account both damage-free constitutive equation and damage evolution, with the explicit separate expressions for their dependence on stress triaxiality.

$$\sigma_{eq}(\varepsilon_{eq}, \eta_{av}) = \left(1 - \overline{D} f(\eta_{av}) \frac{\langle ln\varepsilon_{eq}^{p} - ln\,\varepsilon_{th}\rangle}{ln\,\varepsilon_{eq,f}^{p} - ln\,\varepsilon_{th}}\right) \sigma_{eq}^{0}(\varepsilon_{eq})[1 - 3\Upsilon(\eta_{av} - \eta_0)] f(\eta_{av})^{0.5} \tag{4.10a}$$

where $\sigma_{eq}(\varepsilon_{eq}, \eta_{av})$ represents the equivalent stress in the conventional constitutive equation with damage involvement, while $\sigma_{eq}^{0}(\varepsilon_{eq})$ is the equivalent stress in the damage-free constitutive equation of the smooth specimen without involving any damage, ε_{eq}^{p} the equivalent plastic strain, and $\langle ln\varepsilon_{eq}^{p} - ln\,\varepsilon_{th}\rangle$ a step function, defined as

$$\langle ln\varepsilon_{eq}^{p} - ln\,\varepsilon_{th}\rangle = \begin{cases} 0 & if\ \varepsilon_{eq}^{p} \le \varepsilon_{th} \\ ln\varepsilon_{eq}^{p} - ln\,\varepsilon_{th} & if\ \varepsilon_{eq}^{p} > \varepsilon_{th} \end{cases} \tag{4.10b}$$

The above step function is imbedded in the damage component of Eq. (4.10a), and is used to trigger the damage evolution once ε_{eq}^{p} is larger than ε_{th}.

For a smooth specimen fractures during the uniform deformation, both η_{av} and η_0 are equal to 1/3, and thus $f(\eta_{av}) = 1$, $[1 - 3\Upsilon(\eta_{av} - \eta_0)] = 1$, and $\varepsilon_{eq}^{p} = \varepsilon_p$ (logarithmic plastic strain for the smooth specimen). These conditions reduce Eq. (10a) to a nonlinear CDM model that is based on von Mises yield criterion. On the other hand, if $\eta_{av} > \eta_0$ and $\Upsilon \neq 0$, Eq. (4.10a) can be used to represent a general stress-strain relationship that contains ductile damage development and damage-free constitutive equation, both expressed as functions of stress triaxiality.

4.3 Characterization of conventional constitutive equation

4.3.1 Materials and test specimens

High-strength rail steel, CZECH TZ IH (CZ) supplied by the Canadian National Railway Company (CN), was used as the sample material to examine the dependence of conventional constitutive equation on the stress triaxiality. Both monotonic and cyclic loading-unloading tensile tests were conducted at room temperature using an Instron hydraulic universal testing machine with load capacity of 222 KN.

Two types of notch-free specimens were used which as shown in Figure 4.2, are named smooth and short-gauge specimens. Gauge section dimensions of the smooth specimens follow those specified in ASTM E8/E8M-11 [17], but gauge length for short-gauge specimens is shortened to increase transverse stress so that this type of specimens provides deformation and fracture behaviour at a stress triaxiality level much higher than that in the smooth specimens. Note that no taper was introduced to the smooth specimens for the monotonic tensile tests, but a taper to the smooth specimens for the cyclic loading-unloading tensile tests by reducing diameter by 2% in the middle of the gauge section where an extensometer was placed, in order to encourage neck initiation and fracture there.

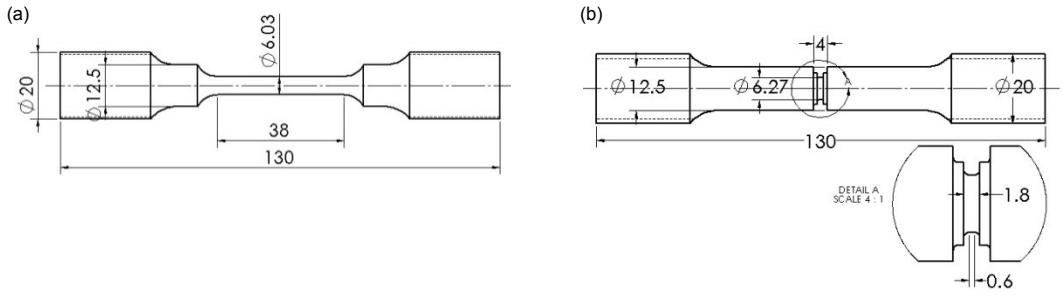

Figure 4.2 Geometry and dimensions of (a) smooth and (b) short-gauge specimens

4.3.2 Fundamental mechanical properties

Monotonic tensile tests were carried out on smooth specimens to obtain basic mechanical properties for the CZ rail steel. Three specimens were tested at a crosshead speed of 8.5×10^{-3} mm/s, equivalent to an initial strain rate of 2.36×10^{-4} /s. Each smooth specimen had two extensometers placed in the middle of the gauge section, to measure simultaneously elongation and diameter changes. Based on the assumption of uniform stress and strain distributions along the gauge section and negligible volume change during the deformation, the true stress (σ) and logarithmic strain (ε) were calculated using the equations below [103]

$$\sigma = L/A \tag{4.11}$$

$$\varepsilon = ln(A_0/A) \tag{4.12}$$

where L is tensile load, A_0 the original cross-sectional area, and A the corresponding cross-sectional area measured during the test.

Monotonic tensile tests were also carried out on short-gauge specimens using the same conditions as those for the smooth specimens. However, because of the straight gauge length of 0.6 mm for the short-gauge specimens, as shown in Figure 4.2(b), only the diametric extensometer was used to quantify deformation in the gauge section. The axial extensometer was clipped outside of the gauge section with the initial length of 4 mm. Note that the true stress and logarithmic strain for the short-gauge specimens were also calculated using Eqs. (4.11) and (4.12), based on the assumption of uniform stress and strain distributions on the cross section. However, this assumption was relaxed in section 4.4.3, to consider variation of stress and strain distributions on the cross section in the study of the influence of stress triaxiality on the damage-free constitutive equation.

Figure 4.3 presents axial true stress-logarithmic strain curves for the smooth and short-gauge specimens, and Table 4.1 the corresponding mechanical properties including Young's modulus (E_0), yield stress (σ_y), ultimate tensile strength (UTS), fracture stress (σ_f) and plastic fracture strain (ε_p^f). The test results indicate that with the gauge length reduced from 38 to 0.6 mm, fracture stress for the rail steel is increased by about 20% while the fracture strain reduced over 80%.

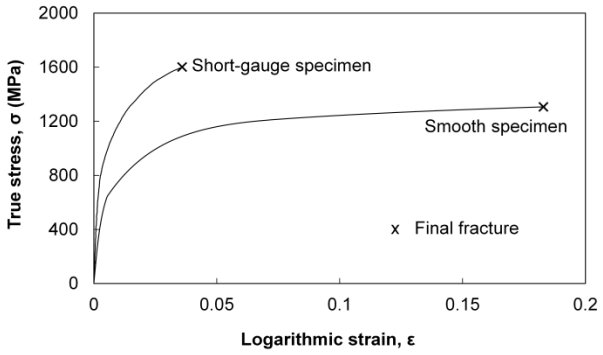

Figure 4.3 Typical experimentally-determined stress-strain curves for smooth and short-gauge specimens of the CZ rail steel

Table 4.1 Fundamental mechanical properties for the CZ rail steel

Type	Smooth specimen					Short-gauge specimen	
Properties	E_0(GPa)	σ_y(MPa)	UTS(MPa)	σ_f(MPa)	ε_p^f(%)	σ_f(MPa)	ε_p^f(%)
Values	193	632	1130	1307	18.3	1587	3.4

4.3.3 Conventional constitutive equation

The conventional constitutive equation for the railhead of the CZ rail steel, determined in Chapter 2, was applied to a 3D FE model of smooth specimen using ABAQUS standard 6.13. In view of the axi-symmetry of the specimen geometry, the FE model has only quarter of the cross section, consisting of 94,200 standard linear hexahedral 8-node elements with reduced integration and 104,265 nodes, for which dimensions followed those given in Figure 4.2(a) except that a

small taper was introduced in the gauge section to reduce the cross-sectional diameter by 0.1% at the location where necking and fracture were observed from the experimental testing. The FE model was evenly discretized in the gauge section, with element size of 0.167 mm longitudinally and aspect ratio of 1. The classical J_2 plasticity with isotropic strain hardening was selected for the simulation. Boundary conditions were set to be the same as those used in the experimental testing, i.e., with one end fixed and the other end moving at a specified displacement rate.

The same conventional constitutive equation of the CZ rail steel was also applied to a 3D FE model of short-gauge specimen with quarter of the cross section. The model consists of 178,800 standard linear hexahedral 8-node elements with reduced integration and 189,103 nodes of which the dimensions follow those given in Figure 4.2(b). The FE model was evenly discretized with element size of 0.078 mm and aspect ratio of 1 in the 0.6 mm-long gauge section. One end of the model was fixed while the other end subjected to the displacement-controlled boundary condition. Figure 4.4(b) presents the experimentally determined load-elongation and diameter reduction curves (represented by dashed lines) for the short-gauge specimens, compared with the curves generated from the FE models (represented by open squares).

The curves in Figure 4.4 suggest that results from the FE models of smooth and short-gauge specimens, based on the same conventional constitutive equation, agree reasonably well with the experimental testing results, having only slight deviation for the curves of diameter reduction. Therefore, the conventional constitutive equation for the CZ rail steel used in the study shows little sensitivity to the change of stress triaxiality. This is consistent with one of the tenets of classical metal plasticity theory, as stated in Introduction 4.1.

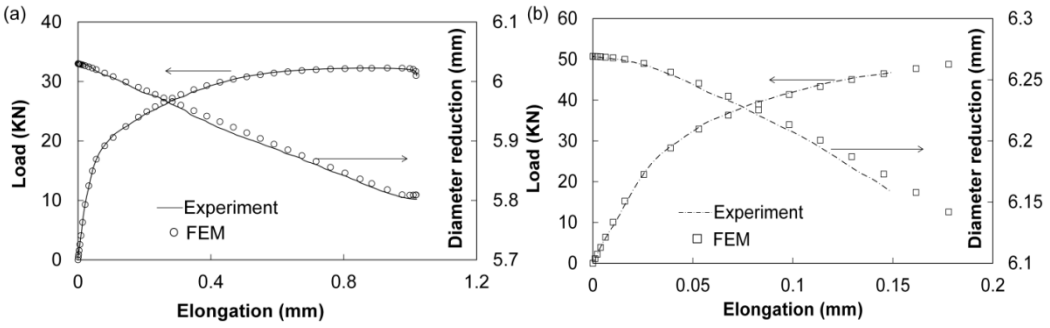

Figure 4.4 Comparison of load and diameter reduction as functions of elongation between experiment and FE simulation for (a) smooth and (b) short-gauge specimens

4.4 Calibration of new constitutive model

The constitutive model expressed by Eq. (4.10a) contains three parameters ($\overline{D}$, $\sigma_{eq}^{0}(\varepsilon_{eq})$, and Υ) that need to be calibrated so that Eq. (4.10a) can be applied to the CZ rail steel. As to be described in this section, three steps were used in the study to determine values for the three parameters. The first step was to use results from loading-unloading tensile tests on smooth specimens to determine variation of unloading elastic modulus as a function of plastic strain, based on which $\overline{D}$ could be determined by fitting the curve generated from Eq. (4.9) to the experimentally measured elastic modulus values. The second step was to determine value for $\sigma_{eq}^{0}(\varepsilon_{eq})$ by conducting FE modelling of smooth specimen using separate inputs of damage evolution, defined in Eq. (4.2), and $\sigma_{eq}^{0}(\varepsilon_{eq})$, where the former was determined using the measured elastic modulus from the loading-unloading tensile tests, and the latter through the iterative FE modelling till the experimentally measured variation of load and cross sectional diameter, as functions of elongation, matched those from the FE modelling. With $\overline{D}$ and $\sigma_{eq}^{0}(\varepsilon_{eq})$ determined, the last step was to determine the Υ value in Eq. (4.10a), through an iterative FE modelling process of short-gauge specimen so that the FE model can regenerate the data from the experimental testing. Results from the above three steps are summarized below. Note that value for η_{av} in Eq. (4.10a)

was determined using Eq. (4.7), based on stress triaxiality in the FE models of smooth and short-gauge specimens using the conventional constitutive equation.

4.4.1 Damage parameter

Results from the loading-unloading tensile tests on smooth specimens are used to determine the value for $\overline{D}$. As mentioned earlier, gauge section of the smooth specimens for the loading-unloading tests is tapered to reduce diameter in the middle by 2%, to ensure that neck formation and specimen fracture occur there so that the diametric extensometer mounted in the middle of the gauge section can record the diameter change till fracture is initiated. Crosshead speed used for the loading-unloading tests on smooth specimens is same as that used for the monotonic tensile tests. Condition for triggering the unloading before the UTS is based on the load increment of 2 kN, but after UTS based on the displacement increment of 0.25 mm which corresponds to a loading period of 30 seconds.

Effective elastic modulus (E) was determined using the linear portion of the unloading part of the stress-strain curves from the loading-unloading tests of smooth specimens, following the approach described by Lemaitre and Dufailly [192]. Due to the increase of stress triaxiality after the necking starts, the measured unloading slope from the smooth specimens is also affected by the change in the gauge section geometry. Such an influence was removed using the approach described by Celentano and Chaboche [193]. After this correction, variation of E can then be established as a function of plastic strain, which is then used to calibrate $\overline{D}$ value in Eq. (4.9) so that the curve generated from Eq. (4.9) can fit the trend of change for the measured E values.

Figure 4.5 depicts the above procedure for the CZ rail steel. Figure 4.5(a) compares curves of true stress versus logarithmic strain for a smooth specimen under the loading-unloading tensile test and from the FE modelling based on the conventional constitutive equation. The loading-unloading test is to determine the unloading slope and the FE modelling to correct the effect of gauge section

geometry on the unloading slope. The FE model for the loading-unloading tensile test is same as that used for the monotonic tensile tests, except that the former has a taper in the gauge section to reduce diameter in the middle by 2%, which reflects the physical taper introduced to the specimens. The FE model has one end completely constrained from any movement, while the other end is subjected to a displacement-controlled cyclic loading. As shown in Figure 4.5(a), the monotonic part of the curve from the FE modelling agrees well with that from the experimental testing.

Figure 4.5(b) shows variation of the geometric correction factor β, defined in Eq. (4.14a) and determined from the FE model, as a function of logarithmic plastic strain (ε_p) for smooth specimen, following the approach proposed by Celentano and Chaboche [193].

$$\beta(\varepsilon_p) = \frac{E_0}{S_{FEM}} \tag{4.14a}$$

where E_0 is the original elastic modulus and S_{FEM} the unloading slope in the loading-unloading true stress-logarithmic strain curves, established from the FE model based on the conventional constitutive equation.

As shown in Figure 4.5(b), β value for the smooth specimen remains relatively constant when deformation in the gauge section is uniform, but starts decreasing at the onset of necking. This phenomenon is consistent with that reported before [193]. Since the FE model mimics closely the deformation behaviour observed from the experimental testing, variation of β value shown in Figure 4.5(b) should also be reflected by results from the experimental testing. That is,

$$\beta(\varepsilon_p) = \frac{E}{S_{exp}} \tag{4.14b}$$

where E is the experimentally measured elastic modulus and S_{exp} the unloading slope from the true stress-logarithmic strain curve from the loading-unloading tests. Therefore, variation of E with ε_p for the smooth specimens of the CZ rail steel used in the study can be determined by multiplying β with S_{exp}, which is shown in Figure 4.5(c).

Figure 4.5(c) also includes a curve generated from Eq. (4.9), with ε_{th} chosen to be the yield strain of 0.002, Young's modulus (E_0) and plastic strain at final fracture ($\varepsilon_{eq,f}^{p}$) determined from the experimental testing, and average stress triaxiality (η_{av}) obtained from the FE modelling of smooth specimen under monotonic tension. Therefore, Eq. (4.9) has only $\overline{D}$ as the adjusting parameter for the curve in Figure 4.5(c) to fit the experimental data based on the least square fitting procedure. With the $\overline{D}$ value determined, damage evolution in smooth specimen of the CZ rail steel up to the fracture initiation can then be expressed as a function of ε_p using Eqs. (4.2) and (4.9), as presented in Figure 4.5(d).

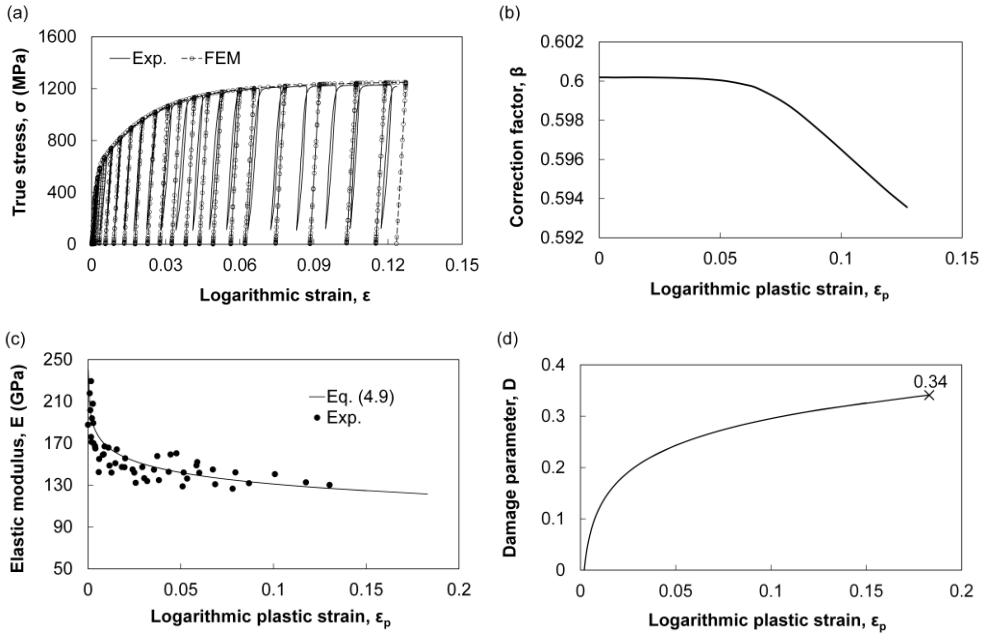

Figure 4.5 Summary of results from the experimental testing and the FE simulation for loading-unloading tests of smooth specimens: (a) numerical and experimental loading-unloading tensile tests, (b) correction factor β, (c) effective elastic modulus E, and (d) damage parameter D

Table 4.2 Summary of values for parameters in Eq. (4.9) for the CZ rail steel

Parameters of smooth specimen					
E_0 (GPa)	$\overline{D}$	η_{av}	ε_{th}	$\varepsilon^p_{eq,f}$	D_{cr}
193	0.33	0.37	0.002	0.183	0.34

Table 4.2 summarizes values for the parameters in Eq. (4.9) for the CZ rail steel, in which D_{cr} is the critical damage parameter for smooth specimens, determined using the curve in Figure 4.5(d) at the onset of fracture, as indicated by the cross symbol in Figure 4.5(d). As mentioned earlier, $\overline{D}$ was the only fitting parameter used for the curve generated by Eq. (4.9) to fit the experimental data in Figure 4.5(c). Value for $\overline{D}$ represents the critical damage value for smooth specimens if fracture were initiated before the onset of necking. For the CZ rail steel, since $\varepsilon^p_{eq,f}$ is 18.3% which is not far from the strain for the onset of necking (7.1%), with the calculated η_{av} to be only 0.37 (compared to 0.33 for η during the uniform deformation), it is not surprising that values for D_{cr} and $\overline{D}$ in Table 4.2 are very close to each other.

4.4.2 Damage-free constitutive equation

The damage-free constitutive equation was established using ABAQUS explicit 6.13. FE model for this part of study has the same mesh pattern as that used in the previous section but the element type has been changed to explicit linear brick elements with reduced integration. Material property input to the FE model contains two parts. The first part is damage evolution that includes both damage initiation and evolution, established from loading-unloading tensile tests with the assumption that damage starts at the yield point with the stress triaxiality of 1/3 and damage evolution follows that depicted in Figure 4.5(d). The second part is the damage-free constitutive equation with the isotropic strain hardening, established by adjusting values for parameters in Eq. (2.4) so that the FE model can regenerate the loading part of the results from the loading-unloading tests,

including load-elongation and cross section reduction curves. In addition, the final unloading curve from the FE model was compared with that from the experimental testing to examine their consistency. Same as before, caution was taken to make sure that the 0^{th} and 1^{st} orders of continuity were met for the damage-free constitutive equation at the coincident points between the adjacent sections of the curve. It is worth mentioning that ratio of kinetic energy to internal energy for this model was less than 1%, thus satisfying the condition for the quasi-static analysis.

In order to alleviate the mesh dependency of the results from the FE simulation, due to the involvement of damage development, input of damage evolution based on that depicted in Figure 4.5(d) was expressed as a function of equivalent plastic displacement, as shown in Figure 4.6(a), following the suggestion given by Hillerborg et al. [194]. The equivalent plastic displacement is the product of the increment of plastic strain from 0.002 and characteristic length of the linear brick element (0.167 mm for the FE model of smooth specimen). Boundary conditions for the FE model are same as those used before, that is, with one end of the specimen fixed and the other end under the displacement control.

Figures. 4.6(b) and 4.6(c) compare results from the above FE model for smooth specimen with those from the experimental testing of the CZ rail steel. The figures suggest that good agreement exists between the FE simulation and the experimental testing, with less than 2% difference in both the loading path and the final unloading slope. Although the unloading slope is compared only for the final unloading stage, slopes from the other unloading stages are also expected to show good agreement. This is because ABAQUS explicit assumes that the progressive accumulation of ductile damage depends solely on the amount of plastic deformation, not the unloading path. Therefore, once the FE model can regenerate the unloading slope for the final stage, it is also expected to regenerate unloading slopes for the other unloading stages.

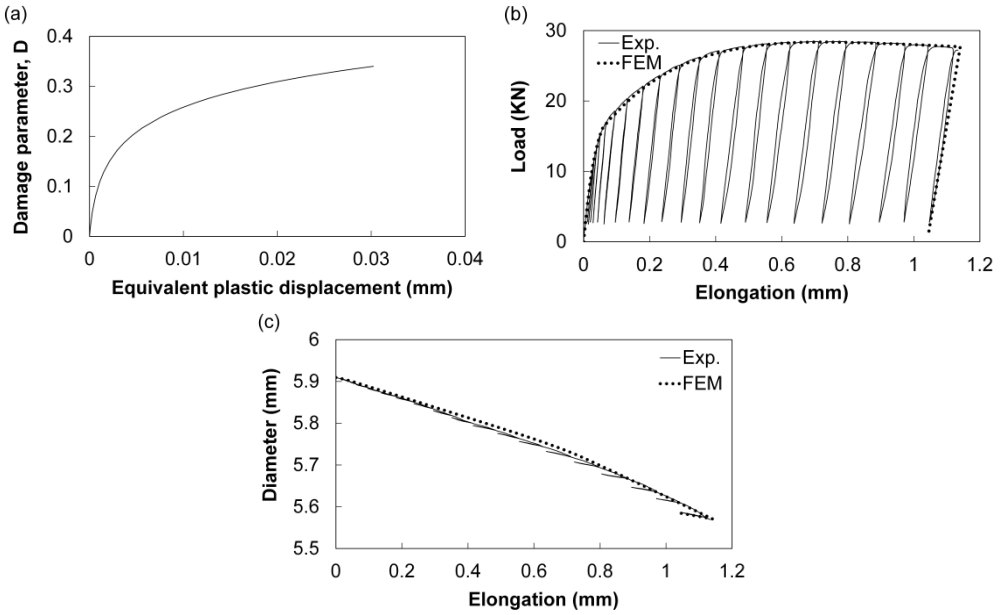

Figure 4.6 Comparison of data from the experimental testing with those from the FE simulation for smooth specimen, using separate material input for damage evolution and damage-free constitutive equation: (a) damage evolution as a function of equivalent plastic displacement, (b) load-elongation curve, and (c) diameter reduction as a function of elongation

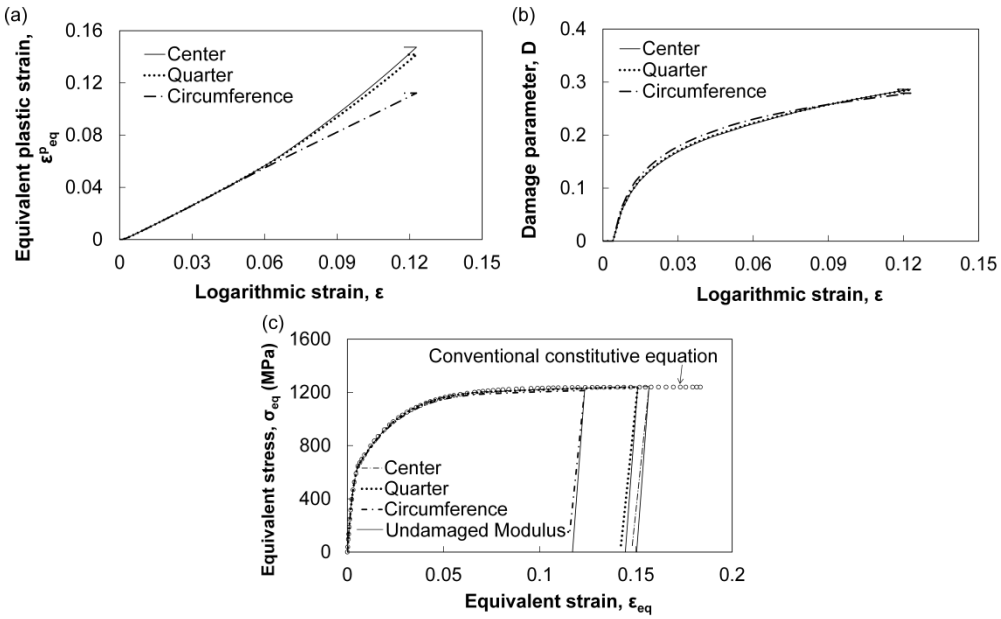

Figure 4.7 Results from FE simulation of loading-unloading of smooth specimen at three points on the minimum cross section: (a) equivalent plastic strain, (b) damage evolution, and (c) equivalent stress-strain curves

Figure 4.7 presents results from the elements located at the centre, quarter of diameter from the centre, and along the circumference on the minimum cross section of the FE model for smooth specimen, using separate inputs for damage-free constitutive equation and damage evolution. Figure 4.7(a) describes variation of the equivalent plastic strain (ε_{eq}^{p}) as a function of logarithmic strain ($\boldsymbol{\varepsilon}$) of the cross section, suggesting that ε_{eq}^{p} at the three locations has very similar values during the uniform deformation. However, the ε_{eq}^{p} values start deviating from each other after the necking starts. At the maximum elongation, i.e., before the unloading stage in the FE simulation, the element at the centre of the minimum cross section has the biggest ε_{eq}^{p}value and the element along the circumference the smallest. Figure 4.7(b) depicts the damage evolution as a function of ε in the three elements, showing little difference among the three locations for the damage development. This suggests that smooth specimen generates a relatively uniform damage distribution on the cross section. Note that as shown in Figure 4.7(b), for ε value smaller than 0.07, i.e., before the onset of necking, rate of damage development in the element along the circumference of the cross section is slightly faster than that in the centre. This is probably because of the 2% taper in the gauge section of the FE model, which has increased the local deformation along the circumference of the minimum cross section.

The most interesting phenomenon observed from this FE simulation is the equivalent stress-equivalent strain curves during the loading path, as shown in Figure 4.7(c), which are constructed based on the output from the three elements of the FE model. Evolution of the three curves in Figure 4.7(c) is in excellent agreement, not only with each other but also with the conventional constitutive equation (presented using open circles in Figure 4.7(c) which was used as the material input to generate FE simulation data for Figure 4.4. Although this agreement suggests the possibility of using FE simulation based on the conventional constitutive equation to regenerate deformation behaviour of the

smooth specimen under the monotonic loading, the use of conventional constitutive equation fails to regenerate the change of the unloading slope observed from the experimental testing, as depicted in Figure 4.7(c). Note that the unloading curves generated from a FE model based on the conventional constitutive equation are represented by three solid lines in Figure 4.7(c), compared with three dashed lines that represent the unloading curves generated from the FE model with separate inputs of damage-free constitutive equation and damage evolution. Figure 4.7(c) indicates clearly that slope for each of the three dashed lines is smaller than that for the solid lines.

Contour plots from the FE models of smooth specimen, right before the fracture initiation, are presented in Figure 4.8. The contour plots in Figure 4.8(a) are from the FE model in the ABAQUS standard based on the conventional constitutive equation as the material input, thus showing distribution of equivalent plastic strain (PEEQ), von Mises stress (Mises) and hydrostatic stress (Pressure). The contour plots in Figure 4.8(b), on the other hand, are from the FE model in the ABAQUS explicit using separate inputs of damage evolution and damage-free constitutive equation. As a result, Figure 4.8(b) also includes a contour plot of the damage parameter (SDEG). Overall, the two approaches give similar results for PEEQ, Mises and Pressure. For SEDG, Figure 4.8(b) shows that its maximum value occurs on the minimum cross section, suggesting that fracture is expected to start from there. Note that the label "Avg: 75%" shown on each of the contour plots in Figure 4.8 is the nodal averaging threshold. This "75%" means that when the element-based variables, i.e., PEEQ, Mises, Pressure, and SDEG, are extrapolated to the nodes from the integration points, those nodal results will be averaged and displayed continuously if they are within 75%. In other words, if the difference is more than 25% from each other, a discontinuity will be displayed. This threshold value of 75% is a default setting in ABAQUS and can be changed in ABAQUS/Viewer-Results-Options-Computation tab-Averaging.

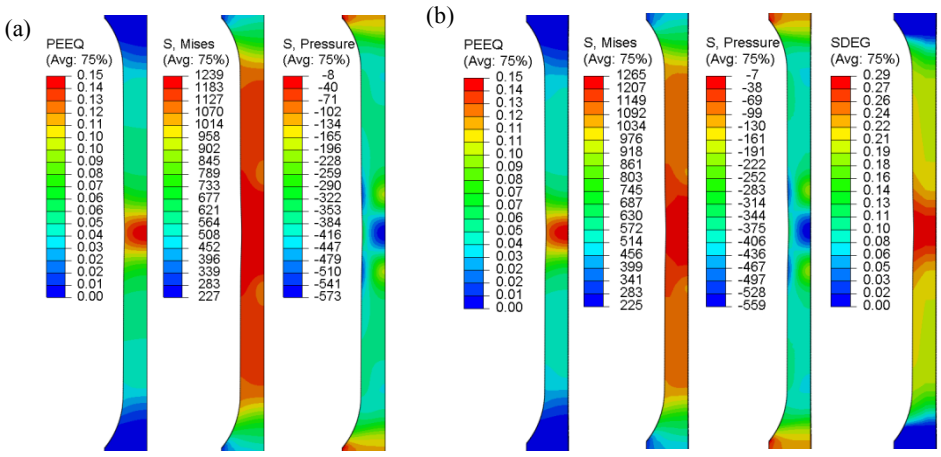

Figure 4.8 Contour plots for equivalent plastic stain (PEEQ), von Mises stress (Mises in MPa), hydrostatic stress (Pressure in MPa), and damage parameter (SDEG) from the FE modelling: (a) using the conventional constitutive equation and (b) using separate inputs for damage evolution and damage-free constitutive equation

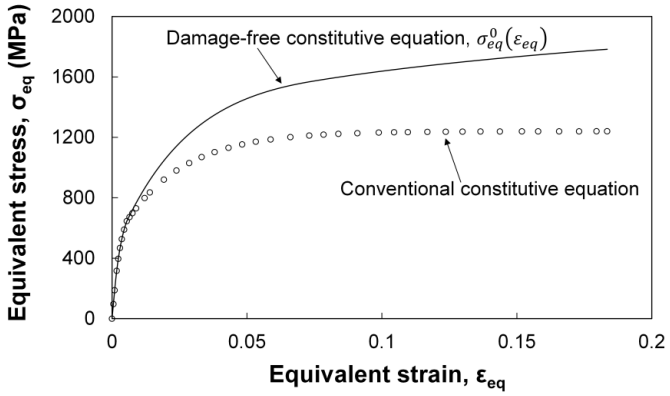

Figure 4.9 Comparison of conventional constitutive equation and damage-free constitutive equation for smooth specimens of the CZ rail steel

Table 4.3 Parameters in Eq. (2.4) for conventional and damage-free constitutive equations of smooth specimen

Parameters		Constitutive equation	
		Conventional	Damage-free
Eq. 2.4(a)	E (GPa)	193	193
	v	0.3	0.3
Eq. 2.4(b)	a (MPa)	30	30
	b	0.0101	0.0101
	c	-2	-2
	d	-26	-26
	e (MPa)	894	894
Eq. 2.4(c)	α (MPa)	452	420
	$\bar{\beta}$ (MPa)	1240	1650
	γ	45.0	37.0
Eq. 2.4(d)	M (MPa)	1502	2261
	n	0.082	0.140

Figure 4.9 compares damage-free and conventional constitutive equations for the smooth specimen of the CZ rail steel. As expected, the former shows a higher strain-hardening effect than the latter. The less significance in strain hardening for the conventional constitutive equation comes from the inclusion of the damage effect on the stress response to deformation. Table 4.3 summarizes values for all parameters in Eq. 2.4 for the two types of constitutive equations, in which the difference is mainly for parameters in Eqs. 2.4 (c) and 2.4(d).

4.4.3 Material constant

With $\overline{D}$ and $\sigma_{eq}^{0}(\varepsilon_{eq})$ determined, even without knowing the value for ϒ, Eq. (4.10a) can be used to represent the stress-strain relationship for smooth specimens. This is because in this case both η_{av} and η_0 are equal, thus eliminating the term in Eq. (4.10a) which contains ϒ. In general, however, value for ϒ needs to be determined in order to express the stress response to strain at different stress triaxiality levels. This was achieved in this study by conducting FE modelling of short-gauge specimens, to generate results that match the experimental data from monotonic tensile tests. The FE model for short-gauge specimen used here is

identical to that used in section 3.3 except that material property input for the former is based on Eq. (4.10a) with ϒ as an adjustable material constant which is independent of stress triaxiality. In view that stress triaxiality is not uniform in the short-gauge specimen, constitutive equation for the FE model based on Eq. (4.10a) should vary with the change of stress triaxiality. Ideally, a user-defined subroutine should be used to consider dependence of the constitutive equation on the stress triaxiality. Here, however, an approximation approach is adopted, by dividing the cross section into five annular regions. Stress triaxiality is expected to vary among the five annular regions, but remains constant in each annular region. As to be shown in this section, such an approximation is acceptable for the purpose of determining the ϒ value. Note that ϒ is a material constant that is treated as being independent of the stress triaxiality variation.

Figure 4.10 presents the FE model for short-gauge specimen used to determine the ϒ value. Figure 4.10(a) depicts an overall, sectional view of the FE model that has the same dimensions and mesh pattern as the model used to obtain data for Figure 4.4(b), but gauge section in the former is divided into five zones of equal length in the radial direction, corresponding to the five annular regions on the cross section. Material property input for each zone is dependent on stress triaxiality. Figure 4.10(b) presents an example of the variation of equivalent plastic strain (ε_{eq}^{p}) and stress triaxiality (η) in the radial direction of the minimum cross section at the onset of fracture, determined from the FE model based on the conventional constitutive equation. Note that Figure 4.10(b) presents three curves for each of ε_{eq}^{p} and η, determined from the FE model with different mesh sizes in the gauge section, with elements of 0.157, 0.078, and 0.039 mm in length, respectively. These curves in Figure 4.10(b) suggest that little difference is detectable by varying the element size. Therefore, the FE model with element size of 0.078 mm was used for the study, to save computational time but still provide satisfactory resolution. In addition to those curves, Figure 4.10(b) also includes four solid vertical lines that divide the radial length into five zones. Equivalent

plastic strain ($\overline{\varepsilon_{eq}^{p}}$) for each zone, marked by a horizontal dash line on the curve with its value given in the figure, is taken as the mean ε_{eq}^{p} value for all elements in that zone. Similarly, stress triaxiality for each zone ($\overline{\eta_{av}}$) is taken as the mean value of η_{av} for all elements in that zone, also given in Figure 4.10(b). These five $\overline{\eta_{av}}$ values, together with $\overline{D}$ and $\sigma_{eq}^{0}(\varepsilon_{eq})$ determined from the previous sections, were substituted into Eq. (4.10a) to establish the constitutive equation for the FE model that was used to determine ϒ value for the CZ rail steel.

Figure 4.11 summarizes variation of load as a function of logarithmic strain (ε) from the above FE model of short-gauge specimen with ϒ equal to 0 or 0.1, compared with the curve generated from the FE model based on the conventional constitutive equation (i.e., without considering the dependence of constitutive equation on the stress triaxiality) and two curves from the experimental testing. The figure suggests that by increasing ϒ value from 0 to 0.1, the curve generated by the FE model based on Eq. (4.10a) matches well with those from the experimental testing. The small ϒ value required to have a good match with the experimental data suggests that the above approximation approach is acceptable for the purpose of determining the ϒ value. Figure 4.11 also suggests that even though both conventional constitutive equation and Eq. (4.10a) with ϒ =0.1 can enable the FE model to generate the load-logarithmic strain curve that is close to those from the experimental testing, the curve based on the latter shows a better fit than that based on the former.

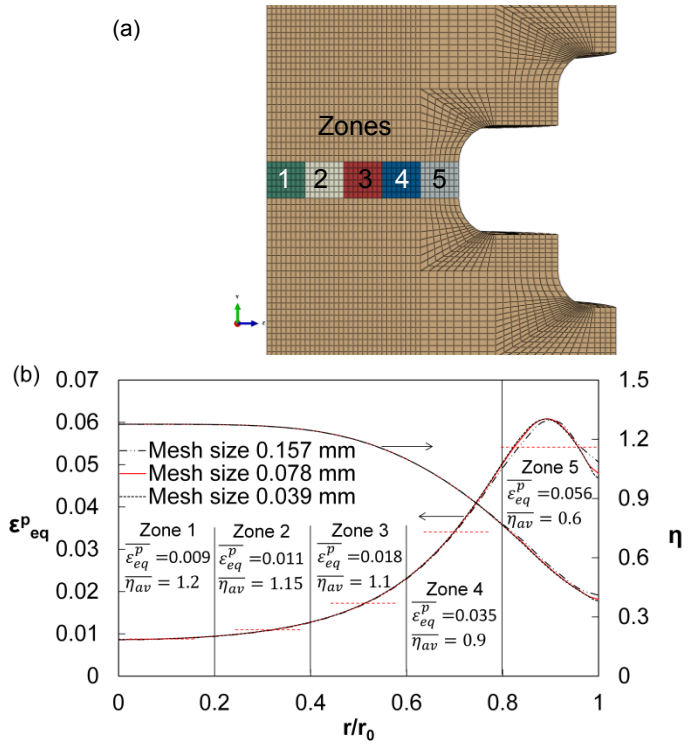

Figure 4.10 FE model of short-gauge specimen: (a) showing five zones in the gauge section with different material property inputs and (b) variation of equivalent plastic strain and stress triaxiality in the radial direction of the cross section and the corresponding average values for each of the five zones at the onset of fracture

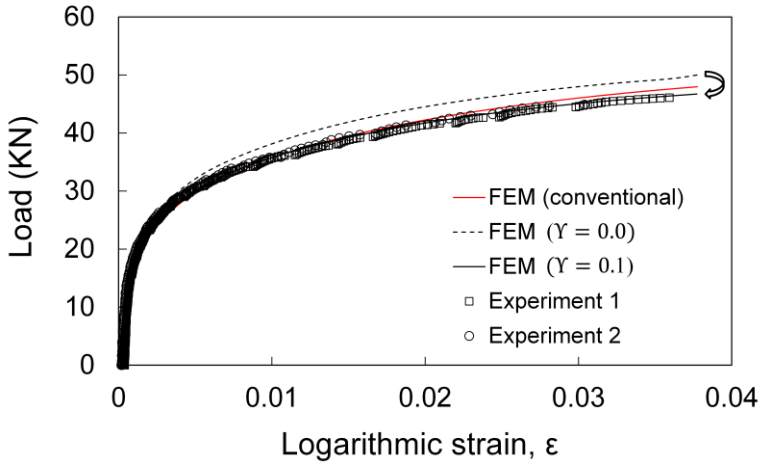

Figure 4.11 Comparison of load-logarithmic strain curves for short-gauge specimen, from experimental testing and FE simulations (based on Eq. (4.10a) or the conventional constitutive equation)

4.5 Discussion

With $\overline{D}$, $\sigma_{eq}^{0}(\varepsilon_{eq})$ and Υ identified, Eq. (4.10a) can be regarded as a constitutive model for the CZ rail steel. The first part of the constitutive model depicts the damage evolution and the second part represents the damage-free constitutive equation. The constitutive model suggests that stress triaxiality has influence on both damage evolution and damage-free constitutive equation. Explanation is explored here for this constitutive model to yield the conventional constitutive equation that is independent of the variation of stress triaxiality.

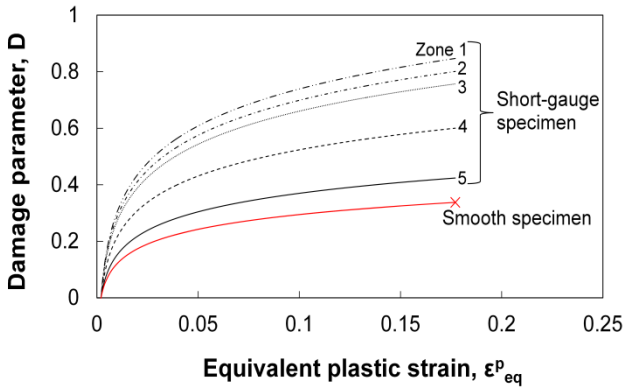

Figure 4.12 Damage evolution in smooth and five zones of short-gauge specimens

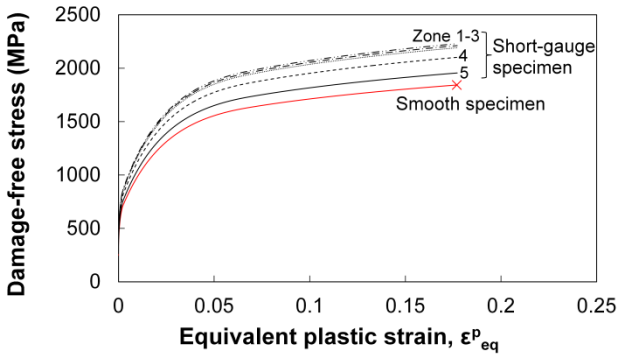

Figure 4.13 Damage-free constitutive equations for smooth and five zones of short-gauge specimens

Figure 4.12 shows the variation of D with the increase of ε_{eq}^{p} for both smooth and short-gauge specimens. Note that since stress triaxiality is uniformly distributed on the minimum cross section of the smooth specimen, its damage evolution can be expressed by one curve in which a single critical D value is needed to define the initiation of final fracture. For the short-gauge specimen, on the other hand, non-uniform distribution of stress triaxiality on the cross section has yielded dependence of damage evolution on both ε_{eq}^{p} and stress triaxiality. In Figure 4.12, influence of stress triaxiality on D is presented using five curves, each for one of the five zones in Figure 4.10(a). Figure 4.12 suggests that damage evolution in any of the five zones in the short-gauge specimen has a higher rate than that in the smooth specimen. Among the five zones in the short-gauge specimen, damage evolution rate is higher in the zone that has a higher $\overline{\eta_{av}}$ value. In view of the dependence of damage evolution rate on the stress triaxiality, critical D value for fracture initiation may also depend on the stress triaxiality. This requires further study for clarification.

Figure 4.13 shows damage-free constitutive equations for both smooth and short-gauge specimens. For the short-gauge specimen, due to non-uniform distribution of stress triaxiality, five curves are used to represent the damage-free constitutive equation, one for each zone of Figure 4.10(a). As indicated by Figure 4.13, at a given ε_{eq}^{p} level, damage-free stress response to strain increases with the increase of stress triaxiality. Although the concept of damage-free stress-strain curves has been reported previously [183, 186, 195, 196], only Malcher et al. [195] established the damage-free stress-strain curves for smooth tensile and butterfly specimens which cover the stress triaxiality in the range from 0 to 0.33. Results from their study suggest that higher the stress triaxiality generated in the specimen lower the strain-hardening of the damage-free stress-strain curve. This is inconsistent with the results from our study, as shown in Figure 4.13, that is, the damage-free stress-strain curves increase with the increase of stress triaxiality. However, the results from our study cover the range of stress triaxiality from 0.33

to 1.2, which is quite different stress state. Thus, further study is deserved for clarification.

In view of Figures 4.12 and 4.13, we believe the explanation for the independence of conventional constitutive equation on the change of stress triaxiality is that the increase of damage-free stress response to deformation caused by the increase of stress triaxiality is offset by the stress decrease due to the increase of damage. That is, with the increase of stress triaxiality, both damage evolution rate and damage-free constitutive equation increase, causing strain-softening and strain-hardening of the material, respectively. For the CZ rail steel, these two effects counter-balance each other, resulting in the insensitivity of the conventional constitutive equation to the change of stress triaxiality.

The proposed constitutive model also suggests that it is possible for the conventional constitutive equation to show dependence on the change of stress triaxiality. For example, for 2024-T351 aluminum [167], the dependence of the conventional constitutive equation on the change of stress triaxiality is possibly because of the different levels of dependence of damage evolution and damage-free constitutive equation on the change of stress triaxiality. That is, with the increase of stress triaxiality, the decrease in stress caused by the increase of damage evolution cannot be fully offset by the increase in stress caused by the increase of damage-free constitutive equation. We believe that different levels of sensitivity of the damage evolution and the damage-free constitutive equation to the change of stress triaxiality are governed by the magnitude of Υ value. By increasing Υ value in Eq. (4.10a), sensitivity of the damage-free constitutive equation to the increase of stress triaxiality is reduced and may not be sufficient to offset the stress decrease caused by the increase of damage evolution. This may result in the conventional stress-strain curve at a notch tip being lower than for smooth specimen. However, further study using materials for which the conventional constitutive equation is sensitive to the stress triaxiality is needed to verify this concept.

4.6 Conclusion

In this study, a constitutive model that considers the influence of stress triaxiality on both damage evolution and damage-free constitutive equation is postulated. By decoupling the damage evolution from the damage-free constitutive equation, the study found that they both are sensitive to the change of stress triaxiality. Using this constitutive model, independence of the conventional constitutive equation on the stress triaxiality for a high-strength rail steel is explained. That is, the apparent independence of the conventional constitutive equation from the increase of stress triaxiality results from the decrease of stress caused by the increase of damage evolution being offset by the increase of damage-free constitutive equation.

Chapter 5 Indentation fracture toughness of high-strength rail steels based on a stress-triaxiality-dependent ductile damage model[4]

5.1 Introduction

Indentation test is an attractive alternative technique to the conventional destructive test methods, especially for monitoring property change in structural components for which functions may be interrupted by the destructive tests. The indentation test was originally developed for measuring material hardness (H) that was related to flow stress [197-199]. An advanced version of the hardness test was later developed [200], from which the curve of load-contact depth can be used to determine Young's modulus (E_0), based on the Hertzian contact theory [201] and the Sneddon's elastic punch theory [202]. With the development of high-resolution, depth-sensing instruments, Doerner and Nix [114] used the indentation load-depth curve to determine both H and E_0 for thin films. Their work demonstrated the possibility of using data directly from the indentation test to determine mechanical properties, without relying on any image analysis. Further improvement was made by Oliver and Pharr [203] from the discovery of the dependence of the measurement accuracy on the presence of pile-up that varies with the levels of strain hardening [204-207] and contact depth [208, 209]. Consequently, the influence of pile-up on the measurement accuracy was extensively studied. Some researchers [210-212] multiplied the measured contact depth (i.e., without the consideration of pile-up) by a coefficient to represent the actual contact depth due to the presence of pile-up, while others applied the work

[4] Part of this chapter has been published in the following publication:
1. Yu, F., Jar, B. and Hendry, M., 2016, July. Critical Strain and Damage Evolution for Crack Growth From a Sharp Notch Tip of High-Strength Steel. In ASME 2016 Pressure Vessels and Piping Conference (pp. V06AT06A029-V06AT06A029). American Society of Mechanical Engineers.
2. Yu, F., Jar, B. and Hendry, M., Indentation fracture toughness of high-strength rail steels based on a stress-triaxiality-dependent ductile damage model. (under review at Journal of Theoretical and Applied Fracture Mechanics)

of energy introduced by the indentation to determine the actual contact depth [213-216]. In addition to the pile-up, the accuracy of E_0 was also known to be affected by the loading frame compliance, which was initially assumed to remain constant during the test [203, 217]. However, recent studies have suggested that the loading frame compliance can vary with the contact depth and the variation should be considered to calculate E_0 [218, 219]. With the above advancement, indentation test is now used not only as a non-destructive technique to measure mechanical strength and $E_{0,}$ but also as a tool to establish the stress-strain relationship for metals [220-223].

For brittle materials such as ceramics, cracks are generated under indentation. Thus, the indentation loading is also deemed to be feasible for determining fracture resistance [76-79, 224], even though some researchers have argued that any agreement between the estimated fracture toughness using the indentation test and that measured using the standard destructive test is fortuitous or by force-fitting the calibration constants [225-228]. For materials that involve plastic deformation before crack formation, however, indentation test is yet to be accepted for estimating the fracture toughness. This is because cracks are not likely to be generated in ductile materials by the indentation loading. Therefore, fracture toughness estimated by indentation test (K_{Ind}) has to be based on a critical contact depth at which the specific indentation energy is deemed to correspond to the specific work of fracture for crack initiation from the crack tip under tensile deformation [80, 82, 87]. This approach requires the assumption that both the crack tip and the indenter tip generate a highly concentrated stress field at a similar level of stress triaxiality (defined as a ratio of hydrostatic stress to von Mises stress). Under this assumption, existing approaches for determining the critical contact depth can be categorized based on the following three criteria: (i) critical fracture stress [81, 87], (ii) critical fracture strain [88, 89], and (iii) critical damage parameter [82-86].

The first and second criteria above are based on the critical fracture stress and strain at the crack tip, respectively [81, 89]. For the third criterion, however, the

existing works are still based on the critical damage parameter (D_{cr}) from the smooth specimen, with the assumption that the D_{cr} value is independent of the stress triaxiality [82-86]. Validity of this assumption is investigated in this study, through examining the influence of stress triaxiality and loading mode (tensile fracture versus indentation compression) on the damage evolution [94, 96, 181, 229] and the D_{cr} value [179, 230-232], respectively. Figure 5.1 shows the overall approach used in this investigation. In view of the stress-triaxiality-dependent ductile damage model described in Chapter 4, the damage parameters for the smooth, short-gauge, and at the crack tip of SENB specimens can be determined. Meanwhile, indentation test is also performed to characterize the damage evolution under indentation. The critical contact depth, h_c^*, is determined from the product of the D_{cr} value at the crack tip and an adjusting parameter κ. The latter is considered to differentiate the potential difference of the D_{cr} value between tensile fracture and indentation compression. Once the h_c^* value is determined, the specific indentation energy, w_{Ind}, and the corresponding K_{Ind} are determined. Based on the above approach, this chapter is divided into three parts.

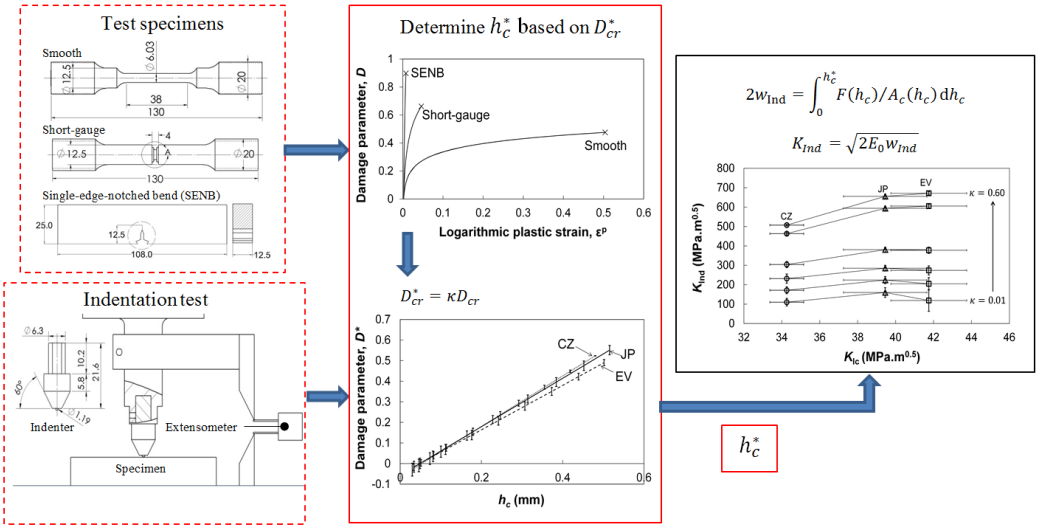

Figure 5.1 The overall approach to determine the critical contact depth, h_c^*, based on the critical damage parameter at the crack tip for calculating the indentation fracture toughness, K_{Ind}

The first part of this chapter is to establish locus of plastic fracture strain versus stress triaxiality. In addition to the two types of notch-free (named smooth and short-gauge) specimens, this part of study also includes two types of round-notched specimens with different notch radii, to ensure the accuracy of the established fracture locus.

The second part of the chapter is concerned about the effect of stress triaxiality on damage evolution, specifically, to evaluate applicability of a stress-triaxiality-dependent ductile damage model for predicting damage evolution in rail steels. This part of study is based on results from the two types of notch-free specimens, using cyclic loading-unloading tensile tests to determine their damage evolution. By extrapolating results from the above two parts of the study to the stress triaxiality level at the crack tip of the pre-cracked single-edge-notched bend (SENB) specimen, the equivalent plastic fracture strain and damage evolution at the crack tip are determined. This leads to the determination of the D_{cr} at the crack tip.

The last part of this chapter presents results from the cyclic loading-unloading ball indentation test, based on which damage evolution under indentation is established, but as a function of the contact depth rather than the equivalent plastic strain that is used for the tensile loading. The critical contact depth for calculating the K_{Ind} value is based on the critical damage parameter for indentation compression (D_{cr}^{*}). This D_{cr}^{*} value is equivalent to the product of D_{cr} at the crack tip and an adjusting parameter κ which is used to reconcile the potentially different critical damage parameters between the tensile fracture and the indentation compression. In addition, K_{Ind} is also determined based on the D_{cr} value for smooth specimens, denoted as the conventional indentation fracture toughness ($K_{\mathrm{Ind,con}}$). In this study, both K_{Ind} and $K_{\mathrm{Ind,con}}$ are compared with the experimentally measured K_{Ic} values for the three rail steels.

5.2 Theoretical background

5.2.1 Indentation fracture toughness

In fracture mechanics, the mode I critical stress intensity factor (K_{Ic}) can be expressed in terms of the specific fracture energy (w_f) [26, 28, 233, 234], as depicted in the following expressions:

$$K_{\mathrm{Ic}} = \sqrt{2E_0 w_f} \tag{5.1}$$

where E_0 is the Young's modulus.

In view that the magnitude of stress triaxiality under the indenter tip is similar to that at the crack tip, specific indentation energy to a critical contact depth, $2w_{Ind}$, is postulated to be correlated to $2w_f$ [80, 82], as expressed below.

$$2w_f \propto 2w_{\mathrm{Ind}} = \int_0^{h_c^*} F(h_c)/A_c(h_c)\,\mathrm{d}h_c \tag{5.2}$$

where, h_c^* is the critical value of contact depth h_c, representing the fictitious fracture initiation point under indentation for the ductile material. $F(h_c)$ is the applied indentation load as a function of h_c, and the projective area of indentation, $A_c(h_c)$, with ball indenter expressed as [82]

$$A_c(h_c) = \pi(2Rh_c - h_c^2) \tag{5.3}$$

Note that the h_c value is evaluated by analyzing the indentation unloading curve, with the consideration of the indenter geometry and elastic deflection. As well, for the ductile material, the pile-up effect needs to be included to determine the h_c value accurately [203, 205, 211, 212]. That is,

$$h_c = h_{pile} + h_{max} - \epsilon \frac{F_{max}}{S(h_{max})} \quad (5.4)$$

where h_{pile} is the height of the pile-up, h_{max} and F_{max} the maximum values of the contact depth (without the consideration of the pile-up) and indentation load, respectively, ϵ a constant which is set to be 0.75 for a ball indenter tip [203], and $S(h_{max})$ the contact stiffness at h_{max}, defined using the slope of the unloading curve [203].

After using the w_{Ind} value for w_f in Eq. (5.1), K_{Ic} from Eq. (5.1) represents K_{Ind} which is considered as an alternative factor for estimating the fracture toughness of ductile material [80-88]. That is,

$$K_{Ind} = \sqrt{2E_0 w_{Ind}} \quad (5.5)$$

5.2.2 Determination of critical contact depth

The critical contact depth, h_c^*, is essential for calculating K_{Ind}, which is determined based on the basic concept of CDM [127],

$$D = 1 - E/E_0 \quad (5.6)$$

where D is the damage parameter, defined based on the concept of effective stress and hypothesis of strain equivalence [127], and E elastic modulus of damaged material.

Lee et al. [82] proposed to use the measured elastic modulus, E^*, from the unloading curve of the indentation test to replace the E in Eq. (5.6), and thus establish variation of damage parameter with increase of h_c. According to Lee et al.'s work, the elastic modulus under indentation was calculated based on Hertzian contact law [201] and Sneddon's elastic punch theory [202], as shown in Eq. (5.7) [82-86].

$$E^* = \frac{1-v^2}{\left(\frac{1}{E_{\text{eff}}}-\frac{1-v_i^2}{E_i}\right)} = \frac{1-v^2}{\left(2C_s\sqrt{2Rh_c-h_c^2}-\frac{1-v_i^2}{E_i}\right)} \tag{5.7}$$

where v and v_i are Poisson's ratios of specimen and indenter, respectively, E_{eff} the effective modulus between specimen and indenter, E_i the Young's modulus of indenter, R the radius of ball indenter, and C_s the specimen compliance which is the difference between the total compliance (C) and the load frame compliance (C_f):

$$C_s = C - C_f \tag{5.8}$$

The detailed procedure to calibrate C_f for our indentation system is illustrated in the Appendix. Therefore, by substituting E^* from Eq. (5.7) to Eq. (5.6), the relationship between damage parameter and h_c is given below.

$$D^* = 1 - \frac{1-v^2}{\left(2C_s\sqrt{2Rh_c-h_c^2}-\frac{1-v_i^2}{E_i}\right)E_0} \tag{5.9}$$

where D^* is damage parameter under indentation.

For a critical D^* value, D_{cr}^*, the corresponding critical h_c value, h_c^*, can be determined from Eq. (5.9). In the past, D_{cr}^* value was assumed to be independent of stress triaxiality and equal to D_{cr} measured from the cyclic loading-unloading tensile test of the smooth specimens [82-86]. In the present study, however, D_{cr}^* value is determined using the following approach, with the consideration of the influences of stress triaxiality [94, 96, 181, 229] and loading mode [179, 230, 231] (specifically, between tensile fracture at the crack tip and indentation compression) on the damage development.

First of all, damage development in two types of notch-free (smooth and short-gauge) specimens is established using cyclic loading-unloading tensile tests, based on which a stress-triaxiality-dependent ductile damage model, proposed by Bonora [181], is calibrated for the three high-strength rail steels used in this study. Original form of the Bonora's ductile damage model that expresses D as a function of stress triaxiality (η) and equivalent plastic strain (ε_{eq}^{p}) [181] is

$$D = D_0 + (\overline{D} - D_0)\left\{1 - [1 - \frac{\ln \varepsilon_{eq}^{p} - \ln \varepsilon_{th}}{\ln \varepsilon_{p}^{f} - \ln \varepsilon_{th}} f(\eta)]^{\lambda}\right\} \tag{5.10}$$

where D_0 is the initial damage in the material before the test, $\overline{D}$ a material constant that represents the critical amount of damage in the smooth specimen if fracture occurs under uniform deformation, ε_{p}^{f} the plastic fracture strain measured experimentally for the smooth specimen, ε_{th} the threshold plastic strain for damage initiation assumed to be independent of η, λ is the damage exponent characteristic of the material, and $f(\eta)$ defined as [127]:

$$f(\eta) = \frac{2}{3}(1 + v) + 3(1 - 2v)(\eta)^2 \tag{5.11}$$

In order to take into account the loading history, η value is calculated based on the concept of average stress triaxiality (η_{av}) as [130]:

$$\eta_{av} = \frac{1}{\varepsilon_{eq,max}^{p}} \int_0^{\varepsilon_{eq,max}^{p}} \eta(\varepsilon_{eq}^{p}) d\varepsilon_{eq}^{p} \tag{5.12}$$

where $\eta(\varepsilon_{eq}^{p})$ and $\varepsilon_{eq,max}^{p}$ are the stress triaxiality, as a function of ε_{eq}^{p}, and the maximum value of ε_{eq}^{p}, respectively, both determined from an element of a FE model which has the maximum η value when the simulation reaches the critical deformation level for fracture initiation in the testing. In the rest of this chapter,

η_{av} is used to replace η in Eq. (5.10) so that the expression considers the possible influence of loading history on the damage development.

Since all rail steels used in the current study are in the pristine condition D_0 is chosen to be 0 (i.e., no damage before the test). Using Eq. (5.6) for the relationship between D and E, Eq. (5.10) can be converted to an expression that depicts the deterioration of E in a deformation process. That is,

$$E = [1 - \overline{D}\left\{1 - [1 - \frac{\ln \varepsilon_{eq}^{p} - \ln \varepsilon_{th}}{\ln \varepsilon_{p}^{f} - \ln \varepsilon_{th}} f(\eta_{av})]^{\lambda}\right\}]E_0 \tag{5.13}$$

In the above expression, value of ε_{th} is assumed to be the yield strain of 0.002, E_0 and ε_p^f determined from the experimental testing of the smooth specimen, η_{av} calculated using Eq. (5.12) based on the η value determined from FE modelling, and $\overline{D}$ and λ are the two variables that need to be identified for the three rail steels based on the deterioration of E determined for the cyclic loading-unloading tensile tests of the smooth and short-gauge specimens.

Once values of $\overline{D}$ and λ are determined, Eq. (5.13) is used to predict deterioration of E at the crack tip and the corresponding critical value of E at the crack initiation, which can be further converted to damage evolution and D_{cr}, respectively. To this end, both the equivalent plastic fracture strain ($\varepsilon_{eq,f}^{p}$) and η_{av} at the crack tip are required. In this study, the latter is determined from a FE model of the pre-cracked SENB specimen, and the former based on an extrapolation of the $\varepsilon_{eq,f}^{p}$ values from tensile tests for various η_{av} values to the η_{av} value at the crack tip.

In view that the stress triaxiality under the indenter tip is similar to that at the crack tip [82, 87], the D_{cr} value at the crack tip should be used to determine the critical h_c value (i.e., h_c^*) in Eq. (5.9), rather than using the D_{cr} value from smooth specimens. In addition, since different loading modes are introduced by tension

and indentation, parameter κ is introduced to adjust D_{cr} value used in indentation, to take into account the possible effect of loading mode on the D_{cr} value. That is,

$$D_{cr}^{*} = \kappa D_{cr} \tag{5.14}$$

where D_{cr}^{*} is the critical damage parameter under indentation loading, which is determined by adjusting D_{cr} at the crack tip using κ. Using the above D_{cr}^{*} value, h_c^{*} value for the indentation loading can be determined from Eq. (5.9), and applied to Eq. (5.2) to calculate w_{Ind} and then Eq. (5.5) for K_{Ind}. Note that this study uses strain-equivalent damage concept between tension and indentation. Since damage evolution in compression is expected to be slower than that in tension [179, 231, 232], κ value should between 0 and 1. Six different κ values, from 0.01 to 0.6, are used to calculate D_{cr}^{*} in the study to examine the possible influence of κ on the relationship between K_{Ind} and K_{Ic}. In addition, $K_{\mathrm{Ind,con}}$ based on the D_{cr} value from smooth specimens is also calculated for comparison.

5.3 Experimental and numerical methodologies

5.3.1 Materials

Three types of high-strength rail steels, JAPAN NSC FHH (JP), EVRAZ RMSM FHH (EV), and CZECH TZ IH (CZ), supplied by the Canadian National Railway Company (CN), were used in the test program. Detailed characterization of mechanical properties and constitutive equations for the three rail steels can be found in Tables 3.1 and 3.2, respectively. Note that all tests in this chapter were performed at room temperature only.

5.3.2 Experimental details

A test program, including tensile, SENB and indentation tests, was conducted for the three types of high-strength rail steels at room temperature. All specimens were prepared from the railhead region. An Instron 222 kN hydraulic universal testing machine was used to conduct the monotonic tensile, loading-unloading tensile, and SENB tests. A MTS 44 kN hydraulic testing system was used for the indentation test.

As shown in Figure 5.2, four types of axisymmetric tensile (two notch-free and two round-notched) specimens are designed for the monotonic tensile test to establish locus of equivalent plastic fracture strain versus average stress triaxiality. Three identical tests were conducted for each type of tensile specimens at an initial strain rate of 2.36×10^{-4} /s. For the smooth specimen, Figure 5.2(a), both axial and diametric extensometers were placed in the middle of the gauge section to measure simultaneously the elongation and diameter changes. For the other types of specimens in Figure 5.2, i.e., short-gauge, notch type I (NTI) and notch type II (NTII), due to the short gauge section, strain was calculated based on measurement from a diametric extensometer, placed in the middle of the gauge section. Based on the assumption of uniform stress and strain distributions in the gauge section and negligible volume change during the deformation, the true stress (σ) and logarithmic strain (ε) are calculated using the equations below:

$$\sigma = L/A \tag{5.15}$$

$$\varepsilon = \ln(A_0/A) \tag{5.16}$$

where L is the tensile load, A_0 the original cross-sectional area, and A the corresponding cross-sectional area measured during the test.

Loading-unloading tensile tests were conducted on the two notch-free (smooth and short-gauge) specimens for the three rail steels to characterize their damage

parameters. Note that the smooth specimen used in the loading-unloading tensile test had a 2% taper introduced in the middle of the reduced gauge section, to ensure the occurrence of neck formation and specimen fracture at the middle of gauge section. Because of the 2% tapering in the gauge section, strain was determined purely based on measurement from the diametric extensometer. The initial strain rate introduced to specimens in the loading-unloading tensile test was the same as that used in the monotonic tensile test. Condition to trigger the unloading phase was based on the load increment of 2 kN before reaching the UTS, but after UTS based on the increment of displacement by 0.25 mm which corresponded to a loading period of 30 seconds. For the short-gauge specimen, since fracture occurred before UTS, only load control was performed in the cyclic loading-unloading tensile tests, with the same load increment of 2 kN.

The K_{Ind} for the three rail steels is determined from the indentation test using a home-made indentation system for which the schematic drawing is illustrated in Figure 5.3(a). The indentation load was recorded using a MTS load cell with a resolution of 0.0001 N, and the depth measured by a clip-on extensometer with a resolution of 3 μm. The indenter shown in Figure 5.3(a) is made of O1 tool steel with proper heat treatment and a tungsten carbide ball (1.19 mm in diameter, E_{i} of 480GPa, ν_{i} of 0.28), compression fit into the pre-machined semi-spherical cavity at the bottom of the indenter. The indentation system was first calibrated using a standard testing block to regenerate its hardness and Young's modulus values, based on which the load frame compliance (C_f) was determined. Details of the procedure are given in the Appendix. Note that in addition to C_f, the amount of pile-up (h_{pile}) around the indenter was also quantified to characterize the deterioration of E^* under indentation.

Specimens for the indentation tests were 10 mm thick and polished gradually to a mirror-like finish using an alpha alumina polishing powder of 0.05μm at final polishing step. Values for h_{pile} were directly measured using a digital optical

microscope with magnification of 320X and a digital dial indicator with a resolution of 2.54 μm. Details of the procedure are depicted as follows.

Firstly, the original, flat specimen surface near the indent was focused under the microscope and its vertical position, recorded by the digital dial indicator, used as the reference. Then, the pile-up region located at the edge of indent was focused and change of the reading from the indicator represented the h_{pile} value. Around each indent, five measurements were taken and the average value used as the height of the pile-up.

Figure 5.3(b) illustrates one cycle of the loading-unloading indentation test for the JP rail steel. The unloading curve is best fitted using a power law function, $F = B\left(h - h_f\right)^m$, where B and m are two adjusting parameters for which the values are determined using the least square fitting method. After that, the contact stiffness, $S = dF/dh$, is determined at h_{max} [203]. The indentation tests were performed at ten different depths (0.04, 0.06, 0.09, 0.12, 0.18, 0.24, 0.3, 0.36, 0.42, and 0.48 mm) with a constant indentation speed of 0.1 mm/min in each loading-unloading cycle and five tests were conducted at each specified depth.

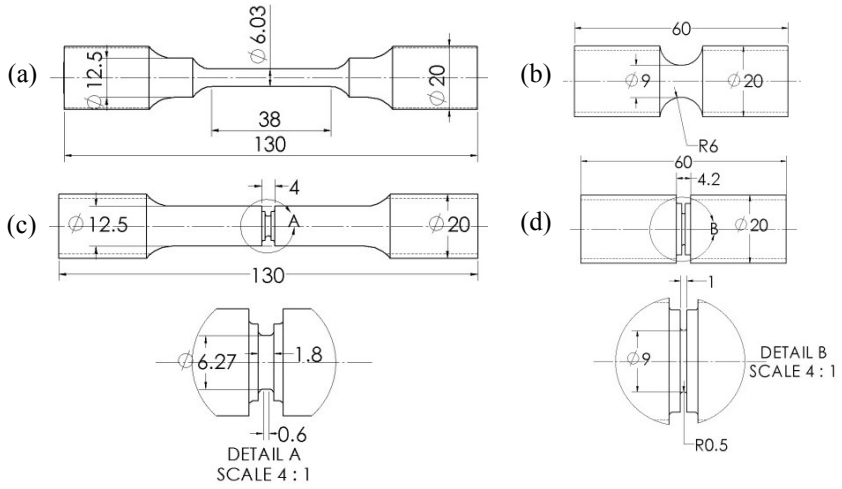

Figure 5.2 Dimensions and geometries of four types of axisymmetric tensile specimens: (a) smooth specimen, (b) notch type I (NTI) specimen, (c) short-gauge specimen, and (d) notch type II (NTII) specimen

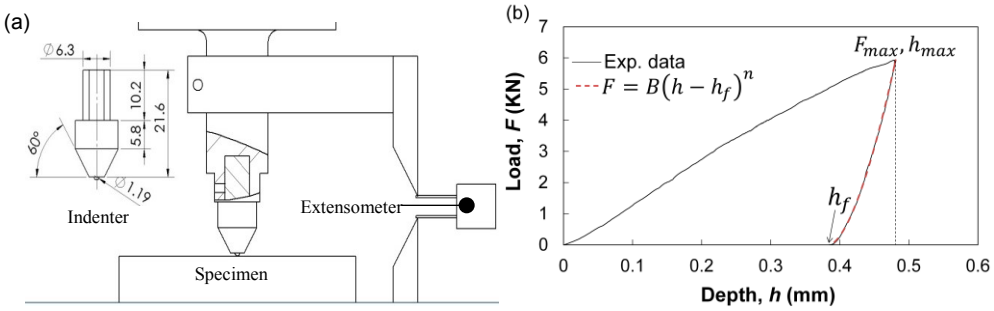

Figure 5.3 Indentation test: (a) schematic presentation of the test set-ups and ball indenter and (b) a typical indentation loading-unloading curve (for JP rail steel)

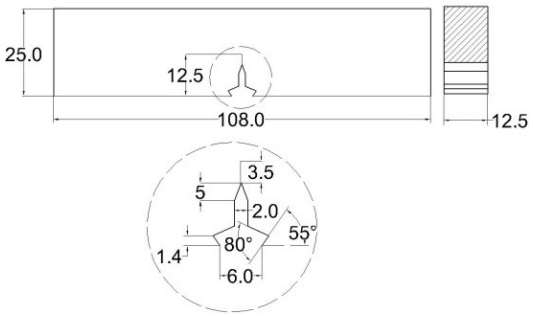

Figure 5.4 Dimensions of the SENB specimen for the standard fracture toughness test

For the purpose of validating $K_{Ind,}$ the SENB test was conducted according to ASTM E399 [18] to measure K_{Ic} for the three rail steels. Dimensions of the SENB specimens are shown in Figure 5.4. The SENB specimen was first pre-cracked using fatigue testing by setting initial values of the maximum stress intensity factor ($K_{max)}$ and the minimum stress intensity factor (K_{min}) to be 14 and 5 MPa.m$^{0.5}$, respectively, until crack grew for a length in the range of 3 to 3.5 mm, and then the specimens were tested at a crosshead speed of 2×10^{-3} mm/s. The crack mouth opening displacement (CMOD) was measured using the same clip-on extensometer, mounted to the mouth of the notch before each test. Details of the SENB test for the fracture toughness measurement are given in the chapters 2 and 3.

5.3.3 Finite element modelling

Finite element (FE) modelling of monotonic tensile, loading-unloading tensile, and SENB tests was carried out using ABAQUS standard 6.13. The constitutive model is based on the J_2 plasticity theory, with material constants in Table 5.1, was used as material input data. The quadrilateral 8-node element with reduced Gauss integration was used in discretization for all types of specimens. The FE models were shown for the JP rail steel only. The same procedure was also applied to the other two rail steels (EV and CZ).

As shown in Figure 5.5, axisymmetric FE models are built for the four types of tensile specimens, following the dimensions given in Figure 5.2. Figure 5.5(a) depicts the FE model of the smooth specimen, with 6,392 axisymmetric stress elements and 20,173 nodes, Figure 5.5(b) the NTI specimen with 5,509 axisymmetric stress elements and 16,878 nodes, Figure 5.5(c) the short-gauge specimen with 4,930 axisymmetric stress elements and 15,119 nodes, and Figure 5.5(d) the NTII specimen with 3,757 axisymmetric stress elements and 11,556 nodes. The boundary conditions for the four types of tensile specimens were set to be the same as that applied in the testing, i.e., with one end fixed and the other end moving at a specified displacement rate.

FE modelling of the two notch-free (smooth and short-gauge) specimens subjected to the loading-unloading tensile test was also performed. It should be noted that the FE model of the smooth specimen in the loading-unloading tensile test had a 2% taper in the middle of reduced gauge section to reflect the physical taper introduced to the smooth specimen. Both FE models had one end completely constrained from any movement, while the other end subjected to a displacement-controlled cyclic loading.

As shown in Figure 5.6, a symmetric 2-dimensional (2D) FE model is established for the SENB specimen, which has dimensions same as those specified in Figure 5.4. The contact pins were modelled as analytical rigid bodies and the SENB specimen a deformable body meshed with 29,155 plane-strain

elements and 88,200 nodes. The contact surface was placed between the contact pins and the SENB specimen in the conditions of small sliding, “hard” normal contact and tangential friction. The boundary conditions were set to be the same as those for the testing, i.e., with the bottom pin fixed and the top pin moving down at a specified displacement rate. The notch tip was mimicked using a circular profile with an initial radius of 0.1 μm, which is determined based on the strip yield model [150]. In order to capture the large stress and strain gradients around the notch tip, the quarter circular arc in the right figure of Figure 5.6 was divided into 18 sections. Such division was repeated in the radial direction around the notch tip, to generate 100 layers of fan elements in the radial direction.

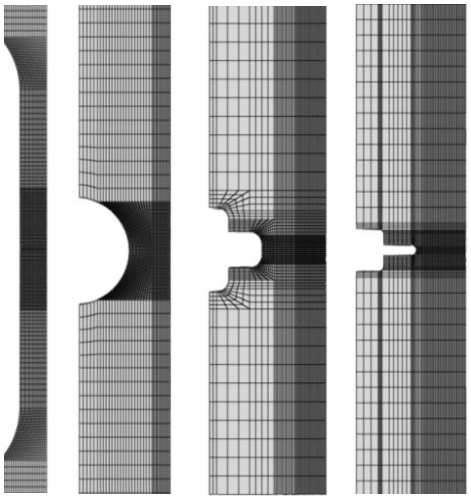

Figure 5.5 FE models of (a) smooth, (b) NTI, (c) short-gauge, and (d) NTII specimens

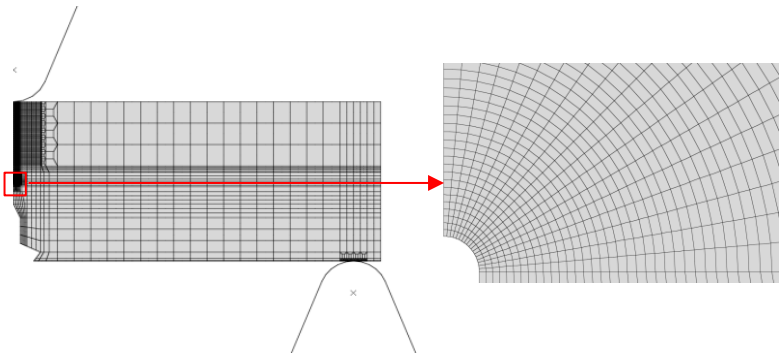

Figure 5.6 FE model for the SENB specimen (left) and details of the mesh pattern at the notch tip (right)

5.4 Results

5.4.1 Locus of fracture strain versus stress triaxiality

In this section, locus of equivalent plastic fracture strain versus average stress triaxiality for each of the three rail steels is established using the four types of tensile specimens. Diameter of the minimum cross-section of the post-test tensile specimen is measured to calculate the equivalent plastic fracture strain using Eq. (5.16). The FE modelling is used to determine the variation of the stress triaxiality during deformation. The average stress triaxiality value, calculated using Eq. (5.12) based on the output from a selected element in the corresponding FE model, as to be specified later, is used to represent the stress triaxiality for a given specimen geometry.

Figure 5.7 presents both the experimentally determined monotonic true stress-logarithmic strain curves (in solid lines) and the corresponding curves generated from the FE models (in dash lines) for the four types of tensile specimens of the three rail steels. The experimental results indicate that by reducing the gauge length from 38 to 1 mm, i.e., from smooth to NTII specimen, the fracture strains for all of the three rail steels are reduced dramatically. This is due to the well-known stress triaxiality effect on the fracture strain [44]. It should be noted that

although the four types of tensile specimens give the same order of fracture strain among the three rail steels, difference of the fracture strain values among the three rail steels is reduced by increasing the stress triaxiality. That is, fracture strain for the JP rail steel is reduced from 0.5 to 0.022, for the EV rail steel from 0.3 to 0.016, and for the CZ rail steel from 0.18 to 0.012. On the other hand, in view of good agreement between simulation and experimental results, shown in Figure 5.7, distributions of stress triaxiality for the four types of tensile specimens are obtained from the FE modelling of tensile specimens.

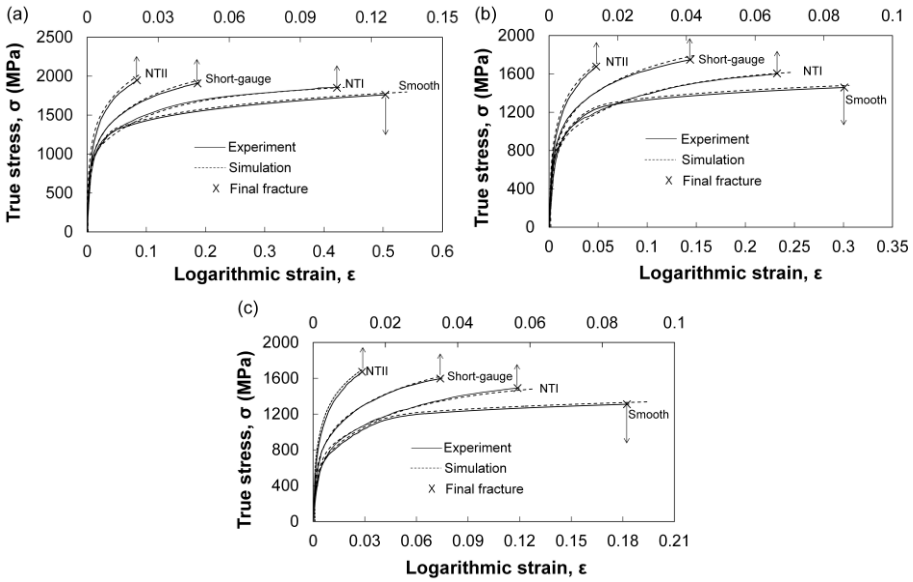

Figure 5.7 Comparison of experimental and numerical true stress-logarithmic strain curves of four types of tensile specimens for (a) JP, (b) EV, and (c) CZ rail steels

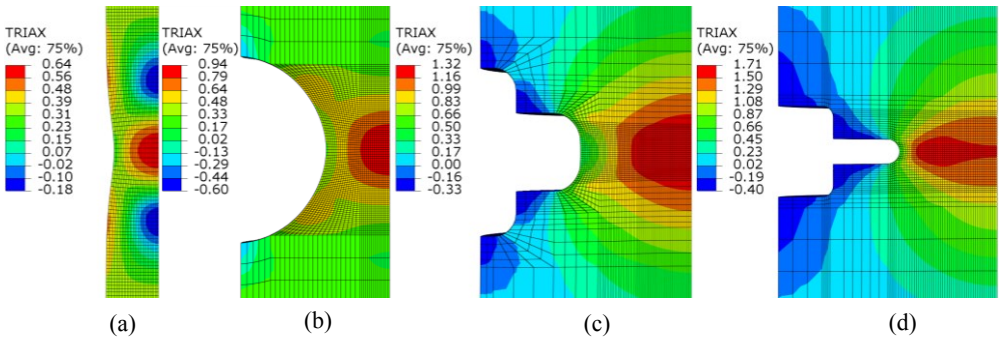

Figure 5.8 Contour plots of stress triaxiality at the onset of fracture for (a) smooth, (b) NTI, (c) short-gauge, and (d) NTII specimens of JP rail steel

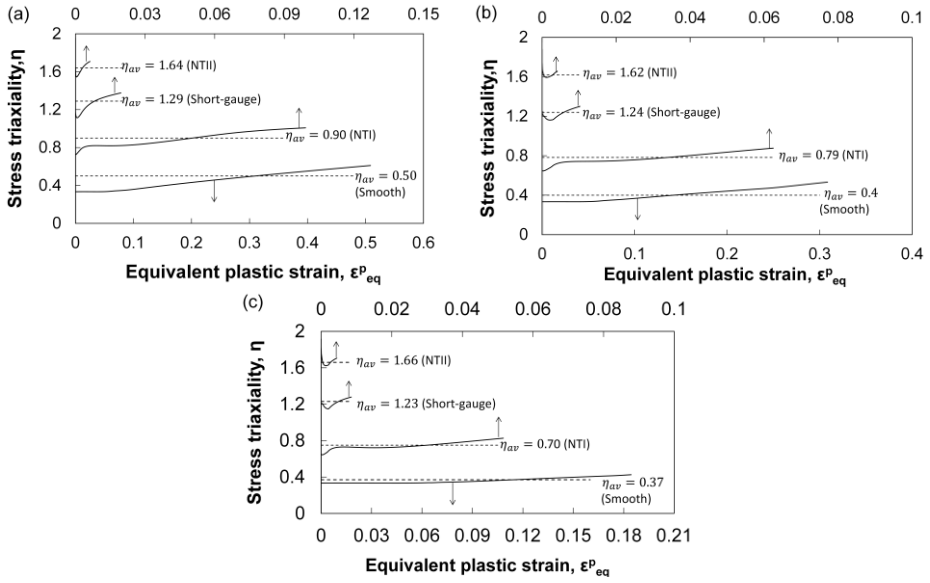

Figure 5.9 Evolution of stress triaxiality and its average value in an element of FE modelling of four types of tensile specimens that has the maximum stress triaxiality at fracture initiation for: (a) JP, (b) EV, and (c) CZ rail steels

Figure 5.8 presents contours of stress triaxiality for the four types of tensile specimens of the JP rail steel, right before the onset of fracture. As shown in Figures 5.8(a), 5.8(b), and 5.8(c) for smooth, NTI, and short-gauge specimens, respectively, the maximum stress triaxiality occurs at the centre of the minimum

cross-section. While for the NTII specimen, as shown in Figure 5.8(d), its maximum stress triaxiality occurs along a ring band that is closer to the circumference than to the centre of the cross-section. Note that the same phenomena as those shown in Figure 5.8 also occur for the other two rail steels.

Figure 5.9 presents variations of stress triaxiality as a function of equivalent plastic strain among the four types of tensile specimens for the three rail steels. Each of the curves is determined from an element in the FE model which yields the maximum stress triaxiality at the onset of fracture. As expected, magnitude of stress triaxiality increases with the decrease of gauge length. Their average values are also calculated for all the cases considered in the study using Eq. (5.12), as indicated using the horizontal dash lines in Figure 5.9.

As shown in Figure 5.10, fracture loci of equivalent plastic fracture strain ($\varepsilon_{eq,f}^{p}$) versus average stress triaxiality (η_{av}) for the three rail steels are established using the four types of tensile specimens. The experimental data of $\varepsilon_{eq,f}^{p}$ versus η_{av} are best fitted using two power-law functions, one suggested by Bao and Wierzbicki [130] and the other a modified version of Bonora's model [181]. The fitting suggests that the former gives a better agreement with the experimental data than the latter. Consequently, $\varepsilon_{eq,f}^{p}$ of the pre-cracked SENB specimen for the three rail steels are extrapolated from the fracture loci shown by the solid lines in Figure 5.10 to the η_{av} value at the crack tip.

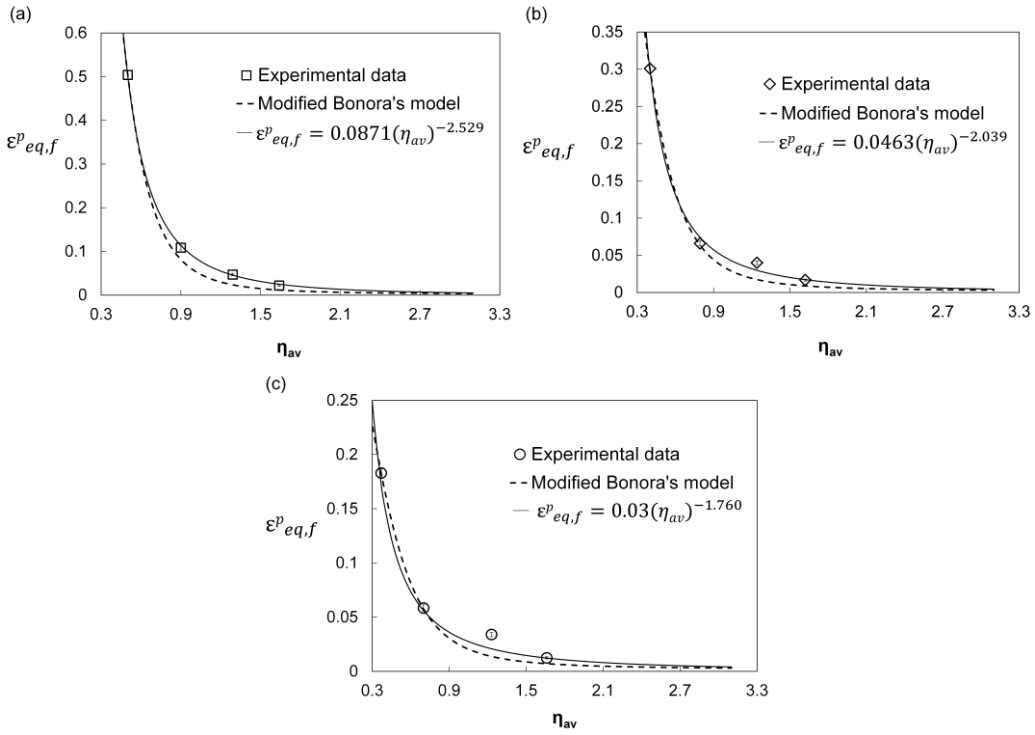

Figure 5.10 Dependence of equivalent plastic fracture strain ($\varepsilon^p_{eq,f}$) on average stress triaxiality (η_{av}) for (a) JP, (b) EV, and (c) CZ rail steels

The η_{av} value at the crack tip is determined using the FE model of the pre-cracked SENB specimen. Firstly, as illustrated in Figure 5.11 for the JP rail steel, the linear portion of the experimental data, up to the first apparent pop-in, is mimicked by the simulation, where the tangential friction coefficient at the contact with the pin is set to be 0.35. Figure 5.12 presents the distribution of stress triaxiality at the moment when the simulation reaches the first apparent pop-in of the JP rail steel. It is shown that the maximum stress triaxiality is located ahead of the crack tip along the crack growth path. Note that the same phenomenon exists for the other two rail steels.

Figure 5.13 presents evolution of the stress triaxiality as a function of the equivalent plastic strain until crack initiation occurs (at the first apparent pop-in) for the three rail steels, based on output from an element ahead of the crack tip that has the maximum stress triaxiality. Value for η_{av} at the crack tip is calculated

using Eq. (5.12) for each of the three rail steels, and labelled as dash horizontal lines in Figure 5.13. Note that difference of the η_{av} values at the crack tip of the SENB specimens of the three rail steels is attributed to the difference of the strain-hardening in the three rail steels, for which the details have been discussed in the chapter 3.

Table 5.2 lists the estimated $\varepsilon_{eq,f}^{p}$ values for the pre-cracked SENB specimen of the three rail steels. It is shown that due to the increase of the stress triaxiality, the $\varepsilon_{eq,f}^{p}$ value of the pre-cracked SENB specimen is significantly reduced from that of the smooth specimen, but still in the same order of magnitude as that for the yield strain of the smooth specimen. The table also suggests that ranking of the fracture strain of the pre-cracked SENB specimen is the same as that of the four types of tensile specimens. That is, the JP rail steel always has the highest fracture strain and the CZ rail steel the lowest.

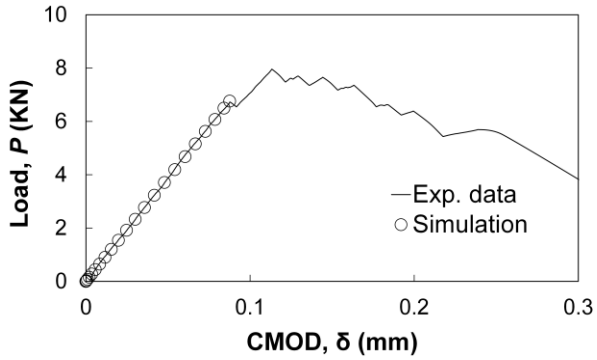

Figure 5.11 Comparison of linear portion of *P*-*δ* curves between experiment and simulation for the JP rail steel

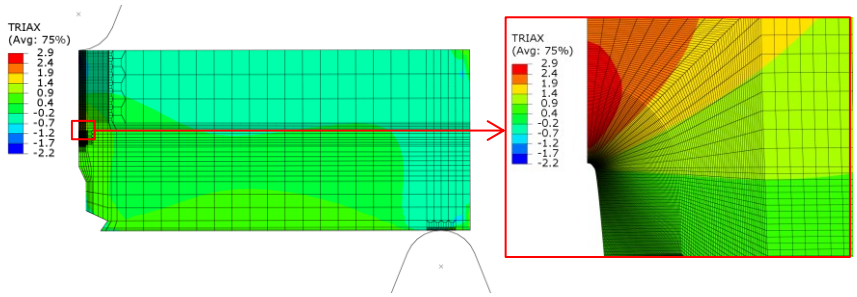

Figure 5.12 Distribution of stress triaxiality at the onset of fracture for the pre-cracked SENB specimen of the JP rail steel

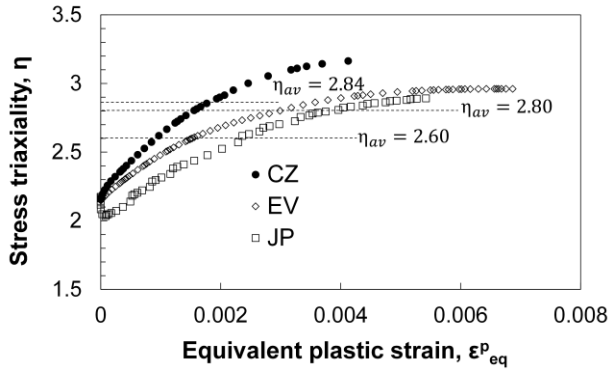

Figure 5.13 Evolution of stress triaxiality and the corresponding average stress triaxiality values for the three rail steels, based on stress triaxiality evolution in an element that is located ahead of the crack tip with the maximum stress triaxiality

Table 5.1 Plastic fracture strain of the pre-cracked SENB specimen for the three rail steels

Parameters	Rails		
	JP	EV	CZ
η_{av}	2.60	2.80	2.84
$\varepsilon_{eq,f}^{p}$	0.0078	0.0057	0.0048

5.4.2 Stress triaxiality effect on critical damage parameter

In this section, damage measurement using the two types of notch-free (smooth and short-gauge) specimens is carried out to verify the validity of a ductile damage model for predicting damage evolution in the three rail steels.

Figure 5.14 compares experimental and numerical loading-unloading true stress-logarithmic strain curves of the two notch-free specimens for the JP rail steel. The experimental cyclic loading-unloading tensile test is conducted to determine damage evolution for the two notch-free specimens, based on the assumption that damage is uniformly distributed on the cross section. Following the classical approach [192], the unloading slope from the linear portion of the unloading part of the true stress-logarithmic strain curves is measured up to the fracture initiation. However, due to the triaxial stress state introduced, for the smooth specimen after the neck formation and for the short-gauge specimen from the beginning, the experimentally measured unloading slope is also influenced by the change in gauge section geometry. In view of this, numerical simulation of the loading-unloading tensile test is performed to correct the effect of gauge section geometry on the unloading slope for the smooth specimen, following the approach suggested by Celentano and Chaboche [193], and its slightly modified version, as described below, for the short-gauge specimen. With this correction, variation of the elastic modulus with plastic strain can then be determined to establish the damage evolution during the plastic deformation process.

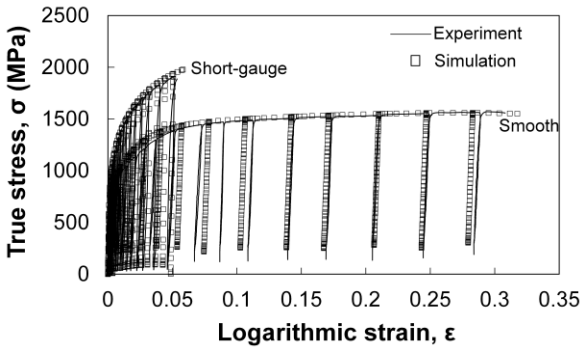

Figure 5.14 Experimental and numerical true stress-logarithmic strain curves from the loading-unloading smooth and short-tensile tests for JP rail steel

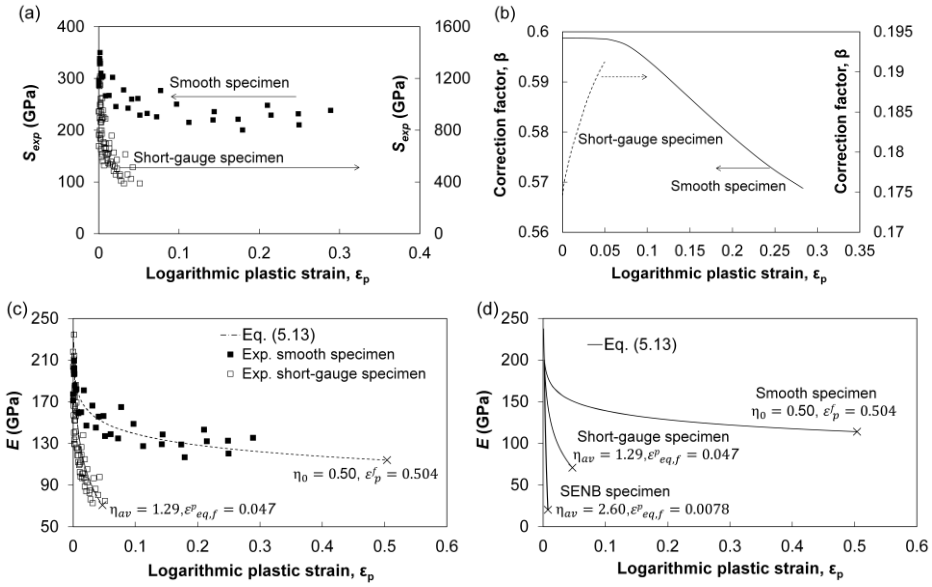

Figure 5.15 Depiction of the ductile damage model in Eq. (5.13) for smooth and short-gauge specimens of JP rail steel: (a) experimental unloading slope, S_{exp}, (b) correction factor, β, (c) change of elastic modulus, E, and (d) extrapolation of the measured E values to the stress triaxiality level at the crack tip of SENB specimen

Figure 5.15 illustrates the identification procedure for predicting damage evolution in the JP rail steel. Figure 5.15(a) shows variation of the unloading slope measured for the cyclic loading-unloading tensile tests of the smooth and short-gauge specimens for the JP rail steel. It can be seen that both types of the notch-free specimens show decrease in the unloading slope with the increase of logarithmic plastic strain (ε_p). However, due to the effect of triaxial stress state and Poisson's ratio, the unloading slope in Figure 5.15(a) does not represent the elastic modulus. Therefore, an additional procedure that uses a geometric correction factor (β), as described in ref. [193], is used to convert the unloading slope to the elastic modulus.

Figure 5.15(b) shows the variation of the geometric correction factor β, defined in Eq. (5.17a), as a function of logarithmic plastic strain (ε_p) for both types of notch-free specimens, following the approach proposed by Celentano and Chaboche [193].

$$\beta(\varepsilon_p) = \frac{E_0}{S_{FEM}} \tag{5.17a}$$

where E_0 is the input Young's modulus, and S_{FEM} the unloading slope in the loading-unloading true stress-logarithmic strain curves from the FE modelling of both smooth and short-gauge specimens. As expected, β value for the smooth specimen remains relatively constant when deformation in the gauge section is uniform, but after necking β value decreases with the increase of ε_p, which is consistent with that reported before [193]. While for the short-gauge specimen, it is found that β value increases monotonically from the beginning of deformation till fracture occurs.

Since FE models for both smooth and short-gauge specimens mimic closely the deformation behaviour observed from the experimental testing, as shown in Figure 5.14, variation of β versus ε_p should also be applicable to results from the experimental testing. That is,

$$\beta(\varepsilon_p) = \frac{E}{S_{exp}} \tag{5.17b}$$

where E is the elastic modulus of damaged material, and S_{exp} the measured unloading slope from the experimental testing. Therefore, variation of E with ε_p for the two types of notch-free specimens of the JP rail steel can be determined by multiplying β with S_{exp}, as shown in Figure 5.15(c), in which solid and open squares represent data for the smooth and short-gauge specimens, respectively. Figure 5.15(c) shows clearly that E for the short-gauge specimen degraded faster than that for the smooth specimen.

According to the data shown in Figure 5.15(c), validity of Eq. (5.13) for predicting damage evolution is demonstrated for the JP rail steel. The least-square-fitting method is first applied to the experimental data of the smooth

specimens. By setting $\varepsilon_{eq}^{p} = \varepsilon_{p}^{f}$ and η_{av} =1/3, Eq. (5.13) is reduced to Eq. (5.6), where $\overline{D}$ becomes the only unknown and thus can be uniquely determined using the linear least-square-fitting method. As $\overline{D}$ is a material constant, its value is kept unchanged once it is determined and is applied to the short-gauge specimen for which the η_{av} value in Eq. (5.13) for the JP rail steel is 1.29. In this case, λ is the only unknown in Eq. (5.13), and can be determined again using the linear least-square-fitting method to best fit the change of the elastic modulus with the increase of ε_p for the short-gauge specimen.

The above procedure is also applied to the other two rail steels, and the so-determined values for $\overline{D}$ and λ for the three rail steels are listed in Table 5.3. As shown in Table 5.3, λ is same for all of the three rail steels, but $\overline{D}$ is slightly different.

As Eq. (5.13) can well fit the experimental data of *E* versus ε_p for the two types of notch-free specimens by only changing the average stress triaxiality, Eq. (5.13) is to be a suitable ductile damage model to predict damage evolution of high-strength rail steels. As shown in Figure 5.15(d) for the JP rail steel, change of *E* at the crack tip of the pre-cracked SENB specimen, along with that for the smooth and short-gauge specimens, is plotted as a function of ε_p. The deterioration of *E* at the crack tip of the JP rail steel is predicted using Eq. (5.13), based on the corresponding values of η_{av} and $\varepsilon_{eq,f}^{p}$ in Table 5.2 and $\overline{D}$ and λ in Table 5.3. As shown in Figure 5.15(d), the deterioration rate of *E* increases with the increase of η_{av}, and the critical *E* value before the onset of fracture, i.e., at $\varepsilon_{eq,f}^{p}$, decreases with the increase of η_{av}. It should be pointed out that the phenomena presented in Figure 5.15 for the JP rail steel were also observed for the other two rail steels (EV and CZ).

Table 5.2 Parameters of $\overline{D}$ and λ in Eq. (5.13) for three rail steels

Parameters	Rails		
	JP	EV	CZ
$\overline{D}$	0.408	0.414	0.330
λ	1	1	1

According to Eq. (5.6), change of E can be converted to damage parameter, which is presented in Figure 5.16 for the smooth, short-gauge, and pre-cracked SENB specimens of the three rail steels. Figure 5.16(a) compares damage parameters for the smooth specimen of the three rail steels, which shows that the CZ rail steel is lowest in the damage evolution rate and has the smallest value for D_{cr}. On the other hand, the JP and EV rail steels show similar damage evolution rates, but due to the larger ε_p the former has about 10% higher D_{cr} value than the latter.

Figure 5.16(b) shows damage parameters in the short-gauge specimen of the three rail steels. Obviously, the increase of stress triaxiality from that generated in the smooth specimen to the short-gauge specimen has increased both the damage evolution rate and D_{cr}. Such phenomenon has been reported before, between smooth and circumferentially notched tensile specimens of aluminium 7449 [229]. Furthermore, for the short-gauge specimen, EV rail steel shows a faster damage evolution rate than the JP rail steel. Although $\varepsilon^{p}_{eq,f}$ of the EV rail steel is still slightly smaller than that of the JP rail steel, their D_{cr} values are similar. The CZ rail steel, on the other hand, still has the smallest damage evolution rate and critical damage parameter among the three rail steels.

Figure 5.16(c) presents damage parameters at the crack tip of the pre-cracked SENB specimen for the three rail steels. The figure suggests that with the further increase of stress triaxiality to that at the crack tip, the damage evolution rate is further increased for the three rail steels. The figure also suggests that D_{cr} values at the crack tip of the pre-cracked SENB specimen are almost twice as big as those for the smooth specimen.

Because of the difference in the damage evolution rates and $\varepsilon_{eq,f}^{p}$ values at the crack tip of the pre-cracked SENB specimen for the three rail steels, the latter shown in Table 5.2, D_{cr} values at the crack tip of the pre-cracked SENB specimens are similar between the EV and JP rail steels, and larger than that of the CZ rail steel.

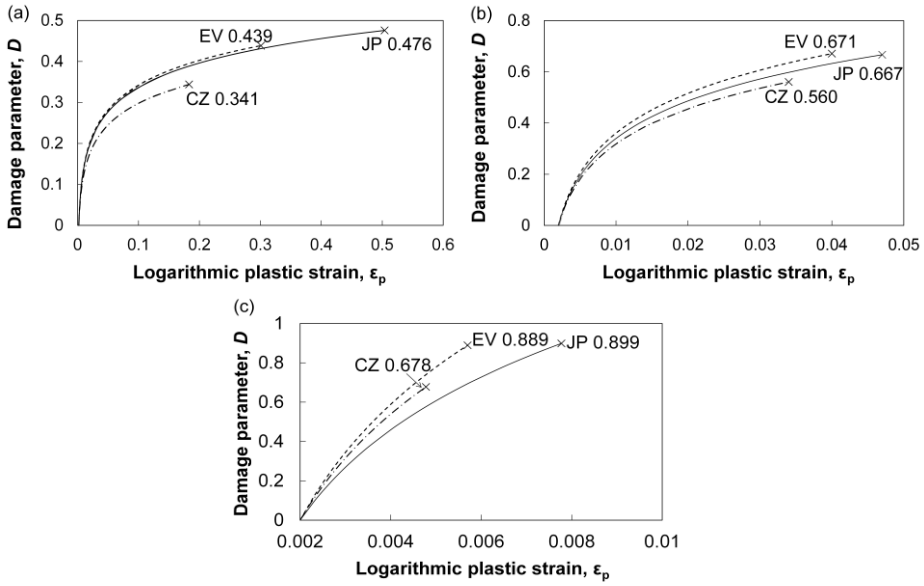

Figure 5.16 Damage parameter and D_{cr} values for (a) smooth, (b) short-gauge, and (c) at the crack tip of pre-cracked SENB specimens of the three rail steels

5.4.3 Indentation fracture toughness

In view of the above effect of stress triaxiality on the damage development, question is raised about the appropriateness of using $K_{\mathrm{Ind,con}}$, determined from indentation tests based on D_{cr} for the smooth specimens, to characterize fracture toughness that is traditionally based on K_{Ic} from the pre-cracked SENB specimens. Furthermore, D_{cr} value for the indentation compression might be different from that for tensile fracture. Therefore, in this section, D_{cr} values at the crack tip of pre-cracked SENB specimens are used to calculate K_{Ind}, with an

adjusting parameter κ introduced to reconcile the potential difference of D_{cr} between the different loading modes (tensile fracture and indentation compression). In addition, $K_{Ind,con}$ is also considered for the comparison. Validity of $K_{Ind,con}$ and K_{Ind} is examined by comparing their values with the experimentally measured K_{Ic} values.

5.4.3.1 Critical contact depth

Two variables are essential for determining the deterioration of E^* under indentation, i.e., h_c and C_s. Value for the h_c can be calculated using Eq. (5.4), and the corresponding C_s using Eq. (5.8). In order for the accuracy of h_c, the $h_{pile}$is measured and Figure 5.17 summarizes the h_{pile} values for the three rail steels as a function of h_{max}. The figure shows that h_{pile} has a small value at a small h_{max} and increases gradually with the increase of h_{max}. The figure also shows that h_{pile} is evolved in a slightly different way among the three rail steels. That is, the JP rail steel starts the earliest for developing h_{pile}, and its value is the largest at the given h_{max}. On the other hand, development of h_{pile} in the CZ rail steel is the latest, and its magnitude the smallest. Value for C_s is determined, as expressed in Eq. (5.8), by subtracting the load frame compliance, C_f, from the experimentally measured total compliance, C. The former has been calibrated using a standard Brinell hardness testing block, using a procedure described in the Appendix, and the latter is the inverse of contact stiffness determined using the Oliver-Pharr method [203].

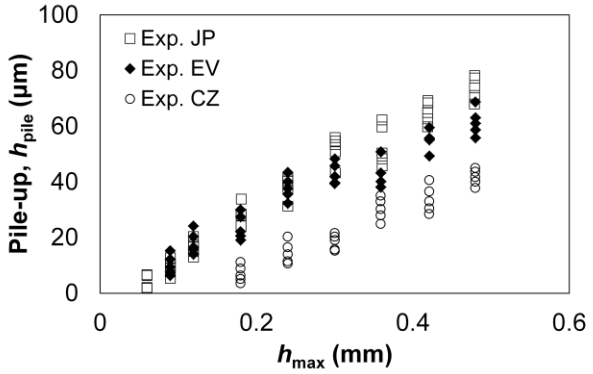

Figure 5.17 Variation of h_{pile} as a function of h_{max} for the three rail steels

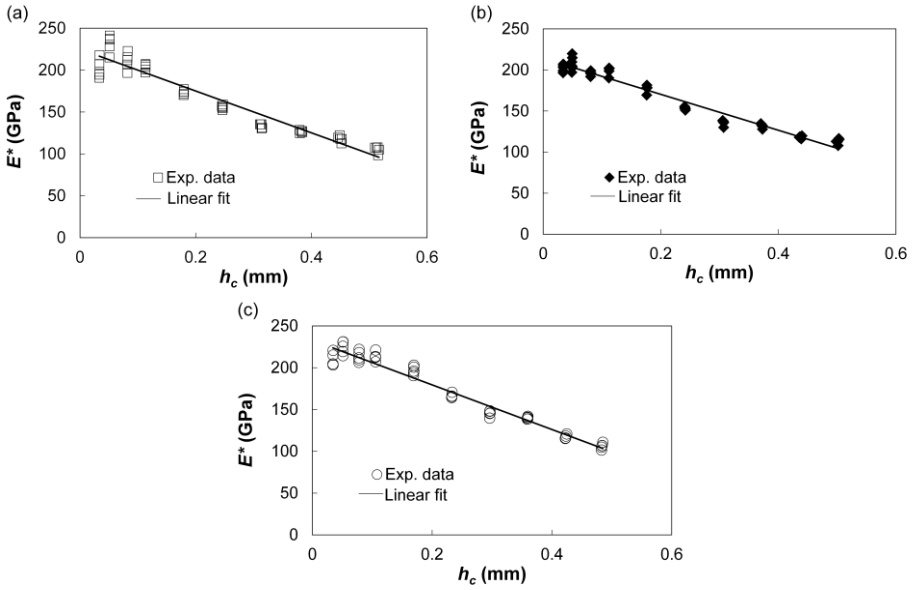

Figure 5.18 Variation of elastic modulus E^* in the ball indentation test for (a) JP, (b) EV, and (c) CZ rail steels

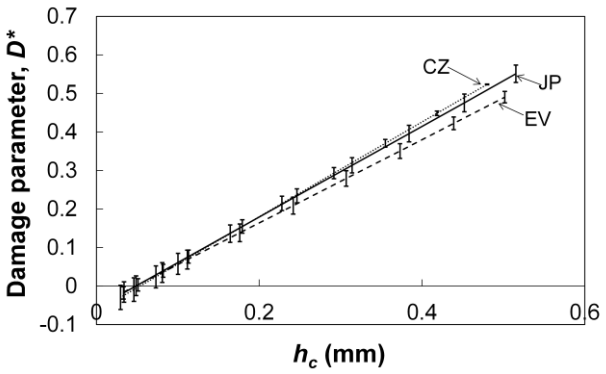

Figure 5.19 Damage development for the three rail steels under the ball indentation test

Table 5.3 Critical contact depth h_c^* for the given D_{cr}^* values

κ	JP rail steel			EV rail steel			CZ rail steel		
	D_{cr}^*	h_c^* (mm)		D_{cr}^*	h_c^* (mm)		D_{cr}^*	h_c^* (mm)	
		mean	STD		mean	STD		mean	STD
0.01	0.0090	0.0563	0.0139	0.0089	0.0563	0.0242	0.0068	0.0632	0.0242
0.05	0.0450	0.0867	0.0143	0.0445	0.0892	0.0235	0.0339	0.0844	0.0231
0.1	0.0899	0.1248	0.0146	0.0889	0.1304	0.0226	0.0678	0.1110	0.0216
0.2	0.1798	0.2004	0.0161	0.1778	0.2128	0.0209	0.1356	0.1641	0.0190
0.5	0.4495	0.4292	0.0179	0.4445	0.4599	0.0156	0.3390	0.3235	0.0106
0.6	0.5394	0.5053	0.0186	0.5334	0.5423	0.0139	0.4068	0.3767	0.0078

Based on values for h_c and C_s, E^* under indentation loading can be determined and are presented in Fig. 5.18 for the three rail steels. Data points in Fig. 5.18 are fitted using a linear function. By converting the so-determined E^* values to D^* using Eq. (5.6), damage evolution under ball indentation is presented as a function of h_c for the three rail steels, as depicted in Fig. 5.19. The figure suggests that under indentation, the EV rail steel has the lowest damage evolution rate and the CZ rail steel the fastest. Error bars on each curve represent the standard deviation of the experimental data at a given h_c value.

Critical indentation depth (h_c^*) for each of the three rail steels, which is needed for calculating K_{Ind}, can be determined using Fig. 5.19 based on D_{cr}^* values in Table 5.4. As mentioned earlier, a parameter κ is introduced to adjust D_{cr}^* values using D_{cr} values in Fig. 5.16(c), so that the possible difference of the critical

damage parameter between tensile loading and indentation compression is considered.

Table 5.4 summarizes six different D_{cr}^{*} values for each of the three rail steels by varying κ from 0.01 to 0.6, and the corresponding mean values and standard deviation of h_c^*. The table suggests that h_c^* for the EV rail steel is larger higher than that for the JP rail steel, and that h_c^* for the CZ rail steel is the smallest among the three rail steels (except at κ of 0.01). It should be noted that κ of 0.6 yields the maximum h_c^* values that can possibly be generated in the EV and JP rail steels using the ball indenter of 1.19mm in diameter.

5.4.3.2 Correlation of K_{Ind} and K_{Ic}

Using the above information, i.e. h_c^* listed in Table 5.4 and A_c expressed in Eq. (5.3), the specific indentation energy ($2w_{Ind}$) can be calculated from Eq. (5.2) using the curve of F versus h_c from the experimental testing. Thus, the corresponding K_{Ind} can be determined from Eq. (5.5). Fig. 5.20 depicts F as a function of h_c from the indentation tests for the three rail steels used in the study, fitted using the quadratic polynomial function. The corresponding K_{Ind} values are presented in Fig. 5.21. In addition, $2w_{Ind}$ was also calculated using h_c^* determined from Fig. 5.19 based on the D_{cr} values given in Fig. 5.16(a). The corresponding K_{Ind} values are denoted as $K_{\text{Ind,con}}$, representing the K_{Ind} values from the conventional approach that is based on the D_{cr} values from the smooth specimens.

As shown in Fig. 5.21, K_{Ind} values are estimated for each of the six κ values, all of which have larger magnitude than that for K_{Ic}. Note that the figure contains scattering bars for both K_{Ind} and K_{Ic}, but scattering of K_{Ind} for $\kappa \geq 0.2$ is so small that it is actually buried by the markers for the average value. All of the six K_{Ind} values in the figure suggest that the CZ rail steel should have the smallest fracture toughness among the three rail steels. Although there seems to be a transition in the ranking of K_{Ind} between the EV and JP rail steels when κ increases from 0.2 to

0.6, the difference of K_{Ind} values is within the scattering of data. A similar phenomenon exists for K_{Ic} for the two rail steels. That is, difference of K_{Ic} between the EV and JP rail steels has a size similar to that of the scattering bar for their data points.

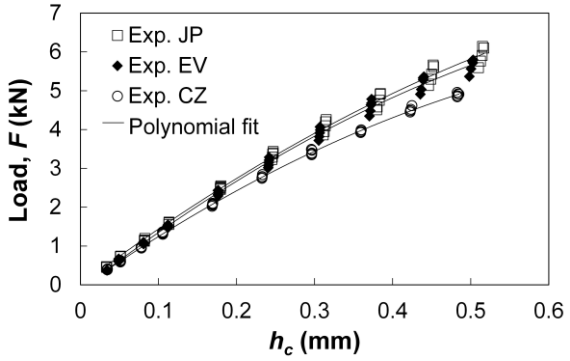

Figure 5.20 Curve fitting between the indentation load (F) and the contact depth (h_c) of three rail steels using quadratic polynomial functions

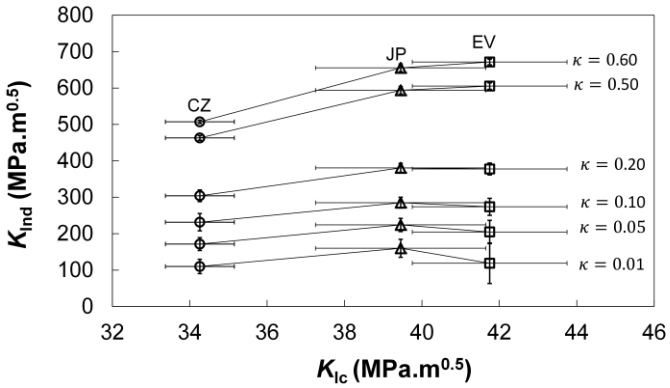

Figure 5.21 The indentation fracture toughness (K_{Ind}) estimated by adjusting the D_{cr} at the crack tip using κ in the range from 0.01 to 0.6, and compared with the K_{Ic} for the three rail steels

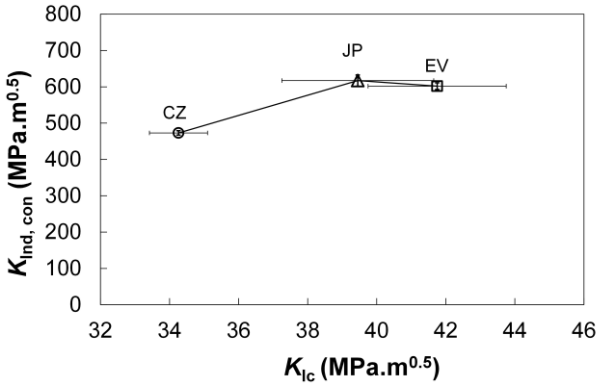

Figure 5.22 The conventional indentation fracture toughness ($K_{Ind,con}$) estimated by the D_{cr} from the smooth specimen, and compared with the K_{Ic} for the three rail steels

Fig. 5.22 presents $K_{Ind,con}$ for the three rail steels, calculated using h_c^* based on the D_{cr} value from the smooth specimens. The figure suggests that similar to that shown in Fig. 5.21, the $K_{Ind,con}$ has a value bigger than that of K_{Ic}. In addition, the $K_{Ind,con}$ values for the three rail steels is generally in an order that is consistent with that of the K_{Ic} values.

In view of the results shown in Figs. 5.21 and 5.22, it is suggested that when there is a clear difference in the fracture toughness for the rail steels, such as between the CZ and JP rail steels, both K_{Ind} and $K_{Ind,con}$ can be used to establish their ranking of K_{Ic}. However, when the difference in fracture toughness is small, such as between the EV and JP rail steels, further study is needed, first to reduce scattering of the measured K_{Ic} values, and then to determine whether K_{Ind} or $K_{Ind,con}$ can reflect the difference of K_{Ic}.

5.5 Conclusions

In this chapter, an investigation was carried out to elucidate effects of stress triaxiality on fracture strain and damage parameter for three types of high-strength rail steels. The study shows that with the increase of stress triaxiality fracture strain decreases, while the critical damage parameter increases. The results also

suggest that fracture strain at the crack tip is close to the yield strain for smooth specimens, and that the rate of damage evolution increases with the increase of stress triaxiality. Value for the critical damage parameter at the crack tip, estimated based on results from notch-free specimens, was found to be nearly twice as big as that for the smooth specimen. Furthermore, at a high stress triaxiality level, difference of the critical damage parameter between the EV and JP rail steels become negligible.

The study also determined both K_{Ind} and $K_{\text{Ind,con}}$ for the three types of high-strength rail steels. The former is based on D_{cr} at the crack tip of the pre-cracked SENB specimen, and the latter the smooth specimen. The study found that both K_{Ind} and $K_{\text{Ind,con}}$ can be used to identify the ranking of K_{Ic} for materials that show an obvious difference in the fracture toughness. However, for materials that have similar fracture toughness, scattering of the measured values becomes an issue to distinguish the difference in the fracture toughness. Another issue that needs to be resolved in the future study is the potential difference of critical damage parameter values in different loading modes.

5.6 Appendix A

The load frame compliance, C_f, of the current indentation testing system was calibrated using a standard hardness testing block of Brinell hardness 203 (HBW 10/3000) and Young's modulus 210 GPa. The indentation test was conducted at ten different displacements of 0.03, 0.05, 0.08, 0.1, 0.12, 0.14, 0.15, 0.17, 0.19, and 0.21 mm. Figure 5.A1(a) presents a set of results from an indentation loading-unloading test, where the unloading curves are best fitted using a power-law function, $F = B\left(h - h_f\right)^m$ in which the two fitting parameters, B and m, are determined using the least square fitting method.

Validity of the indentation test set-up was firstly evaluated by examining the ability to regenerate hardness of a standard testing block. Following the previous

works on the hardness measurement using indentation load-contact depth curve [114, 203], Brinell hardness at each contact depth were calculated and presented in Figure 5.A1(b). It should be noted that no obvious pile-up was observed for the standard hardness testing block when subjected to the selected indentation depths. Therefore, h_{pile} was not considered when calculating h_c. Figure 5.A1(b) indicates clearly that the measured hardness values agree well with the reference Brinell hardness of the standard testing block, with a slight increase in the hardness values at small h_c, due to deformation-induced strain-hardening on the testing block [197].

The second validation process of the hardness test setup was to regenerate Young's modulus of the standard hardness testing block. The elastic modulus is determined from the indentation test based on the Hertzian contact law [5] and Sneddon's elastic punch theory [6], as shown in Eq. (5.7). However, separating the specimen compliance (C_s) from the directly measured unloading compliance (C) is required, as the latter contains both frame and specimen compliances. The frame compliance, C_f, can be determined using the following equation based on the procedure given in ref. [203]:

$$C_f = C - \frac{\sqrt{\pi}}{2E_{\text{eff}}}\frac{1}{\sqrt{A_c}} \tag{A.1}$$

where the effective elastic modulus, E_{eff}, is defined as

$$\frac{1}{E_{\text{eff}}} = \frac{1-v_i^2}{E_i} + \frac{1-v^2}{E_0} \tag{A.2}$$

As shown in Figure 5.A2(a), variation of C_f measured for the current indentation test set-up can be described reasonably well using the following logarithmic function, consistent with that reported before [219].

$$C_f = C_0 + \frac{1}{\tilde{E}}\frac{1}{2\pi R}\ln\left(\frac{2R-h_c}{h_c}\right) \quad \text{(A.3)}$$

where C_0 and $\tilde{E}$ are the two variables for which the values are determined using the least-square-fitting method, representing constant frame compliance and effective modulus of the entire indentation system, respectively.

By substituting Eq. (A.3) into Eq. (5.8), C_s is determined. Thus, E^* for the testing block can be calculated using Eq. (5.7). Figure 5.A2(b) presents the calculated E^* values as a function of h_c. In view of the small h_c values in Figure 5.A2(b), not much damage has been accumulated, thus the measured elastic moduli in Figure 5.A2(b) showing good agreement with the Young's modulus of standard hardness testing block.

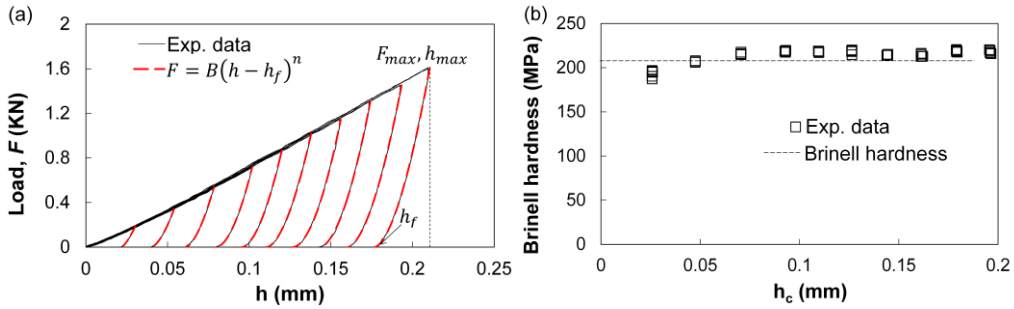

Figure 5.A1 Plots of (a) indentation load-unload curves and (b) Brinell hardness values for the standard testing block

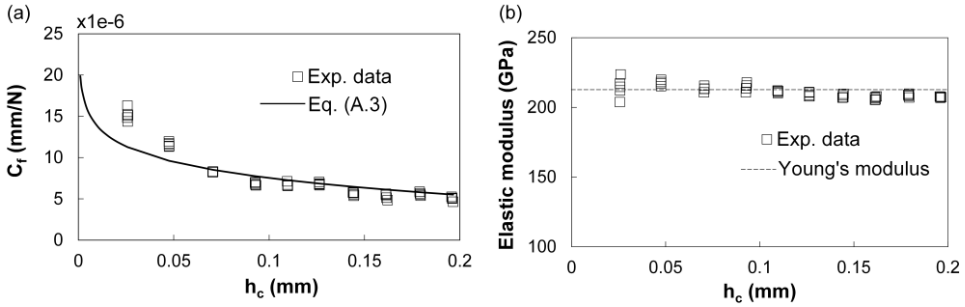

Figure 5.A2 Determination of (a) frame compliance and (b) indentation elastic modulus for the standard hardness testing block

Chapter 6 Conclusions and Future Work

6.1 Conclusions

The ultimate goal of this research project is to develop convenient testing methods to estimate the fracture toughness of high-strength rail steels. In this study, determining the fundamental mechanical properties of such steels through the use of ASTM standards, and interpreting their deformation and fracture behaviour through the use of a new constitutive model involving stress-triaxiality-dependent plasticity and damage, have improved our understanding and knowledge of their material properties. Both destructive and non-destructive testing methods were developed to estimate the fracture toughness of high-strength rail steels. The main contributions of this thesis can be summarized as follows.

Mechanical properties of three types of high-strength rail steels, including the constitutive equation, Vickers hardness and K_{Ic}, were characterized over the entire cross-section of the rail track at 23, -10, and -40^{o}C. The purpose of this characterization was to use the change occurring in K_{Ic} with decreasing temperature to assess the potential impact of low temperature on the rail breaks. The K_{Ic} for all three rail steels was found to be temperature-dependent and decreased by approximately 20% as the temperature decreased from 23 to -40^{o}C. However, at -40^{o}C, all three rail steels showed similar fracture toughness. The test results suggest that all three rail steels tested are more susceptible to impact damage and rail breaks in the Canadian winter months. In addition, the Vickers hardness and constitutive equation were also evaluated over the cross-section of the rail head and foot at all three temperatures. The experimental results, as the key finding of our investigation, showed that K_{Ic} values for the three high-strength rail steels do not follow the trend of difference based on their tensile properties.

To understand the above inconsistency between K_{Ic} values and the tensile properties, an extended strain energy density (SED) approach, considering the stress triaxiality effect on both distortional and dilatational SEDs under small-scale yielding, was used to predict fracture toughness for the three rail steels at 23, -10, and -40^{o}C. First, the equivalent plastic fracture strain of the pre-cracked SENB specimen was extrapolated from the locus of equivalent plastic fracture strain versus average stress triaxiality to the stress triaxiality level at the crack tip. It was found that the predicted fracture strain for the pre-cracked SENB specimen was reduced significantly in the vicinity of the yield strain, and the conventionally calibrated constitutive equation of the rail steels was insensitive to the change in stress triaxiality. Based on the information about the fracture strain, stress triaxiality, and constitutive equation for the two notch-free and the pre-cracked SENB specimens, it was found that the distortional SED decreased, while the dilatational SED increased, with an increase in stress triaxiality. Therefore, by summing up the values of the two types of SEDs at the crack tip of the pre-cracked SENB specimen, the magnitude of the total SED of the EV rail steel was found to be larger than that of the JP rail steel. As well, the critical SED factor, calculated by using the product of the total SED and the characteristic distance ahead of the crack tip, agreed well with the experimental K_{Ic} values for the three rail steels at 23, -10, and -40^{o}C. Therefore, it was concluded that both distortional and dilatational SEDs were indispensable factors that need to be considered for calculating the energy consumed in the elastic-plastic deformation process that leads to fracture. Moreover, the dilatational component of the total SED (or damage energy dissipation) dominates the energy consumption in the fracture process at the crack tip.

In view of the importance of damage when characterizing fracture behaviour at the crack tip, in Chapter 4, a new constitutive model of stress-triaxiality-dependent plasticity and damage was proposed for rail steels. Based on this model, it was found that even though the conventionally determined constitutive equations of rail steels were insensitive to a change in stress triaxiality, both the

damage-free stress response to deformation and damage evolution increased with an increase in stress triaxiality. Therefore, the increase of the damage-free stress response to deformation, caused by the increase in stress triaxiality, can be offset by the stress decrease caused by the increase of damage development, resulting in a conventionally determined stress-strain curve that was insensitive to the change in stress triaxiality. On the other hand, the proposed constitutive model can also be applied to explain the possibility that the conventional stress-strain curves of some materials are dependent on changes in stress triaxiality. Thus, this constitutive model can be further extended to reconcile the inconsistency in the extent to which conventional stress-strain curves depend on stress triaxiality.

In Chapter 5, the principles of a non-destructive ball indentation testing method, designed to determine the indentation fracture toughness (K_{Ind}) of three types of high-strength rail steels, were described. Both the conventional indentation fracture toughness ($K_{Ind,con}$) and K_{Ind} were calculated for three types of high-strength rail steels. The former is based on the D_{cr} from the smooth specimen; the latter is based on the D_{cr} at the crack tip including the adjusting parameter κ to accommodate the potential difference of D_{cr} between tensile fracture and indentation compression. Both approaches can identify ranking order of K_{Ic} in materials with obvious difference in fracture toughness. However, for materials that show small difference in fracture toughness, i.e., within the scattering of the measured data, the K_{Ind} may show different trend with the $K_{Ind,con}$, depending on the κ value to reconcile the difference caused by the change in loading mode from tensile fracture to indentation compression. Such an issue needs further investigation using materials that cover a wide range of fracture toughness.

This study also found that although material damage is not traditionally considered to be a factor that affects mechanical properties, its existence actually plays an important role in understanding the inconsistency between the fracture toughness (K_{Ic}) and tensile properties, both explaining the independence of conventionally calibrated stress-strain curves from the stress triaxiality, and

permitting us to develop the non-destructive indentation fracture toughness testing method for rail steels.

6.2 Future work

Overall, two new testing methods for predicting fracture toughness in high-strength rail steels were established in this research project. However, neither of them is ready to be applied to engineering practices. For the first destructive testing method, in addition to the two notch-free specimens, the accurate stress state ahead of the crack tip must be determined in order to predict K_{Ic} accurately. In the current study, finite element modelling was used to mimic the linear portion of the SENB tests and thus to determine the stress-strain distribution ahead of the crack tip. In order to use test data only from two types of notch-free specimens to predict the fracture toughness, the stress state at the crack tip should be determined without relying on data from the SENB tests.

As concerns the non-destructive indentation technique, the current method can only be used to identify the ranking of the mode I critical stress intensity factor (K_{Ic}) for the three high-strength rail steels, not directly to measure the K_{Ic} values. This is probably because of the size effect of the damage zone generated under different diameters of the ball indenter.

In order to improve the above two testing methods, the following problems are recommended for future investigation:

- *Characterization of the stress-strain field at the crack tip*: In view of many existing approaches to analyze the stress-strain distribution around notches and cracks, such as the SIF, NSIF and energy density approaches [30, 59, 235], the stress-strain distribution ahead of the crack tip can probably be determined without performing the SENB tests. This future research has the potential to enable the destructive testing method to be used in engineering applications.

- *Effect of the diameter of the ball indenter on damage evolution (size effect)*: It is reasonable to speculate that by using different diameters of ball indenter, the damage evolution of rail steels under indentation will be similar, while the specific indentation energy to fracture will be proportional to the size of the ball tip. Therefore, through extrapolation, the accurate size of the ball indenter tip to a size comparable to the crack tip, K_{Ic} can be determined; and thus, this non-destructive indentation technique can be applied to engineering applications. Further work should be carried out in order to verify this hypothesis.

On the other hand, it was found that although the JP rail steel is both stronger and more ductile than the EV rail steel, K_{Ic} of the former is smaller than that of the latter at 23 and -10^{o}C. While at -40^{o}C, their K_{Ic} values are reduced to the same level. It has been wondered what makes the EV rail steel tougher than the JP rail steel, though the latter is stronger and more ductile. Resolving mechanisms that are responsible for such a complex phenomenon requires further investigation by looking into the influence of different microstructures on fracture toughness between these two rail steels. It will definitely be beneficial if the future study investigates mechanisms and microstructures that are responsible for maximizing fracture toughness for rail steels in cold climate condition.

References

[1] Knupp G, Chidley W, Giove J, Hartman H, Morris G, Taylor C. A Review of the Manufacture, Processing, and Use of Rail Steels in North America—A Report of AISI Technical Subcommittee on Rails and Accessories. Rail Steels—Developments, Processing, and Use: ASTM International; 1978.
[2] Yu F, Ben Jar PY, Hendry M. Fracture behaviour at the sharp notch tip of high strength rail steels - Influence of stress triaxiality. Engineering Fracture Mechanics. 2017.
[3] Zerbst U, Lundén R, Edel KO, Smith RA. Introduction to the damage tolerance behaviour of railway rails – a review. Engineering Fracture Mechanics. 2009;76:2563-601.
[4] Leishman EM, Hendry MT, Martin CD. Canadian main track derailment trends, 2001 to 2014. Canadian Journal of Civil Engineering. 2017.
[5] Liu X, Lovett A, Dick T, Rapik Saat M, Barkan CP. Optimization of ultrasonic rail-defect inspection for improving railway transportation safety and efficiency. Journal of Transportation Engineering. 2014;140:04014048.
[6] Canada TSBo. RAILWAY INVESTIGATION REPORT R13E0142. 2013.
[7] Lewandowski J, Thompson A. Microstructural effects on the cleavage fracture stress of fully pearlitic eutectoid steel. Metallurgical and Materials Transactions A. 1986;17:1769-86.
[8] Lewandowski JJ, Thompson AW. Effects of the prior austenite grain size on the ductility of fully pearlitic eutectoid steel. Metallurgical and Materials Transactions A. 1986;17:461-72.
[9] Lewandowski J, Thompson A. Micromechanisms of cleavage fracture in fully pearlitic microstructures. Acta Metallurgica. 1987;35:1453-62.
[10] Alexander D, Bernstein I. Cleavage fracture in pearlitic eutectoid steel. Metallurgical and Materials Transactions A. 1989;20:2321-35.
[11] Clayton P. The relations between wear behaviour and basic material properties for pearlitic steels. Wear. 1980;60:75-93.
[12] Hyzak JM, Bernstein IM. The role of microstructure on the strength and toughness of fully pearlitic steels. Metallurgical Transactions A. 1976;7:1217-24.
[13] Young J. United Kingdom development of rails rolled from continuously cast blooms. Rail Steels—Developments, Processing, and Use: ASTM International; 1978.
[14] Yates J. Innovation in rail steel. Science in Parliament. 1996;53:2-3.
[15] Sharma S, Sangal S, Mondal K. Wear behaviour of bainitic rail and wheel steels. Materials Science and Technology. 2016;32:266-74.
[16] Leishman E. Analysis of Canadian Train Derailments from 2001 to 2014. University of Alberta2016.
[17] Standard ASTM. E8/E8M Standard test methods for tension testing of metallic materials. ASTM International, West Conshohocken, PA. 2011.
[18] Standard ASTM. E399 Standard Test Method for Linear-Elastic Plane-Strain Fracture Toughness KIC of Metallic Materials. ASTM International, West Conshohocken, PA. 2012.
[19] E384 A. Standard Test Method for Microindentation Hardness of Materials. ASTM International, West Conshohocken, PA; 2016.
[20] Service SR. Rail Defect Manual: Sperry Rail Service; 1999.
[21] Ueda M, Seki K, Satou T, Yamamoto T. Pearlite rail having superior abrasion resistance and excellent toughness. Google Patents; 2009.
[22] UEDA M, UCHINO K, MATSUSHITA K, KOBAYASHI A. Development of HE rails with high wear and damage resistance for heavy haul railways. Nippon steel technical report Overseas. 2002:167-72.
[23] Jha A, Prasad B, Modi O, Das S, Yegneswaran A. Correlating microstructural features and mechanical properties with abrasion resistance of a high strength low alloy steel. Wear. 2003;254:120-8.
[24] Moore M. The relationship between the abrasive wear resistance, hardness and microstructure of ferritic materials. Wear. 1974;28:59-68.

[25] Xu L, Kennon NF. A study of the abrasive wear of carbon steels. Wear. 1991;148:101-12.
[26] Griffith AA. The phenomena of rupture and flow in solids. Philosophical transactions of the royal society of london Series A, containing papers of a mathematical or physical character. 1921;221:163-98.
[27] Irwin GR. Fracture dynamics. Fracturing of metals. 1948;152.
[28] Orowan E. Fracture and strength of solids. Reports on progress in physics. 1949;12:185.
[29] Irwin GR. Onset of fast crack propagation in high strength steel and aluminum alloys. Sagamore Research Conference Proceedings. 1956;2:289-305.
[30] Williams M. The bending stress distribution at the base of a stationary crack. Trans ASME. 1957;79:109-14.
[31] Anderson T. Fracture mechanics: fundamentals and applications: CRC press; 2005.
[32] Ritchie RO, Knott JF, Rice J. On the relationship between critical tensile stress and fracture toughness in mild steel. Journal of the Mechanics and Physics of Solids. 1973;21:395-410.
[33] Inglis CE. Stresses in a plate due to the presence of cracks and sharp corners. Spie Milestone series MS. 1997;137:3-17.
[34] Irwin G. Analysis of Stresses and Strains Near the End of a Crack Traversing a Plate. J Appl Mech. 1957.
[35] Westergaard H. Bearing pressures and cracks.
[36] Hutchinson J. Singular behaviour at the end of a tensile crack in a hardening material. Journal of the Mechanics and Physics of Solids. 1968;16:13-31.
[37] Rice J, Rosengren GF. Plane strain deformation near a crack tip in a power-law hardening material. Journal of the Mechanics and Physics of Solids. 1968;16:1-12.
[38] Rice JR, Johnson MA. The Role of Large Crack Tip Geometry Changes in Plane Strain Fracture: Division of Engineering, Brown University; 1969.
[39] Curry D, Knott J. Effects of microstructure on cleavage fracture stress in steel. Metal Science. 1978;12:511-4.
[40] Watanabe J, Iwadate T, Tanaka Y, Yokobori T, Ando K. Fracture toughness in the transition region. Engineering Fracture Mechanics. 1987;28:589-600.
[41] Neimitz A, Graba M, Gałkiewicz J. An alternative formulation of the Ritchie–Knott–Rice local fracture criterion. Engineering Fracture Mechanics. 2007;74:1308-22.
[42] Shlyannikov V, Boychenko N, Fernández-Canteli A, Muñiz-Calvente M. Elastic and plastic parts of strain energy density in critical distance determination. Engineering Fracture Mechanics. 2015;147:100-18.
[43] McClintock FA. Plasticity aspects of fracture. Fracture: an advanced treatise. 1971;3:47-225.
[44] Mackenzie A, Hancock J, Brown D. On the influence of state of stress on ductile failure initiation in high strength steels. Engineering fracture mechanics. 1977;9:167IN13169-168IN4188.
[45] Pandey R, Banerjee S. Strain induced fracture in low strength steels. Engineering Fracture Mechanics. 1978;10:817-29.
[46] Ritchie R, Server W, Wullaert R. Critical fracture stress and fracture strain models for the prediction of lower and upper shelf toughness in nuclear pressure vessel steels. Metallurgical Transactions A. 1979;10:1557-70.
[47] Coates M, Kumar A, Roberts SG. Crack initiation in the brittle fracture of ferritic steels. Fatigue Fracture of Engineering Materials and Structures. 2006;29:661-71.
[48] Kim Y-H, Kwon D, Lee S. KIC Modelling for a critical strain criterion involving the stress triaxiality effect. Acta Metallurgica et Materialia. 1994;42:1887-91.
[49] Atzori B, Lazzarin P, Tovo R. STRESS DISTRIBUTIONS FOR V-SHAPED NOTCHES UNDER TENSILE AND BENDING LOADS. Fatigue & Fracture of Engineering Materials & Structures. 1997;20:1083-92.
[50] Gross B, Mendelson A. Plane elastostatic analysis of V-notched plates. International Journal of Fracture Mechanics. 1972;8:267-76.
[51] Lazzarin P, Tovo R. A unified approach to the evaluation of linear elastic stress fields in the neighborhood of cracks and notches. International Journal of Fracture. 1996;78:3-19.

[52] Lazzarin P, Tovo R. A notch intensity factor approach to the stress analysis of welds. Fatigue & fracture of engineering materials & structures. 1998;21:1089-103.
[53] Carpinteri A. Stress-singularity and generalized fracture toughness at the vertex of re-entrant corners. Engineering Fracture Mechanics. 1987;26:143-55.
[54] Gómez FJ, Elices M. A fracture criterion for sharp V-notched samples. International Journal of Fracture. 2003;123:163-75.
[55] Nui LS, Chehimi C, Pluvinage G. Stress field near a large blunted tip V-notch and application of the concept of the critical notch stress intensity factor (NSIF) to the fracture toughness of very brittle materials. Engineering Fracture Mechanics. 1994;49:325-35.
[56] Seweryn A. Brittle fracture criterion for structures with sharp notches. Engineering Fracture Mechanics. 1994;47:673-81.
[57] Filippi S, Ciavarella M, Lazzarin P. An approximate, analytical approach to theHRR'-solution for sharp V-notches. International journal of fracture. 2002;117:269-86.
[58] Lazzarin P, Zambardi R, Livieri P. Plastic notch stress intensity factors for large V-shaped notches under mixed load conditions. International Journal of Fracture. 2001;107:361-77.
[59] Berto F, Lazzarin P. Recent developments in brittle and quasi-brittle failure assessment of engineering materials by means of local approaches. Materials Science and Engineering: R: Reports. 2014;75:1-48.
[60] Sih G. Mechanics and physics of energy density theory. Theoretical and applied fracture mechanics. 1985;4:157-73.
[61] Sih G. A special theory of crack propagation. Mechanics of fracture initiation and propagation: Springer; 1991. p. 1-22.
[62] Sih G, Ho J. Sharp notch fracture strength characterized by critical energy density. Theoretical and Applied Fracture Mechanics. 1991;16:179-214.
[63] Sih G, Tzou D. Heating preceded by cooling ahead of crack: macrodamage free zone. Theoretical and Applied Fracture Mechanics. 1986;6:103-11.
[64] Sih GC. Strain-energy-density factor applied to mixed mode crack problems. International Journal of fracture. 1974;10:305-21.
[65] Sih GC. Mechanics of Fracture Initiation and Propagation: Surface and volume energy density applied as failure criterion: Springer Netherlands; 2012.
[66] Shlyannikov V. Modelling of crack growth by fracture damage zone. Theoretical and applied fracture mechanics. 1996;25:187-201.
[67] Gillemot F, Czoboly E, Havas I. Fracture mechanics applications of absorbed specific fracture energy: Notch and unnotched specimens. Theoretical and Applied Fracture Mechanics. 1985;4:39-45.
[68] Gillemot LF. Criterion of crack initiation and spreading. Engineering Fracture Mechanics. 1976;8:239-53.
[69] Berto F. Fatigue and fracture assessment of notched components by means of the Strain Energy Density. Engineering Fracture Mechanics. 2016;167:176-87.
[70] Berto F, Lazzarin P. A review of the volume-based strain energy density approach applied to V-notches and welded structures. Theoretical and Applied Fracture Mechanics. 2009;52:183-94.
[71] Radaj D, Berto F, Lazzarin P. Local fatigue strength parameters for welded joints based on strain energy density with inclusion of small-size notches. Engineering Fracture Mechanics. 2009;76:1109-30.
[72] Lazzarin P, Berto F. Control volumes and strain energy density under small and large scale yielding due to tension and torsion loading. Fatigue & Fracture of Engineering Materials & Structures. 2008;31:95-107.
[73] Lazzarin P, Zambardi R. The Equivalent Strain Energy Density approach re-formulated and applied to sharp V-shaped notches under localized and generalized plasticity. Fatigue & Fracture of Engineering Materials & Structures. 2002;25:917-28.
[74] Lazzarin P, Berto F, Zappalorto M. Rapid calculations of notch stress intensity factors based on averaged strain energy density from coarse meshes: Theoretical bases and applications. International Journal of Fatigue. 2010;32:1559-67.

[75] Chaouadi R, De Meester P, Vandermeulen W. Damage work as ductile fracture criterion. International Journal of Fracture. 1994;66:155-64.
[76] Evans AG, Charles EA. Fracture toughness determinations by indentation. Journal of the American Ceramic society. 1976;59:371-2.
[77] Anstis G, Chantikul P, Lawn BR, Marshall D. A critical evaluation of indentation techniques for measuring fracture toughness: I, direct crack measurements. Journal of the American Ceramic Society. 1981;64:533-8.
[78] Niihara K. A fracture mechanics analysis of indentation-induced Palmqvist crack in ceramics. Journal of Materials Science Letters. 1983;2:221-3.
[79] Miyoshi T, Sagawa N, Sassa T. Study on fracture toughness evaluation for structural ceramics. Trans Jap Soc Mech Eng. 1985;51:2487-9.
[80] Haggag FM, Byun T-S, Hong JH, Miraglia PQ, Murty KL. Indentation-energy-to-fracture (IEF) parameter for characterization of DBTT in carbon steels using nondestructive automated ball indentation (ABI) technique. Scripta Materialia. 1998;38:645-51.
[81] Byun TS, Kim SH, Lee BS, Kim IS, Hong JH. Estimation of fracture toughness transition curves of RPV steels from ball indentation and tensile test data. Journal of Nuclear Materials. 2000;277:263-73.
[82] Lee J-S, Jang J-i, Lee B-W, Choi Y, Lee SG, Kwon D. An instrumented indentation technique for estimating fracture toughness of ductile materials: A critical indentation energy model based on continuum damage mechanics. Acta Materialia. 2006;54:1101-9.
[83] Ghosh S, Das G. Effect of pre-strain on the indentation fracture toughness of high strength low alloy steel by means of continuum damage mechanics. Engineering Fracture Mechanics. 2012;79:126-37.
[84] Li J, Li F, He M, Xue F, Zhang M, Wang C. Indentation technique for estimating the fracture toughness of 7050 aluminum alloy with the Berkovich indenter. Materials & Design. 2012;40:176-84.
[85] Amiri S, Lecis N, Manes A, Giglio M. A study of a micro-indentation technique for estimating the fracture toughness of Al6061-T6. Mechanics Research Communications. 2014;58:10-6.
[86] Li J, Li F, Ma X, Wang Q, Dong J, Yuan Z. A strain-dependent ductile damage model and its application in the derivation of fracture toughness by micro-indentation. Materials & Design. 2015;67:623-30.
[87] Byun TS, Kim JW, Hong JH. A theoretical model for determination of fracture toughness of reactor pressure vessel steels in the transition region from automated ball indentation test. Journal of Nuclear Materials. 1998;252:187-94.
[88] Haggag FM, Nanstad RK, Hutton JT, Thomas DL, Swain RL. Use of automated ball indentation testing to measure flow properties and estimate fracture toughness in metallic materials. Applications of automation technology to fatigue and fracture testing: ASTM International; 1990.
[89] Jeon SW, Lee KW, Kim JY, Kim WJ, Park CP, Kwon D. Estimation of Fracture Toughness of Metallic Materials Using Instrumented Indentation: Critical Indentation Stress and Strain Model. Experimental Mechanics. 2016.
[90] Lemaitre J. A course on damage mechanics: Springer Science & Business Media; 2012.
[91] Tai WH. Plastic damage and ductile fracture in mild steels. Engineering Fracture Mechanics. 1990;37:853-80.
[92] Bonora N, Ruggiero A, Esposito L, Gentile D. CDM modeling of ductile failure in ferritic steels: Assessment of the geometry transferability of model parameters. International Journal of Plasticity. 2006;22:2015-47.
[93] Mirza M, Barton D, Church P. The effect of stress triaxiality and strain-rate on the fracture characteristics of ductile metals. Journal of materials science. 1996;31:453-61.
[94] Brünig M, Gerke S, Hagenbrock V. Micro-mechanical studies on the effect of the stress triaxiality and the Lode parameter on ductile damage. International Journal of Plasticity. 2013;50:49-65.

[95] Brünig M, Gerke S, Hagenbrock V. Stress-state-dependence of damage strain rate tensors caused by growth and coalescence of micro-defects. International Journal of Plasticity. 2014;63:49-63.
[96] Malcher L, Mamiya EN. An improved damage evolution law based on continuum damage mechanics and its dependence on both stress triaxiality and the third invariant. International Journal of Plasticity. 2014;56:232-61.
[97] Sahay SS, Mohapatra G, Totten GE. Overview of Pearlitic Rail Steel: Accelerated Cooling, Quenching, Microstructure, and Mechanical Properties. Journal of ASTM International. 2009;6.
[98] Zerbst U, Lundén R, Edel K-O, Smith RA. Introduction to the damage tolerance behaviour of railway rails–a review. Engineering fracture mechanics. 2009;76:2563-601.
[99] Szablewski D, Kalay S, LoPresti J. Development and Evaluation of High Performance Rail Steels for Heavy Haul Operations. Proceedings of the 2011 international heavy haul association conference, Calgary, Canada2011. p. 19-22.
[100] Wang Y-q, Zhou H, Shi Y-j, Feng B-r. Mechanical properties and fracture toughness of rail steels and thermite welds at low temperature. International Journal of Minerals, Metallurgy, and Materials. 2012;19:409-20.
[101] Bandula-Heva T DM. Determination of Stress-Strain Characteristics of railhead steel using image analysis. 2011.
[102] Choung JM, Cho SR. Study on true stress correction from tensile tests. Journal of Mechanical Science and Technology. 2008;22:1039-51.
[103] Bridgman PW. Studies in large plastic flow and fracture: McGraw-Hill New York; 1952.
[104] Joun M, Choi I, Eom J, Lee M. Finite element analysis of tensile testing with emphasis on necking. Computational Materials Science. 2007;41:63-9.
[105] Koc P, Štok B. Computer-aided identification of the yield curve of a sheet metal after onset of necking. Computational Materials Science. 2004;31:155-68.
[106] Sung JH, Kim JH, Wagoner RH. A plastic constitutive equation incorporating strain, strain-rate, and temperature. International Journal of Plasticity. 2010;26:1746-71.
[107] Zhang K, Li Z. Numerical analysis of the stress-strain curve and fracture initiation for ductile material. Engineering fracture mechanics. 1994;49:235-41.
[108] Oku T, Sato S, Fujimura T. The detection of embrittlement in steels by means of hardness measurements. Nuclear Structural Engineering. 1965;2:282-92.
[109] Ogden R. Large deformation isotropic elasticity-on the correlation of theory and experiment for incompressible rubberlike solids. Proceedings of the Royal Society of London A Mathematical and Physical Sciences. 1972;326:565-84.
[110] Voce E. The relationship between stress and strain for homogeneous deformation. J Inst Met. 1948;74:537-62.
[111] Hollomon JH. Tensile deformation. AIME TRANS. 1945;12:1-22.
[112] Freeman JR, Derry AT. Effect of hot-rolling conditions on the physical properties of a carbon steel. Journal of the Franklin Institute. 1925;199:251-2.
[113] Lee J, Subramanian K. Young's modulus of cold-and hot-rolled (Al 2 O 3) p-Al composite. Journal of materials science. 1994;29:4901-5.
[114] Doerner MF, Nix WD. A method for interpreting the data from depth-sensing indentation instruments. Journal of Materials research. 1986;1:601-9.
[115] Nix WD, Gao H. Indentation size effects in crystalline materials: a law for strain gradient plasticity. Journal of the Mechanics and Physics of Solids. 1998;46:411-25.
[116] Li H, Ghosh A, Han Y, Bradt R. The frictional component of the indentation size effect in low load microhardness testing. Journal of Materials Research. 1993;8:1028-32.
[117] Alexander D, Bernstein I. Cleavage fracture in pearlitic eutectoid steel. Metallurgical Transactions A. 1989;20:2321-35.
[118] Wallin K. The scatter in KIC-results. Engineering Fracture Mechanics. 1984;19:1085-93.
[119] Chait R. Factors influencing the strength differential of high strength steels. Metallurgical and Materials Transactions B. 1972;3:369-75.

[120] Dao M, Chollacoop N, Van Vliet K, Venkatesh T, Suresh S. Computational modeling of the forward and reverse problems in instrumented sharp indentation. Acta materialia. 2001;49:3899-918.
[121] Giannakopoulos A, Larsson P-L, Vestergaard R. Analysis of Vickers indentation. International journal of solids and structures. 1994;31:2679-708.
[122] Antunes J, Fernandes J, Menezes L, Chaparro B. A new approach for reverse analyses in depth-sensing indentation using numerical simulation. Acta Materialia. 2007;55:69-81.
[123] Haggag FM, Nanstad RK, Hutton JT, Thomas DL, Swain RL. Use of automated ball indentation testing to measure flow properties and estimate fracture toughness in metallic materials. ASTM STP. 1990;1092:188-208.
[124] Tho K, Swaddiwudhipong S, Liu Z, Zeng K, Hua J. Uniqueness of reverse analysis from conical indentation tests. Journal of materials research. 2004;19:2498-502.
[125] McClintock FA. A criterion for ductile fracture by the growth of holes. Journal of applied mechanics. 1968;35:363-71.
[126] Rice JR, Tracey DM. On the ductile enlargement of voids in triaxial stress fields∗. Journal of the Mechanics and Physics of Solids. 1969;17:201-17.
[127] Lemaitre J. A Continuous Damage Mechanics Model for Ductile Fracture. Journal of Engineering Materials and Technology. 1985.
[128] Bonora N. A nonlinear CDM model for ductile failure. Engineering Fracture Mechanics. 1997;58:11-28.
[129] Hancock J, Mackenzie A. On the mechanisms of ductile failure in high-strength steels subjected to multi-axial stress-states. Journal of the Mechanics and Physics of Solids. 1976;24:147-60.
[130] Bao Y, Wierzbicki T. On fracture locus in the equivalent strain and stress triaxiality space. International Journal of Mechanical Sciences. 2004;46:81-98.
[131] Kim N-H, Oh C-S, Kim Y-J, Yoon K-B, Ma Y-H. Comparison of fracture strain based ductile failure simulation with experimental results. International Journal of Pressure Vessels and Piping. 2011;88:434-47.
[132] Smith E. Cleavage fracture in mild steel. International Journal of Fracture Mechanics. 1968;4:131-45.
[133] Erdogan F, Sih G. On the crack extension in plates under plane loading and transverse shear. Journal of basic engineering. 1963;85:519-27.
[134] Cao J, Li F, Li P, Ma X, Li J. Analysis of ductile–brittle competitive fracture criteria for tension process of 7050 aluminum alloy based on elastic strain energy density. Materials Science and Engineering: A. 2015;637:201-14.
[135] Lazzarin P, Zambardi R. A finite-volume-energy based approach to predict the static and fatigue behavior of components with sharp V-shaped notches. International Journal of Fracture. 2001;112:275-98.
[136] Lazzarin P, Berto F. Some Expressions for the Strain Energy in a Finite Volume Surrounding the Root of Blunt V-notches. International Journal of Fracture. 2005;135:161-85.
[137] Livieri P, Lazzarin P. Fatigue strength of steel and aluminium welded joints based on generalised stress intensity factors and local strain energy values. International Journal of Fracture. 2005;133:247-76.
[138] Berto F, Campagnolo A, Chebat F, Cincera M, Santini M. Fatigue strength of steel rollers with failure occurring at the weld root based on the local strain energy values: modelling and fatigue assessment. International Journal of Fatigue. 2016;82, Part 3:643-57.
[139] Gallo P, Berto F, Glinka G. Generalized approach to estimation of strains and stresses at blunt V-notches under non-localized creep. Fatigue & Fracture of Engineering Materials & Structures. 2016;39:292-306.
[140] Gallo P, Sumigawa T, Kitamura T, Berto F. Evaluation of the strain energy density control volume for a nanoscale singular stress field. Fatigue & Fracture of Engineering Materials & Structures. 2016;39:1557-64.

[141] Torabi AR. Estimation of tensile load-bearing capacity of ductile metallic materials weakened by a V-notch: The equivalent material concept. Materials Science and Engineering: A. 2012;536:249-55.
[142] Torabi AR. On the use of the Equivalent Material Concept to predict tensile load-bearing capacity of ductile steel bolts containing V-shaped threads. Engineering Fracture Mechanics. 2013;97:136-47.
[143] Gurson AL. Continuum theory of ductile rupture by void nucleation and growth: Part I—Yield criteria and flow rules for porous ductile media. Journal of engineering materials and technology. 1977;99:2-15.
[144] Tvergaard V, Needleman A. Analysis of the cup-cone fracture in a round tensile bar. Acta metallurgica. 1984;32:157-69.
[145] Huang Y. Accurate dilatation rates for spherical voids in triaxial stress fields. Journal of Applied Mechanics. 1991;58:1084-6.
[146] Bai Y, Teng X, Wierzbicki T. On the Application of Stress Triaxiality Formula for Plane Strain Fracture Testing. Journal of Engineering Materials and Technology. 2009;131:021002.
[147] Derpenski L, Seweryn A. Ductile fracture of EN-AW 2024 aluminum alloy specimens with notches under biaxial loading. Part 2 – Numerical research and ductile fracture criterion. Theoretical and Applied Fracture Mechanics. 2016;84:203-14.
[148] Suárez F, Gálvez JC, Cendón DA, Atienza JM. Fracture of eutectoid steel bars under tensile loading: Experimental results and numerical simulation. Engineering Fracture Mechanics. 2016;158:87-105.
[149] Mirone G. Role of stress triaxiality in elastoplastic characterization and ductile failure prediction. Engineering Fracture Mechanics. 2007;74:1203-21.
[150] Burdekin FM, Stone D. The crack opening displacement approach to fracture mechanics in yielding materials. The Journal of Strain Analysis for Engineering Design. 1966;1:145-53.
[151] Mihara T, Nomura M, Yamanaka K. Relations between crack opening behavior and crack tip diffraction of longitudinal wave. NDE For Health Monitoring and Diagnostics: International Society for Optics and Photonics; 2002. p. 137-45.
[152] Pook LP. A 50-year retrospective review of three-dimensional effects at cracks and sharp notches. Fatigue & Fracture of Engineering Materials & Structures. 2013;36:699-723.
[153] Shlyannikov VN, Boychenko NV, Tumanov AV, Fernández-Canteli A. The elastic and plastic constraint parameters for three-dimensional problems. Engineering Fracture Mechanics. 2014;127:83-96.
[154] McMeeking R, Parks D. On criteria for J-dominance of crack-tip fields in large-scale yielding. Elastic-plastic fracture: ASTM International; 1979.
[155] Hibbett, Karlsson, Sorensen. ABAQUS/standard: User's Manual: Hibbitt, Karlsson & Sorensen; 1998.
[156] Alves Ml, Jones N. Influence of hydrostatic stress on failure of axisymmetric notched specimens. Journal of the Mechanics and Physics of Solids. 1999;47:643-67.
[157] Welch BL. The generalization ofstudent's' problem when several different population variances are involved. Biometrika. 1947;34:28-35.
[158] Student. PROBABLE ERROR OF A CORRELATION COEFFICIENT. Biometrika. 1908;6:302-10.
[159] Ahrens H. Pearson, E. S., and H. O. Hartley (Edit.): Biometrika Tables for Statisticians Vol. I, 3. Auflage. University Press, Cambridge 1966. XVI + 264 S. Preis 35 s. Biometrische Zeitschrift. 1968;10:226-.
[160] Mendelson A. Plasticity; theory and application: Macmillan; 1968.
[161] Hill R. The mathematical theory of plasticity: Oxford university press; 1998.
[162] Spitzig WA, Richmond O. The effect of pressure on the flow stress of metals. Acta Metallurgica. 1984;32:457-63.
[163] Spitzig WA, Sober RJ, Richmond O. Pressure dependence of yielding and associated volume expansion in tempered martensite. Acta Metallurgica. 1975;23:885-93.

[164] Spitzig WA, Sober RJ, Richmond O. The effect of hydrostatic pressure on the deformation behavior of maraging and HY-80 steels and its implications for plasticity theory. Metallurgical Transactions A. 1976;7:1703-10.
[165] Drucker DC, Prager W. Soil mechanics and plastic analysis or limit design. Quarterly of applied mathematics. 1952;10:157-65.
[166] Kao A, Kuhn H, Richmond O, Spitzig W. Tensile fracture and fractographic analysis of 1045 spheroidized steel under hydrostatic pressure. Journal of Materials Research. 1990;5:83-91.
[167] Wilson CD. A Critical Reexamination of Classical Metal Plasticity. Journal of Applied Mechanics. 2002;69:63.
[168] Zhang KS, Bai JB, François D. Numerical analysis of the influence of the Lode parameter on void growth. International Journal of Solids and Structures. 2001;38:5847-56.
[169] Gao X, Kim J. Modeling of ductile fracture: Significance of void coalescence. International Journal of Solids and Structures. 2006;43:6277-93.
[170] Barsoum I, Faleskog J. Rupture mechanisms in combined tension and shear—Experiments. International Journal of Solids and Structures. 2007;44:1768-86.
[171] Achouri M, Germain G, Dal Santo P, Saidane D. Experimental characterization and numerical modeling of micromechanical damage under different stress states. Materials & Design. 2013;50:207-22.
[172] Ghajar R, Mirone G, Keshavarz A. Ductile failure of X100 pipeline steel – Experiments and fractography. Materials & Design. 2013;43:513-25.
[173] Wu B, Vajragupta N, Lian J, Hangen U, Wechsuwanmanee P, Münstermann S. Prediction of plasticity and damage initiation behaviour of C45E + N steel by micromechanical modelling. Materials & Design. 2017;121:154-66.
[174] Kim J, Gao X, Srivatsan T. Modeling of crack growth in ductile solids: a three-dimensional analysis. International journal of solids and structures. 2003;40:7357-74.
[175] Barsoum I, Faleskog J. Rupture mechanisms in combined tension and shear—Micromechanics. International Journal of Solids and Structures. 2007;44:5481-98.
[176] Bai Y, Wierzbicki T. A new model of metal plasticity and fracture with pressure and Lode dependence. International Journal of Plasticity. 2008;24:1071-96.
[177] Mirone G, Corallo D. A local viewpoint for evaluating the influence of stress triaxiality and Lode angle on ductile failure and hardening. International Journal of Plasticity. 2010;26:348-71.
[178] Krajcinovic D. Damage mechanics. Mechanics of Materials. 1989;8:117-97.
[179] Andrade Pires FM, César de Sá JMA, Costa Sousa L, Natal Jorge RM. Numerical modelling of ductile plastic damage in bulk metal forming. International Journal of Mechanical Sciences. 2003;45:273-94.
[180] Pirondi A, Bonora N. Modeling ductile damage under fully reversed cycling. Computational Materials Science. 2003;26:129-41.
[181] Bonora N, Gentile D, Pirondi A, Newaz G. Ductile damage evolution under triaxial state of stress: theory and experiments. International Journal of Plasticity. 2005;21:981-1007.
[182] Nahshon K, Hutchinson J. Modification of the Gurson model for shear failure. European Journal of Mechanics-A/Solids. 2008;27:1-17.
[183] Xue L. Constitutive modeling of void shearing effect in ductile fracture of porous materials. Engineering Fracture Mechanics. 2008;75:3343-66.
[184] Besson J. Continuum Models of Ductile Fracture: A Review. International Journal of Damage Mechanics. 2009;19:3-52.
[185] Gao X, Zhang T, Zhou J, Graham SM, Hayden M, Roe C. On stress-state dependent plasticity modeling: Significance of the hydrostatic stress, the third invariant of stress deviator and the non-associated flow rule. International Journal of Plasticity. 2011;27:217-31.
[186] Malcher L, Andrade Pires FM, César de Sá JMA. An assessment of isotropic constitutive models for ductile fracture under high and low stress triaxiality. International Journal of Plasticity. 2012;30-31:81-115.
[187] Balan T, Lemoine X, Maire E, Habraken A-M. Implementation of a damage evolution law for dual-phase steels in Gurson-type models. Materials & Design. 2015;88:1213-22.

[188] Chaboche JL, Boudifa M, Saanouni K. A CDM Approach of Ductile Damage with Plastic Compressibility. International Journal of Fracture. 2006;137:51-75.
[189] Brünig M, Chyra O, Albrecht D, Driemeier L, Alves M. A ductile damage criterion at various stress triaxialities. International Journal of Plasticity. 2008;24:1731-55.
[190] Brünig M. A Continuum Damage Model Based on Experiments and Numerical Simulations—A Review. 2015;64:19-35.
[191] Kachanov L. Time of the rupture process under creep conditions. Isv Akad Nauk SSR Otd Tekh Nauk. 1958;8:26-31.
[192] Lemaitre J, Dufailly J. Damage measurements. Engineering Fracture Mechanics. 1987;28:643-61.
[193] Celentano DJ, Chaboche J-L. Experimental and numerical characterization of damage evolution in steels. International Journal of Plasticity. 2007;23:1739-62.
[194] Hillerborg A, Modéer M, Petersson PE. Analysis of crack formation and crack growth in concrete by means of fracture mechanics and finite elements. Cement and Concrete Research. 1976;6:773-81.
[195] Malcher L, Reis FJP, Andrade Pires FM, César de Sá JMA. Evaluation of shear mechanisms and influence of the calibration point on the numerical results of the GTN model. International Journal of Mechanical Sciences. 2013;75:407-22.
[196] Teng X. Numerical prediction of slant fracture with continuum damage mechanics. Engineering Fracture Mechanics. 2008;75:2020-41.
[197] Tabor D. The hardness of metals: Oxford university press; 1951.
[198] Atkins A, Tabor D. Plastic indentation in metals with cones. Journal of the Mechanics and Physics of Solids. 1965;13:149-64.
[199] Richmond O, Morrison HL, Devenpeck ML. Sphere indentation with application to the Brinell hardness test. International Journal of Mechanical Sciences. 1974;16:75-82.
[200] Bulychev S, Alekhin V, Shorshorov M, Ternovskii A, Shnyrev G. Determining Young's modulus from the indentor penetration diagram. Ind Lab. 1975;41:1409-12.
[201] Hertz H. Hertz's Miscellaneous Papers; Chapters 5 and 6. ed: Macmillan, London, UK. 1896.
[202] Sneddon IN. The relation between load and penetration in the axisymmetric Boussinesq problem for a punch of arbitrary profile. International journal of engineering science. 1965;3:47-57.
[203] Oliver WC, Pharr GM. Measurement of hardness and elastic modulus by instrumented indentation: Advances in understanding and refinements to methodology. Journal of materials research. 2004;19:3-20.
[204] Norbury A, Samuel T. The recovery and sinking-in or piling-up of material in the Brinell test, and the effects of these factors on the correlation of the Brinell with certain other hardness tests. Journal of Iron and Steel Institute. 1928;117:673-87.
[205] Matthews J. Indentation hardness and hot pressing. Acta metallurgica. 1980;28:311-8.
[206] Hill R, Storakers B, Zdunek A. A theoretical study of the Brinell hardness test. Proceedings of the Royal Society of London A: Mathematical, Physical and Engineering Sciences: The Royal Society; 1989. p. 301-30.
[207] Biwa S, Storåkers B. An analysis of fully plastic Brinell indentation. Journal of the Mechanics and Physics of Solids. 1995;43:1303-33.
[208] Mesarovic SD, Fleck NA. Spherical indentation of elastic–plastic solids. Proceedings of the Royal Society of London A: Mathematical, Physical and Engineering Sciences: The Royal Society; 1999. p. 2707-28.
[209] Lee HY. Ball indenter utilizing fea solutions for property evaluation. U.S. Patent No. 6,778,916.; 2004.
[210] Alcalá J, Barone AC, Anglada M. The influence of plastic hardening on surface deformation modes around Vickers and spherical indents. Acta Materialia. 2000;48:3451-64.
[211] Taljat B, Pharr GM. Development of pile-up during spherical indentation of elastic–plastic solids. International Journal of Solids and Structures. 2004;41:3891-904.

[212] Das G, Ghosh S, Ghosh S, Ghosh RN. Materials characterization and classification on the basis of materials pile-up surrounding the indentation. Materials Science and Engineering: A. 2005;408:158-64.
[213] Cheng Y-T, Cheng C-M. Relationships between hardness, elastic modulus, and the work of indentation. Applied physics letters. 1998;73:614-6.
[214] Korsunsky AM, McGurk MR, Bull SJ, Page TF. On the hardness of coated systems. Surface and Coatings Technology. 1998;99:171-83.
[215] Giannakopoulos A, Suresh S. Determination of elastoplastic properties by instrumented sharp indentation. Scripta materialia. 1999;40:1191-8.
[216] Korsunsky AM, Constantinescu A. Work of indentation approach to the analysis of hardness and modulus of thin coatings. Materials Science and Engineering: A. 2006;423:28-35.
[217] ASTM. E2546-15 Standard Practice for Instrumented Indentation Testing. ASTM International, West Conshohocken, PA. 2015.
[218] Van Vliet KJ, Prchlik L, Smith JF. Direct measurement of indentation frame compliance. Journal of materials research. 2004;19:325-31.
[219] Kang S-K, Kim J-Y, Kang I, Kwon D. Effective indenter radius and frame compliance in instrumented indentation testing using a spherical indenter. Journal of Materials Research. 2011;24:2965-73.
[220] Ahn J-H, Kwon D. Derivation of plastic stress–strain relationship from ball indentations: examination of strain definition and pileup effect. Journal of Materials Research. 2001;16:3170-8.
[221] Lee H, Haeng Lee J, Pharr GM. A numerical approach to spherical indentation techniques for material property evaluation. Journal of the Mechanics and Physics of Solids. 2005;53:2037-69.
[222] Kim J-Y, Lee K-W, Lee J-S, Kwon D. Determination of tensile properties by instrumented indentation technique: Representative stress and strain approach. Surface and Coatings Technology. 2006;201:4278-83.
[223] Lee JH, Kim T, Lee H. A study on robust indentation techniques to evaluate elastic–plastic properties of metals. International Journal of Solids and Structures. 2010;47:647-64.
[224] Lawn BR, Evans A, Marshall D. Elastic/plastic indentation damage in ceramics: the median/radial crack system. Journal of the American Ceramic Society. 1980;63:574-81.
[225] Nose T, Fujii T. Evaluation of Fracture Toughness for Ceramic Materials by a Single-Edge-Precracked-Beam Method. Journal of the American Ceramic Society. 1988;71:328-33.
[226] Sakai M, Bradt RC. Fracture toughness testing of brittle materials. International Materials Reviews. 1993;38:53-78.
[227] Morrell R. Fracture toughness testing for advanced technical ceramics: internationally agreed good practice. Advances in applied ceramics. 2006;105:88-98.
[228] Quinn GD, Bradt RC. On the Vickers Indentation Fracture Toughness Test. Journal of the American Ceramic Society. 2007;90:673-80.
[229] Maire E, Zhou S, Adrien J, Dimichiel M. Damage quantification in aluminium alloys using in situ tensile tests in X-ray tomography. Engineering Fracture Mechanics. 2011;78:2679-90.
[230] Ladeveze P. On an anisotropic damage theory. Proc CNRS Int Coll. 1983;351:355-63.
[231] Ladeveze P, Lemaitre J. Damage effective stress in quasi unilateral conditions. Proceedings of the 16th International Congress of Theoretical and Applied Mechanics, Lyngby, Denmark, August1984. p. 19-25.
[232] Lematrie. A course for Damage Mechanicas. 1996.
[233] Irwin GR. Fracture dynamics. Fracturing of metals. 1948;147:166.
[234] Irwin G. Analysis of Stresses and Strains Near the End of a Crack Traversing a Plate. J Appl Mech. 1957;24:361-4.
[235] Glinka G. Energy density approach to calculation of inelastic strain-stress near notches and cracks. Engineering Fracture Mechanics. 1985;22:485-508.